Oscillations of the Granular Retrosplenial Cortex

by

Sharena P. Rice

A dissertation submitted in partial fulfillment
of the requirements for the degree of
Doctor of Philosophy
(Neuroscience)
in the University of Michigan
2021

Doctoral Committee:

       Assistant Professor Omar J. Ahmed, Chair
       Professor W. Michael King
       Associate Professor Kayvan Najarian
       Assistant Professor Michael Roberts
       Professor Susan Shore

Sharena P. Rice

ricesp@umich.edu

ORCID iD: 0000-0002-4173-1710

DEDICATION

This dissertation is dedicated to all beings.

TABLE OF CONTENTS

LIST OF FIGURES

ABSTRACT

The retrosplenial cortex is essential for spatial memory and navigation. We aimed to learn about how the retrosplenial cortex encodes information through oscillations. Our results reveal an oscillation pattern we call "splines", resembling the similarly-named interlocking teeth on mechanical gears. Splines are 110-160 Hz, precisely coupled to the peaks of local theta rhythms, and observed during both REM sleep and active awake behaviors. We found that splines are distinct from gamma rhythms: while gamma rhythms are in-phase across the two retrosplenial hemispheres, splines are anti-phase across the hemispheres. By sorting theta cycles by either spline or gamma power, we show that retrosplenial splines and gamma oscillations occur independently of each other within any given theta cycle. Splines are also distinct from sharp wave ripples and alternate with sharp wave ripples across REM and NREM sleep, respectively. At higher running speeds, splines become more powerful, more strongly phase-amplitude coupled to theta, and have greater cross-hemispheric coherence. The retrosplenial cortex's ability to rapidly switch between splines and gamma as distinct modes of rapid interhemispheric communication may allow this region to more effectively integrate information using two mechanistically distinct rhythms.

CHAPTER 1: Introduction

1.1 Abstract

Where are we? How do we know it? Where are we going?

To answer any of these questions, the brain must construct internal maps of the outer world. Here, we review cell types and brain regions involved in creating these internal representations. We then explore the circuitry of the retrosplenial cortex, a region essential for successful spatial navigation. The retrosplenial cortex has reciprocal connections to many different brain regions involved in sensory processing and memory. This interconnectedness allows the retrosplenial cortex to integrate the allocentric and egocentric perspectives of space. Lastly, we highlight oscillations involved in transmitting navigationally-relevant information and discuss how these oscillations may be generated.

1.2 Navigation in the mammalian brain

Diversity across mammals results in an array of navigational strategies employed by each species, but all require the capacity to orient in space. Charles Darwin suggested that animals orient themselves by tracking their current position relative to a

starting point through combining internal and external motion cues to continuously estimate speed and direction (Darwin, 1873; Barlow, 1964). This "dead reckoning," as Darwin called it, is also known as path integration, as it requires the integration of various types of cues along the navigated path. Landmark-related navigation, in contrast, involves relating the body's location with respect to landmark cues rather than the motion cues used in path integration (Taube and Burton, 1995). Being able to perform both path integration and orient to landmarks may allow for more accurate navigation.

Navigation involves motion, which means that the navigating agent must keep track of motion signals and relate them to other streams of incoming information during navigation. Mammalian navigation is thought to involve sequence encoding that combines information from changing sensory scenes with internal memory processes (Pastalkova et al., 2008; Spiers et al., 2001). Different senses may be given different weights in processing spaces depending on the navigational strategy used: where visual information is limited, unreliable, unavailable, or unattended to, more processing power may be dedicated to other senses, such as balance and proprioception, for successful navigation (Townsend et al., 2019; Angelaki et al., 2009; Butler et al., 2010; de Winkel et al., 2017). This chapter will discuss the neural circuitry and brain rhythms involved in navigation, demonstrating why further studies of the retrosplenial cortex (RSC) will contribute to our knowledge of the science underpinning navigation.

1.2.1 Neural circuits of navigation

Many regions are involved in spatial navigation, including the hippocampus. Cells that encode specific locations were first identified in CA1 of the hippocampus in 1971 (O'Keefe and Dostrovsky, 1971). Further experiments of rats navigating in mazes demonstrated that a subset of hippocampal neurons fired in response to specific places (O'Keefe, 1976; O'Keefe and Conway, 1978). These cells that prefer to fire in particular places are called "place cells" (O'Keefe, 1979). Place cells are found in CA1 (O'Keefe and Conway, 1978; O'Keefe and Dostrovsky, 1971), CA3 (Hwaun and Colgin, 2019; Leutgeb et al., 2007), and dentate gyrus (Leutgeb et al., 2007) of the hippocampus.

The medial (Fyhn et al., 2004) and lateral entorhinal cortices are strongly interconnected with the hippocampus (Dolorfo and Amaral, 1998; Ahmed and Mehta, 2009; Amaral and Witter, 1989). The lateral entorhinal cortex has weak spatial specificity (Hargreaves et al., 2005) and likely carries episodic temporal information (Tsao et al., 2018). Border cells, which preferentially respond to borders in an environment, are found in the medial entorhinal cortex (MEC) (van Wijngaarden et al., 2020; Solstad et al., 2008), the parasubiculum (Solstad et al., 2008), the subiculum (Stewart et al. 2013), and the RSC (van Wijngaarden et al., 2020). Boundary vector cells are found in the subiculum (Stewart et al. 2013) and are tuned to reflect both proximity and orientation to the borders of an arena (Barry et al., 2006).

About 15% of the cells across all layers of the medial entorhinal cortex are speed cells, which positively respond to running speed with low levels of spatial and directional information (Kropff et al., 2015). The medial entorhinal cortex also contains cells with multipeaked spatial firing fields that respond during movement around an environment (Fyhn et al., 2004; Hafting et al., 2005). Further characterization revealed that these

neurons fired with a repeating tessellating hexagonal grid pattern during navigation, and that the grid structure of firing fields is expressed instantly in a novel room (Hafting et al., 2005). Since this pattern tiles spatial environments with a grid, the neurons with this property are called "grid cells."

Some computational models of grid cells require head direction signals to accurately reproduce the spatial grid (Giocomo et al., 2011; O'Keefe and Burgess, 2005; McNaughton et al., 2006; Fuhs and Touretzkey, 2006). Head-direction cells signal an animal's head direction in its environment (Taube et al., 1990a, 1990b). Head-direction cells are found in many brain regions. The anterodorsal thalamic nucleus (ADN) is the region containing the highest proportion of head-direction cells, where 50-60% of its neurons encode head direction (Taube, 1995). The ADN projects to layers 1 and 3 (Brennan et al., 2021) of RSC (van Groen and Wyss, 1990; van Groen and Wyss, 1995; van Groen and Wyss, 1990; Yamawaki et al., 2019a), where 10% of RSC neurons have been shown to encode head direction (Cho and Sharp, 2001). Upon electrolytically lesioning the RSC, the ADN's head-direction cells were less stable in their preferred firing orientations, even in the presence of visual landmark information (Clark et al., 2010). This suggests a critical role for the RSC in the head direction system, despite a relatively low proportion of RSC cells encoding head direction.

The head direction signal is produced first by angular head velocity information being sent from the vestibular afferents the vestibular nuclei (Highstein and Holstein, 2006), which send information through a long chain of different brain regions for processing (Cullen and Taube, 2017; Valerio and Taube, 2016; Schuerger and Balaban, 1993 (Figure 1-2)). This information eventually reaches the anterodorsal thalamic

nucleus and the RSC, which contain head direction cells. The head direction signal cannot rely solely on visual cues, but needs information from the vestibular system to adequately encode head direction. The vestibular inner ear has semicircular canals, which encode rotational motion of the head (Corradi et al., 2014). Valerio and Taube's single-unit recordings in the anterodorsal thalamus of transgenic *epistatic circler* mice without functional horizontal semicircular canals demonstrated that head direction cell activity is unstable in these mice (Valerio and Taube, 2016). Along with the semicircular canals, the vestibular inner ear has otoliths to sense translational head motion (Corradi et al., 2014). Otoliths contain crystals of calcium carbonate, called otoconia (Johnson et al., 1982), which are critical for detecting linear acceleration (Athanasiadou et al., 2020). Experiments with *tilted* mice, which have otoconia deficiencies, show that these mice have reduced spatial coherence with place fields forming closer to environmental boundaries (Harvey et al., 2018). The place cells of *tilted* mice do not lose their firing coherence in the absence of visual information.

How do directional signals become integrated with environmental landmarks? Two types of cells that seem suited to this task have been identified in retrosplenial cortex in-vivo. One of these cell types is egocentric boundary vector cells (EBCs), a type of boundary vector cell which encodes both distance from and orientation to borders in the environment (Alexander et al., 2020a). This vector-based location signal is more prominent in retrosplenial dysgranular cortex (RSD), where 38.7% of neurons recorded were classified as EBCs. Along with EBCs, axis cells integrate position with motion. Axis cells are found in the dorsal subiculum and map the current axis of the animal during navigation, regardless of the direction the animal moves along the cells'

preferred axis (Olson et al., 2017). Axis cells in the dorsal subiculum have firing peaks bimodally at head orientations 180 degrees apart.

Multiple cell types are involved in encoding navigationally-relevant spatial relationships (Figure 1-1). Some neurons are conjunctive, encoding more than one dimension. For example, a subpopulation of neurons in the entorhinal cortex encodes both head direction and the regularly-occurring intervals of grid fields (Kubie and Fenton, 2012; Gerlei et al., 2020) while some neurons in the medial entorhinal cortex encode both grid fields and angular velocity (Finkelstein et al., 2018). The existence of conjunctive cells is unsurprising, given that most cortical microcircuits receive at least two functionally distinct afferent inputs from different brain regions (Bittner et al., 2015).

In addition to real-world paradigms, virtual reality environments provide another means to studying spatial navigation in controlled settings. Aronov and Tank had rats perform random foraging and target pursuit tasks during two-dimensional spatial navigation in a virtual environment, in which the rats were not head-fixed (Aronov and Tank, 2014). They found that place cells, grid cells, head direction cells, and border cells are not limited to physical cues, but also able to follow virtual cues. Similarly, fMRI experiments with human subjects demonstrated that the thalamus codes facing direction and that the anatomically-defined RSC codes for head direction in virtual environments (Shine et al., 2016). In addition to the RSC, the vestibular stimulation is known to activate the hippocampal formation in humans (Vitte et al., 1996) and rats (Horii et al., 1994, 2004). While humans with acquired bilateral vestibular loss do not have general memory deficits, they develop significant atrophy of the hippocampus and

have significant deficits in navigating a virtual Morris water maze (Brandt et al., 2005; Kremmyda et al., 2016).

1.2.2 Retrosplenial cortex cell types

Like other regions of the cortex, the retrosplenial cortex has fast-spiking (FS) PV+ neurons (Brennan et al., 2020; Yousuf et al., 2020; Sempere-Ferrández et al., 2018). FS neurons fire rapidly without attenuation in response to stimuli (Connors and Gutnick, 1990). They evoke inhibitory currents with narrow potentials in their spikes and postsynaptic potentials and quick, sharp afterhyperpolarizations, (Connors and Gutnick, 1990; Sempere-Ferrández et al., 2018). Along with FS neurons, there are at least three distinctive firing types of excitatory neurons in the RSG: intrinsically-bursting (IB), regular-spiking (RS), and low-rheobase (LR) (Yousuf et al., 2020; Brennan et al., 2020).

IB neuron spiking happens in clusters called bursts (Connors and Gutnick, 1990). They are only found in layer 5 of RSG, comprising 5% of neurons in the layer (Sempere-Ferrández et al., 2018; Yousuf et al., 2020).

In the RSC, RS neurons comprise 40% of layers 2/3 neurons and 82% of layer 5 (Yousuf et al., 2020), making them the most commonly-observed firing type in the region. RS neurons are excitatory and adapt strongly to maintained stimuli (Connors and Gutnick, 1990; Brennan et al., 2020). They have relatively broad spike widths.

LR neurons are small hyperexcitable pyramidal cells. To our knowledge, low-rheobase neurons are not found anywhere besides the RSG. These cells fire persistently for the entire duration of a stimulus without spike frequency adaptation. LR

neurons comprise 60% of neurons in layers 2/3 of the RSG and are the dominant excitatory neurons of the superficial retrosplenial cortex (Brennan et al., 2020). These neurons are localized to layers 2 and 3, which are the superficial layers of the RSG, and they receive inputs from the anterior thalamic nuclei and the dorsal subiculum (Brennan et al., 2021). This anatomical and spatial layout makes most LR neurons likely to encode spatial information conjunctively, integrating head position and head velocity from the anterior thalamic nucleus inputs with the dorsal subiculum's information on the axis of travel. While these cells have previously been described as "late-spiking" neurons, their defining property is not spiking with greater latency, but a low-rheobase: a low input to evoke a spike (Brennan et al., 2020).
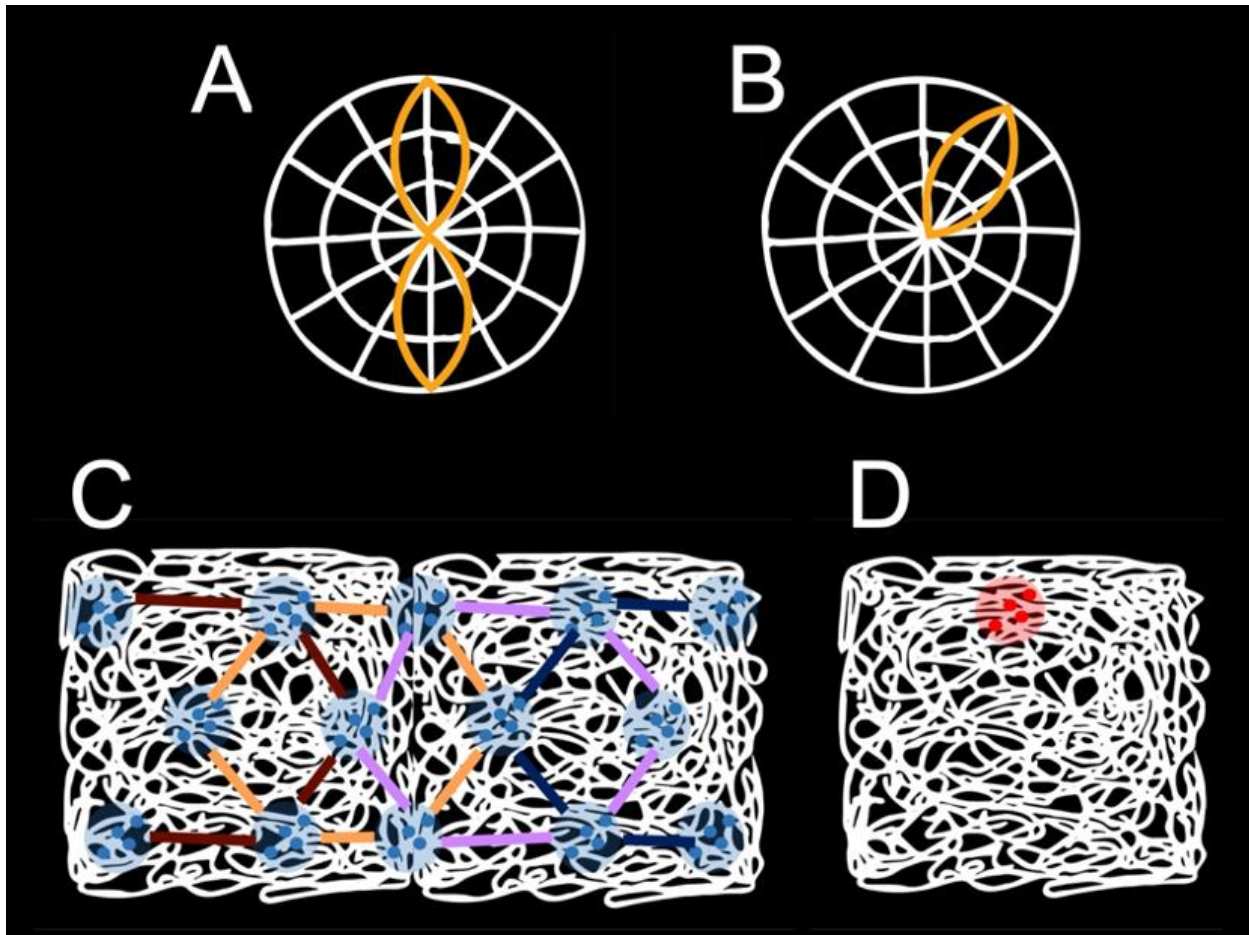
Figure 1-1. Examples of spatial encoding cell types.
A. Orange: illustration of directional tuning in axis cells, found in the subiculum (Olson et al., 2017). Axis cells' two orientation peaks are not necessarily equal in their tuning.
B. Head direction cells are tuned to head direction relative to the surroundings. They are found in the retrosplenial cortex, the anterior thalamic nuclei, postsubiculum, and medial prestriate cortex, among others (Taube, 1998).
C. Grid cells have a repeating tessellating hexagonal pattern. They are found in the medial entorhinal cortex (Hafting et al., 2005).
D. Place cells in the hippocampus preferentially fire in response to places (O'Keefe, 1976).
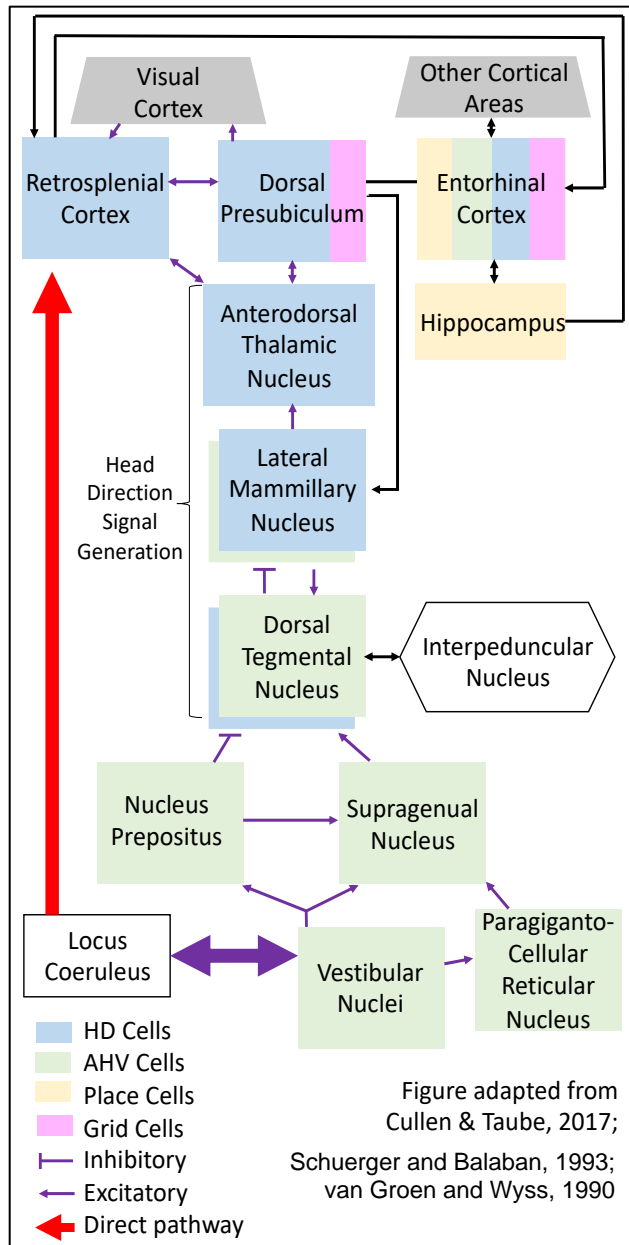
Figure 1-2. Head direction pathway. Vestibular information is transmitted from the vestibular afferents in the inner ear to the vestibular nuclei. The vestibular nuclei have connections with other regions and the information is processed by various regions as it is transmitted through the pathway. These different brain regions contain different cell types (Cullen and Taube, 2017; Schuerger and Balaban, 1993; van Groen and Wyss, 1990).

1.2.3 Retrosplenial cortex gross anatomy

      The retrosplenial cortex (RSC) is a midline structure essential for navigation and thought to serve as the bridge between egocentric and allocentric spatial processing (Vann et al., 2009; Maguire, 2001; Epstein, 2008; Burgess et al., 2001; Byrne et al., 2007; Alexander et al., 2020b). In humans, the RSC is located behind the splenium, hence the name "retrosplenial" (Vann et al., 2009). In the rodent brain, the RSC is one of the largest regions, spanning more than half of the length of the cerebrum (Paxinos et al., 2001; Paxinos and Watson, 2007). The RSC is interconnected with many regions involved in sensory integration, fear processing, and navigation, including the hippocampus (Yamawaki et al., 2019a, 2019b), dorsal subiculum, primary visual cortex (Vogt and Miller, 1983), anterior thalamic nucleus (van Groen and Wyss, 1990; Wyss et al., 1990; van Groen and Wyss, 1995; van Groen and Wyss 2003; Odagiri et al., 2011; Yamawaki et al., 2019b; Brennan et al., 2021), basal forebrain (Murakami et al., 2013; Robertson et al., 2009), dorsal subiculum (Yamawaki et al., 2019a; Kinnavane et al., 2018; Brennan et al., 2021), locus coeruleus (van Groen and Wyss, 1990), and entorhinal cortex (van Wijngaarden et al., 2020). The RSC also sends monosynaptic excitatory projections to the secondary motor cortex (Yamawaki, et al., 2016).

1.2.4 Granular and dysgranular retrosplenial cortex

      The retrosplenial cortex can be divided into the granular retrosplenial cortex (RSG), also known as area 29, and the dysgranular retrosplenial cortex (RSD), also

known as area 30 (Vann et al., 2009). The RSG and RSD are reciprocally connected (van Groen and Wyss, 1992, 2003) but distinct in their cytoarchitecture (van Groen and Wyss, 2003) and connectivity with other regions (van Groen and Wyss, 1992, 2003). Unlike the sparse cellular density in the superficial layers of RSD (van Groen and Wyss, 2003), 60% of the neurons in the densely-packed layers 2 and 3 of RSG (Sripanidkulchai and Wyss, 1987) are low-rheobase (LR) neurons (Brennan et al., 2020).

1.3 Oscillations in navigation and sleep

Synchronous synaptic transmission across populations of neurons generates oscillations (Buzsáki and Watson, 2012; Sohal, 2012). The precise timing of when different neurons fire in relation to population activity sheds light on how the oscillation is generated by populations of neurons (Sohal, 2012; Headley and Weinberger, 2013). Different kinds of oscillations can co-occur within the same region. Cross-frequency coupling between different types of oscillations can demonstrate the temporal organization of the larger network's activity (Buzsáki and Watson, 2012; Mathalon and Sohal, 2015). Brain and behavioral states have neural oscillatory correlates. Oscillations are also useful to study for better understandings of disease mechanisms, with potential for use in clinical applications as disease biomarkers (Neustadter et al., 2016; Winer et al., 2019; Fitzgerald and Watson, 2018).

1.3.1 Gamma rhythms

Gamma rhythms are 30-80 Hz oscillations that are important for information processing during navigation. They occur during a range of behavioral states: active focused attention (Murthy and Fetz, 1992; Jensen et al., 2007), learning and memory (Osipova et al., 2006; Headley and Weinberger, 2011, 2013; Jensen et al., 2007), sensory perception (Engel et al., 2001), decision-making during wakefulness (Amemiya and Redish, 2018), and spontaneously during REM sleep (Steriade, 2009). Defects in gamma rhythms have been linked to cognitive inflexibility in a $Dlx5/6^{+/-}$ mouse model, which has reduced numbers of PV+ interneurons (Cho et al., 2015), and entraining gamma rhythms via multisensory gamma stimulation has been found to improve cognition and reduce amyloid pathology present in the 5xFAD Alzheimer's mouse model (Martorell et al., 2019).

The pyramidal interneuron gamma (PING) model suggests that external input to excitatory and inhibitory neurons drives synchronous rhythmic spiking (Börgers and Kopell, 2003, 2005; Tiesinga and Sejnowski, 2009). Excitatory pyramidal neurons and inhibitory GABAergic interneurons are synaptically interconnected in a loop (Whittington et al., 2000; Börgers and Kopell, 2005, Lee and Jones, 2013, Tiesinga and Sejnowski, 2009). While the excitatory neurons fire just before the trough of gamma, the inhibitory neurons fire preferentially at the trough (Hasenstaub et al., 2005). The PING mechanism allows for the generation of multiple frequencies, where the oscillation's frequency largely depends on the strength and duration of the inhibitory synaptic currents and on the external drive (Börgers, 2017).

Hippocampal gamma comes from at least two sources: self-generated within the hippocampus (Bragin et al., 1995; Csicsvari et al., 2003; Colgin et al., 2009) and through the medial entorhinal cortex (Bragin et al., 1995; Colgin et al., 2009). Fast gamma oscillations in CA1 are synchronized with fast gamma in the medial entorhinal cortex, while slow gamma in CA1 is coherent with slow gamma in CA3. Hippocampal gamma increases in frequency with faster running speed (Ahmed and Mehta, 2012). Gamma power increases in hippocampal areas during stimulus encoding improves spike timing accuracy and predicts memory recall (Jutras et al., 2009). Gamma oscillations can dynamically coordinate hippocampal networks according to behavioral demands (Montgomery and Buzsáki, 2007).

Gamma has also been found in other regions, including the sensorimotor cortices (Murthy and Fetz, 1992, 1996), the visual cortex (Zhigalov et al., 2021), anterior cingulate cortex (Koike et al., 2017), and the RSC (Alexander et al., 2018; Koike et al., 2017). Since cortical neurons can synchronize across distances to process stimulus features (Gray et al., 1989), they are thought to be involved in attention and binding features of the sensory scene. Two frequency bands have been described in the retrosplenial cortex: gamma at 40-100 Hz and fast gamma at 100-160 Hz (Alexander et al., 2018; Koike et al. 2017). Fast gamma has been observed in paradoxical sleep (Koike et al., 2017) and during awake running behaviors (Alexander et al., 2018), and high-frequency oscillations have been described in the parietal and prefrontal cortices (Sirota et al., 2008), parietal neocortex (Scheffzük et al., 2011), and primary somatosensory cortex (González et al., 2020). Further research is needed to determine the precise mechanisms of these fast cortical rhythms.

1.3.2 Theta rhythms

Theta rhythms are 4-12 Hz oscillations in rodents. Projections from the basal forebrain's medial septum and diagonal band of Broca activate inhibitory interneurons and control hippocampal rhythmogenesis (Dannenberg et al., 2015). Lesioning or inactivating the MS disrupts theta rhythms in structures that receive MS projections, including the medial entorhinal cortex (Mitchell et al., 1982; Koenig et al., 2011; Brandon et al., 2011) and the hippocampus (Mizumori et al., 1990; Koenig et al., 2011). Hippocampal theta rhythms are prominent during both running and REM sleep, and they are thought to support both navigation and memory (Buzsáki, 2011; Buzsáki and Moser, 2013). Theta rhythms are important for sequence information processing at different timescales, such as during running behavior at variable speeds (Buzsáki and Moser, 2013; Dragoi and Buzsáki, 2006; Maurer et al., 2012; Wang et al., 2015). Neurons in the some cortical regions fire in sync with theta rhythms during REM sleep and awake running (Sirota et al., 2008).

Theta rhythms are also present in the RSC (Alexander et al., 2018, Alexander et al., 2020a), a target of basal forebrain cholinergic projections (Robertson et al., 2009; Bigl et al., 1982). As a subpopulation of egocentric boundary cells are synchronized with hippocampal theta oscillations (Alexander et al., 2020a), this suggests the subpopulation of egocentric boundary vector cells that does not synchronize with hippocampal theta may respond to and integrate other types of inputs. RSC's theta rhythmicity in relation to neuronal firing needs further exploration as a potential

mechanism for mediating functions that seem unique to the RSC, such as integrating landmark cues from the environment with self-motion cues.

1.3.3 Sharp wave ripples

Generating gamma and theta rhythms supports sensory and sequence information encoding, and memories of this information are mediated by sharp wave ripples (SWRs; Buzsáki, 1989, 2015). SWRs are brief high frequency oscillations of 100-250 Hz that occur during both non-rapid eye movement (NREM) sleep and awake immobility (Buzsáki, 2011). SWRs represent a highly-synchronous population pattern in the mammalian brain (Buzsáki, 2015), allowing for replay of fragments of waking neuronal sequences in a compressed format (Skaggs and McNaughton, 1996; Louie and Wilson, 2001). This compressed hippocampal representation is then transferred to other portions of the sensory and memory circuit, including and several subcortical nuclei (Todorova and Zugaro, 2020) and RSC (Nitzan et al., 2020). Sharp wave ripples are generated by the fast inhibitory neuronal oscillation (FINO) mechanism (Schlingloff et al., 2014).

1.4 Retrosplenial cortex dysfunctions

Retrosplenial cortex hemorrhage creates challenges in recalling recent events. A person with retrosplenial hemorrhage could not remember the birth of his four-year-old child, believing that he only had one child (Valenstein et al., 1987). The patient's

anterograde amnesia was so profound that he could not remember what he had done that morning.

There are multiple hints that RSC dysfunctions underlie Alzheimer's disease symptoms. 93% of people with Alzheimer's experience spatial disorientation (Monacelli, 2003), and these are similar disorientations to patients with damage to their retrosplenial cortex via hemorrhage (Osawa et al., 2008) and stroke (Ferguson et al., 2019). Early-onset metabolic dysfunction of retrosplenial cortex precedes overt amyloid plaque formation (Poirier et al., 2011).

Studying retrosplenial cortex microcircuitry may allow for earlier detection of Alzheimer's disease. This may be done through biomarkers, such as measuring retrosplenial cortex oscillations as a diagnostic tool. Learning about the mechanisms of brain rhythms has the potential to pave the path to high-precision Alzheimer's treatments that may circumvent the unpalatable side effects of current drugs. People with Alzheimer's disease have altered communication across the hemispheres (Lakmache et al., 1998) and their retrosplenial cortices have metabolic dysfunction (Nestor et al., 2003). Thus, it is also possible that retrosplenial oscillation disruptions serve as neurophysiological biomarker of Alzheimer's. Perhaps restoring retrosplenial oscillations could prevent disorientation, improving the quality of life for people with Alzheimer's disease.

1.5 Questions addressed in this dissertation

Researching how retrosplenial cortex oscillations function in sleep and in movement allows us to advance our understanding of mechanisms for spatial memory encoding and consolidation. This dissertation explores the oscillations across layers of the retrosplenial cortex during different brain states. In the second chapter, we characterize oscillations during sleep. We have found that during REM sleep, 110-160 Hz oscillations coupled to the peaks of theta rhythms are strongest in the superficial layers of the RSG, and that these fast oscillations are anti-phase across the RSG's hemispheres. Since these antiphase oscillations resemble the interlocking teeth of mechanical gears, we call them "splines". We find that splines and gamma occur at different phases of theta rhythms. Gamma rhythms are in-phase across the hemispheres.

In the third chapter, we characterize splines at different running speeds. Splines become more coherent and more precisely anti-phase across the hemispheres at faster running speeds. The retrosplenial cortex's ability to switch between gamma and splines for rapid cross-hemispheric communication may be a mechanism of information transfer which allows the brain to encode information more efficiently. In the future, splines may also be explored as a physiological biomarker for brain health and perhaps serve as a target to restore memory functions in disorders such as Alzheimer's disease.

CHAPTER 2: Oscillations of the Retrosplenial Cortex During Sleep

2.1 Abstract

The retrosplenial cortex is essential for successful spatial navigation and memory, including sleep-dependent memory consolidation. To better understand the spectral signatures associated with sleep, here we monitored retrosplenial oscillatory dynamics during different stages of sleep. In rats, we implanted tetrodes into the retrosplenial cortex, as well as CA1, the posterior parietal cortex, and the visual cortex. In mice, we implanted silicon probes across both hemispheres of the retrosplenial cortex and into CA1 of the hippocampus. A unique high-frequency (110-160 Hz) oscillation is precisely coupled to the peak of theta rhythms in the retrosplenial cortex during REM sleep. Our experiments in mice revealed that these high-frequency oscillations are surprisingly anti-phase across the retrosplenial cortex's hemispheres and have the highest power in the superficial layers (layers 2 and 3) of the retrosplenial cortex. This high-frequency oscillation is a mode of cross-hemispheric coordination distinct from gamma rhythms, which is in-phase across the hemispheres. The ability of

the retrosplenial cortex to switch between these two modes of rapid interhemispheric coordination may play a role in information processing and memory consolidation.

2.2 Introduction

Sleep is important for survival (Meddis, 1975; Everson, 1995) and memory consolidation in mammals (Rasch and Born, 2013). The stages of sleep are correlated with different brain rhythms. During slow wave sleep, the hippocampus generates large irregular activity (LIA) and sharp wave ripples (SWRs) (Jarosiewicz et al., 2002). SWRs are essential for hippocampal-dependent memory trace formation (Buzsáki, 1989), as with procedural and declarative memories (Plihal and Born, 1997). Optogenetically prolonging sharp wave ripples initiated by the brain improves spatial memory (Fernández-Ruiz et al., 2019). While non-rapid eye movement (NREM) sleep contains sharp wave ripples, rapid eye movement (REM) sleep does not (Opalka et al., 2020).

During REM sleep, the eyes move rapidly and muscles are atonic (Rasch and Born, 2013). REM sleep is thought to play a role in consolidation of episodic memory (Rauchs et al. 2004). In mice and rats, REM sleep is accompanied by pronounced theta rhythms – 6-12 Hz oscillations seen in the local field potential (LFP) and EEG signals (Colgin, 2013). Traditionally, REM sleep has been associated with dreaming (Aserinsky and Kleitman, 1953), but dreaming can also occur in NREM (Siclari et al., 2017, 2018). The relations between NREM and REM sleep and why both of these sleep states are needed is still to be elucidated (Le Bon, 2020). As chronic sleep deprivation has been linked to increased amyloid beta and tau levels (Wang et al., 2020), and people with

Alzheimer's disease frequently report disordered sleep (Hennawy et al., 2019; Most et al., 2012; Blytt et al., 2017; Moran et al., 2005), learning more about how sleep affects the memory circuit may be useful for creating effective interventions.

The retrosplenial cortex (RSC) is a densely interconnected structure that is also critical for spatial navigation, with dysfunctions leading to impaired memory (Valenstein et al., 1987) and severe spatial disorientation in both humans and rodents (Osawa et al., 2008; Ferguson et al., 2019). Despite its critical importance, how the RSC coherently communicates with other brain regions to carry out its navigational functions remains poorly understood. Recent work has identified 110-160 Hz oscillations in the RSC during both awake running behaviors (Alexander et al., 2018) and REM sleep (Koike et al., 2017). Similar observations of ~110-160 Hz oscillations, though relatively rare, have been made in other brain regions (Scheffzük et al., 2011; Sirota et al., 2008). These rhythms have so far been referred to as either "high frequency oscillations" (Tort et al., 2013) or "fast gamma" (Scheffzük et al., 2011; Alexander et al., 2018; Koike et al., 2017), reflecting their ambiguous nature and emphasizing the need to identify the regions with which these unique oscillations coherently communicate.

2.3 Results

2.3.1 Retrosplenial REM splines alternate with hippocampal non-REM ripples across sleep states

To compare fast oscillatory activity across hippocampal CA1, retrosplenial cortex (RSC), and related cortical regions (visual cortex [V1] and posterior parietal cortex [PPC]), we first used custom microdrives and silicon probes to record multi-site sleep-wake signals (Figure 2-1). Figure 2-2 shows an example of simultaneously recorded spectrograms across CA1, RSC, PPC, and V1, together with the sleep-wake hypnogram (Figure 2-2A-E). While typical non-REM (NREM) ripples were found in hippocampal CA1, the most prominent fast oscillation observed in the cortex during sleep was a 110-160 Hz oscillation in the RSC during REM sleep (Figure 2-2C). Splines during REM sleep were localized in the RSC, and were rarely observed in either CA1, V1, or PPC (Figure 2-2A,D,E). Retrosplenial REM splines consistently alternated with hippocampal NREM ripples across sleep states (Figure 2-2F-H).

Population-averaged power spectra revealed clearly elevated spline (110-160 Hz) power during REM sleep, selectively in the RSC (Figure 2-2I-L; RSC: 9 rats, 62 sessions, 257 channels; CA1: 6 rats, 58 sessions, 203 channels; PPC: 2 rats, 13 sessions, 16 channels; V1: 3 rats, 40 sessions, 93 channels). To compare and quantify oscillatory power across brain regions, we computed the normalized spline power during REM sleep and found that this power was significantly higher in RSC than in any other brain region (N same as above; rank sum test, $p < 0.0001$ in all cases; Figure 2-2M). On the other hand, normalized ripple power during NREM sleep was significantly higher in CA1 (N same as above; rank sum test, $p < 0.05$ in all cases; Figure 2-2N). Qualitatively similar results were obtained whether the data was normalized by broadband power (1-230 Hz; Figure 2-2M-N) or by theta power (5-11 Hz; data not shown). Thus, hippocampal ripples are the dominant fast oscillation during NREM

sleep, but retrosplenial splines are the dominant fast network rhythm across the

sampled brain regions during REM sleep.
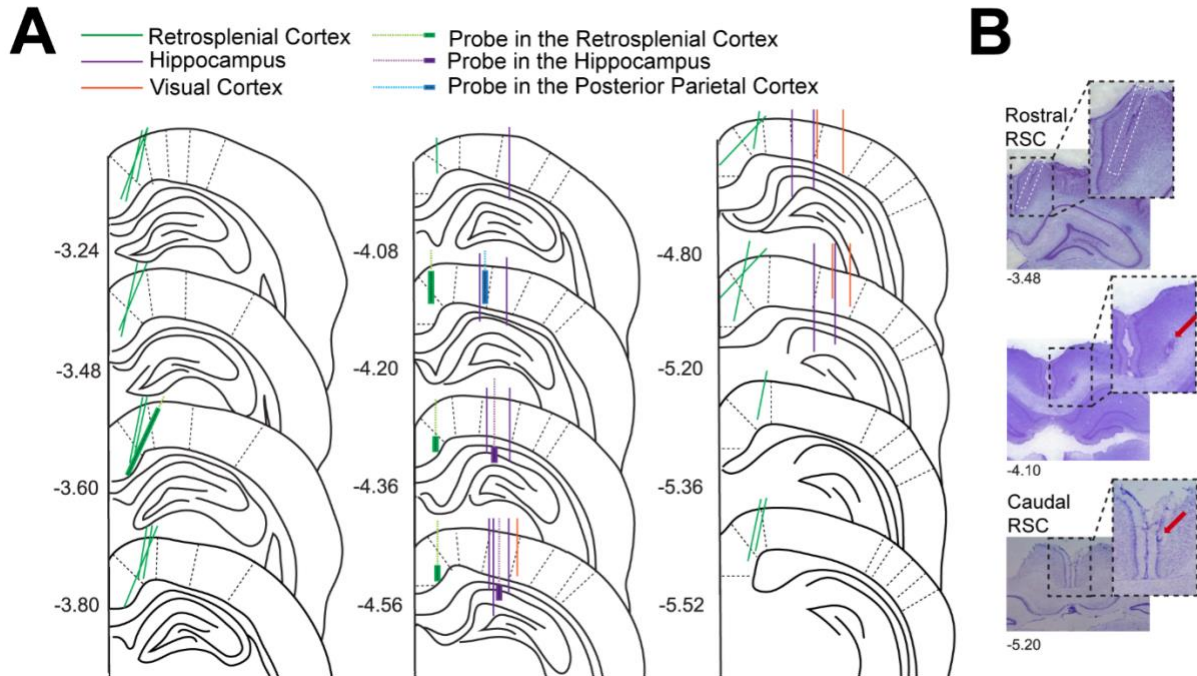
Figure 2-1. Anatomical location of tetrodes and silicon probes for electrophysiological recordings in retrosplenial cortex (RSC), hippocampus (HC), posterior parietal cortex (PPC), and visual cortex (V1).
A. Atlas schematic with precise AP distribution of electrodes.
B. Coronal sections of rat brains showing examples of tetrode track and electrolytic lesions used to identify the location of the recorded signals in RSC.

A

B Hippocampus

C Retrosplenial Cortex

D Posterior Parietal Cortex

E Visual Cortex

F

G Hippocampus

H Retrosplenial Cortex

I REM

J NREM

K

L

M REM
non whitened   whitened

N NREM
non whitened   whitened

CA1   RSC   PPC   V1

25
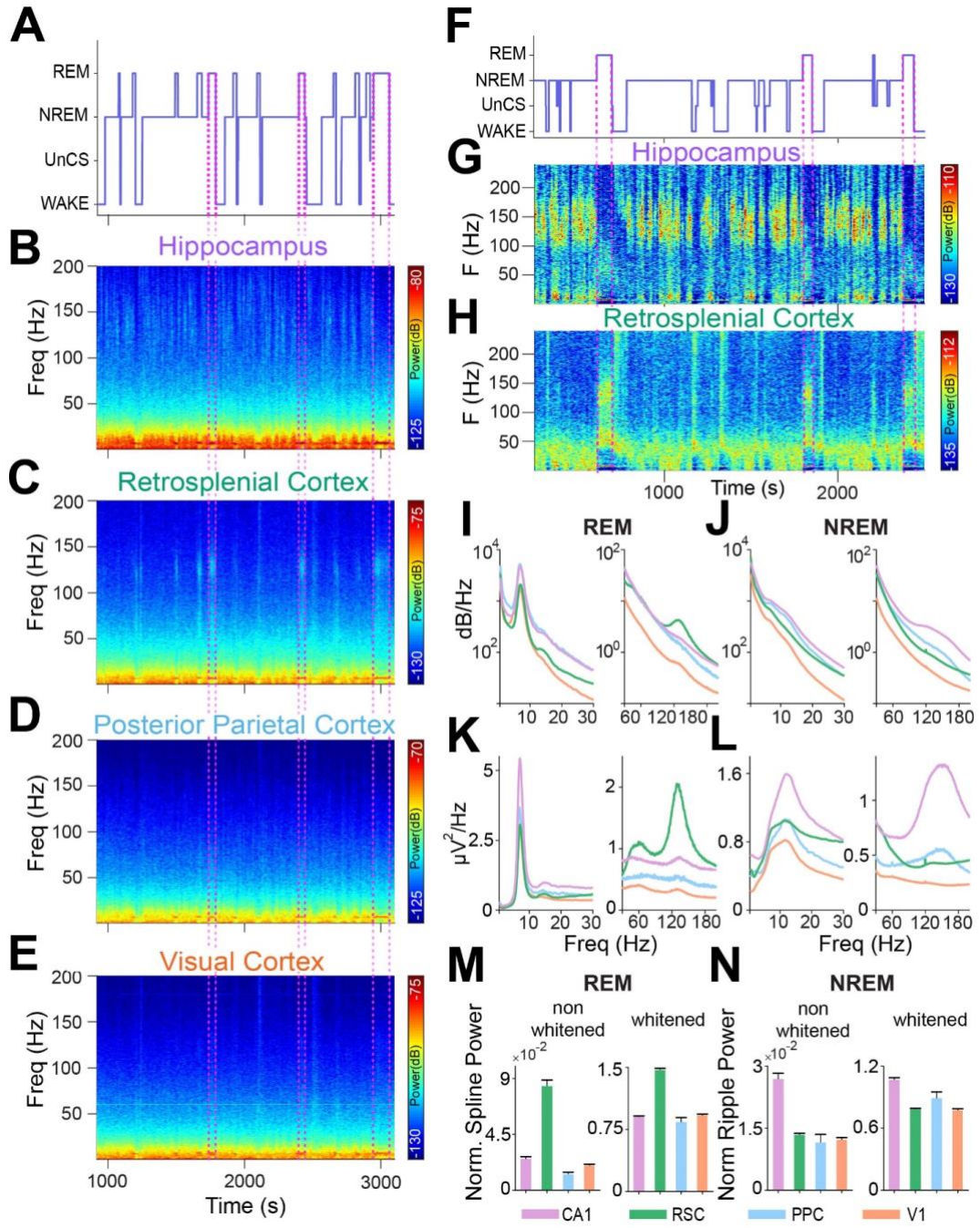
Figure 2-2. Splines are 110-160 Hz fast oscillations, strongest in the retrosplenial cortex during REM sleep.

A. Hypnogram from a sleep session with multiple NREM-REM transitions.

B-E. Corresponding spectrograms from hippocampal CA1, retrosplenial cortex (RSC), posterior parietal cortex (PPC), and primary visual cortex (V1), respectively. While CA1 shows typical NREM ripples (*B*), another high frequency oscillation in the 110-160 Hz range, which we refer to as splines, is seen in the RSC (*C*) during REM sleep (REM is demarcated by dotted lines). Hippocampal NREM ripples thus appear to alternate with RSC REM splines. Weak ripple and spline power were observed in PPC and V1 during NREM and REM, respectively (*D, E*).

F. Hypnogram from a sleep session in a separate rat.

G-H. Corresponding whitened spectrograms from CA1 and RSC respectively showing ripples during NREM sleep in CA1 alternating with splines in RSC during REM sleep (dotted lines again highlight example REM epochs).

I. Averaged spectra during REM sleep across CA1 (purple), RSC (green), PPC (blue), and V1 (orange). The low (0-30Hz) and high (30-200Hz) frequency bands have been separated for greater clarity. All 4 regions show high theta power during REM sleep. However only RSC shows significantly more spline power. Data shown in I – N is across 9 rats, 62 sessions, 257 channels from RSC; 6 rats, 58 sessions, 203 channels from CA1; 2 rats, 13 sessions, 16 channels from PPC; and 3 rats, 40 sessions, 93 channels from V1.

J. Averaged spectra during NREM across CA1 (purple), RSC (green), PPC (blue), and V1 (orange). CA1 shows high power in the ripple band (110-190 Hz) during NREM sleep. Note the very weak cortical ripples in PPC and RSC.

K, L. Same as I, J, but now showing averaged whitened power spectra.

M. Normalized spline power with pre- and post-whitened values. This ratio is significantly higher during REM sleep in RSC as compared to CA1, PPC, and V1 (rank sum test, $p<0.0001$ in all cases).

N. Normalized ripple power with pre- and post-whitened values. This ratio is significantly higher in CA1 during NREM compared to all other regions (rank sum test, $p <0.05$ in all cases)
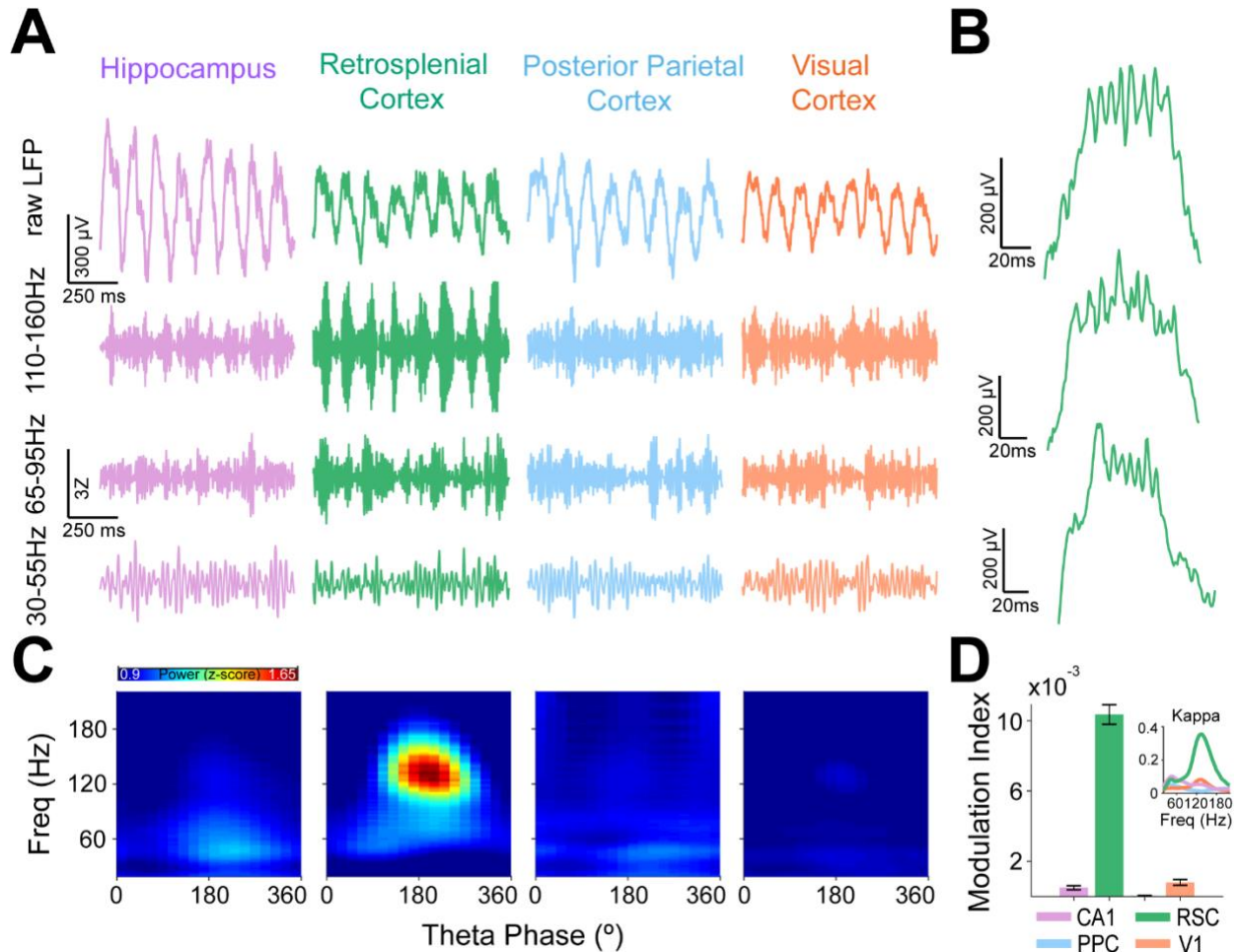
Figure 2-3. Retrosplenial splines are precisely coupled to the peak of theta.
A. Examples of simultaneously recorded raw and filtered LFP traces during REM sleep from CA1 (purple), RSC (green), PPC (blue), and V1 (orange) showing theta oscillations in all four brain regions but strong spline oscillations (110-160 Hz) at the peak of theta exclusively in RSC. Power in high (65-95 Hz) and low gamma (30-55 Hz) is much weaker than spline power in RSC and often phase-shifted compared to splines.
B. Single retrosplenial theta cycle examples during REM sleep from three separate rats. Splines are consistently locked to the peak of retrosplenial theta in all animals.
C. Population theta phase-amplitude coupling across the four brain regions during REM sleep. A phase of 180 degrees represents the peak of theta. Splines are precisely coupled to the peak of RSC theta. (9 rats, 62 sessions, 257 channels from RSC; 6 rats, 58 sessions, 203 channels from CA1; 2 rats, 13 sessions, 16 channels from PPC; and 3 rats, 40 sessions, 93 channels from V1.)
D. Strength of theta phase-amplitude coupling quantified for each LFP using the modulation index (MI) metric. Splines are more precisely coupled to theta in the RSC than in any other brain region (rank sum test, p<0.001). Inset shows kappa (measure of strength of phase-locking for circular variables) values for theta phase-amplitude coupling of each frequency. Kappa for splines was significantly higher (rank sum test, p< 0.0001) in RSC compared to CA1, PPC, and V1.
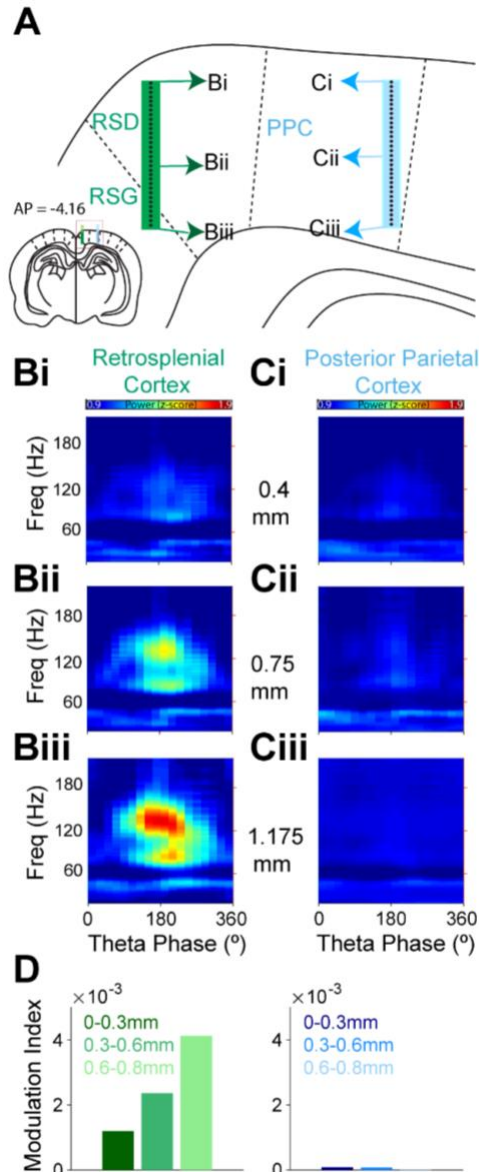
Figure 2-4. Coupling of splines to theta is strongest in the granular retrosplenial cortex.
A. Schematic of simultaneous recording in RSC and PPC in 1 rat using silicon probes (32 contacts on each probe).
B, C. Phase-amplitude coupling computed across 3 distinct depths on each probe, at the positions shown in **A**. The color axis is the same across all 6 plots. The strength of splines and their coupling to theta increases with depth in RSC, increasing sharply in the granular RSC compared to the dysgranular RSC. Phase-amplitude coupling of splines to theta is far weaker in superficial PPC and further decreases with depth.
D. All 32 contacts on each probe were grouped into 3 sub-groups based on their depth from the most superficial contact. The modulation index increases significantly with depth (rank sum, 0 – 0.3mm vs 0.3 – 0.6 mm, p = 0.007, 0.3 – 0.6mm vs 0.6 – 0.8 mm, p = 0.0015, 0 – 0.3mm vs 0.6 – 0.8mm, p <0.001). MI across PPC was significantly lower than that in RSC (rank sum, p<0.001 in all cases).

2.3.2 Splines are precisely and surprisingly coupled to the peak of theta, most strongly in the granular retrosplenial cortex

Since theta and spline power co-occurred in the RSC during REM sleep (Figure 2-2), we next explored the temporal relationship between spline and theta rhythms to confirm and extend previous observations (Alexander et al., 2018; Koike et al., 2017). Simultaneously recorded raw LFP traces from CA1, RSC, PPC, and V1 showed that splines selectively occur at the peak of RSC theta (Figure 2-3A-C). Given the lack of splines in other regions, this phase-amplitude coupling of splines to the theta peak was restricted to the RSC. Figure 2-3B shows three representative theta cycles from three different rats with splines consistently at the peak of each theta cycle. To study the strength of this phase-amplitude coupling of splines to the peak of theta, we used wavelet-based spectrograms and computed the strength of each fast frequency across the phases of theta cycles. Phase – amplitude plots across rats during REM (Figure 2-3C) confirmed that splines are strongest in RSC and precisely coupled to the peak of theta. To quantify the strength of coupling of splines to theta, we used the modulation index metric (Tort et al., 2010) and found it to be significantly higher in RSC compared to all other brain regions examined here (N same as for Figure 1; rank sum test, p <0.0001).

Since the RSC is subdivided into dorsal dysgranular and ventral granular subdivisions (van Groen and Wyss, 1992, 2003; Domesick, 1969), we asked whether the coupling of splines to theta differed between these regions. We found that across these two subdivisions of the RSC, the strength of theta phase-amplitude coupling of

splines increased with depth and was thus stronger in the granular RSC than in the

dysgranular RSC (Figure 2-4). Despite this strong modulation in spline amplitude by the

phase of the theta cycle in which splines occur, splines were not strongly modulated by

theta amplitude and occurred in both high and low amplitude theta cycles (Figure 2-5A).

Overall, theta amplitude and spline power were only weakly correlated (Figure 2-

5B, median ρ = 0.2 across 9 rats, 54 sessions and 216 channels). Thus, the occurrence

of prominent theta oscillations does not necessarily predict the occurrence of splines.

However, when splines do occur, they are precisely coupled to the peak of the

containing theta cycle.

Since splines were not strongly correlated to theta amplitude, we wondered if

there were other factors correlated to the probability of splines. Using an objective

algorithm to identify theta cycles with and without splines (Figure 2-6), we found that

spline-containing theta cycles tended to occur in clusters within each REM epoch

(Figure 2-7). To confirm the presence of such spline-rich REM frames, we computed the

probability of observing splines in a theta cycle, triggered off theta cycles with splines

versus theta cycles without splines. The triggering cycle in this analysis is referred to as

theta cycle 0. We found that when splines occurred in theta cycle 0, the probability of

observing splines in adjacent theta cycles was significantly elevated for up to -32 to +36

adjacent theta cycles (Figure 2-7B; two sample t-test, $p<0.05$). Thus, during REM sleep,

splines occurred in clusters spanning multiple contiguous theta cycles. To understand

the subtype-specific single unit correlates of spline-rich frames, we classified cells into

fast-spiking putative inhibitory neurons (FS) and regular-spiking putative excitatory

neurons (RS) using their characteristic waveform shapes. Figure 2-8 shows the clusters

and mean firing rate of each cell type during awake, NREM, and REM sleep states. The firing rate of both RSC and CA1 FS cells increased during spline-rich REM frames (Figure 2-8A-D). To quantify this observation, we computed the cycle-by-cycle firing rate of each cell during each REM theta cycle. We then compared this cycle-by-cycle firing rate triggered off theta cycles with splines versus theta cycles without splines (Figure 2-8E). The triggering cycle in this analysis is again referred to as theta cycle 0. We found that when splines occurred in theta cycle 0, the firing rate of both RSC and CA1 FS cells was elevated for at least ± 24 cycles (two sample t-test, $p < 0.05$). Thus, spline-rich REM frames are accompanied by increased FS cell activity.
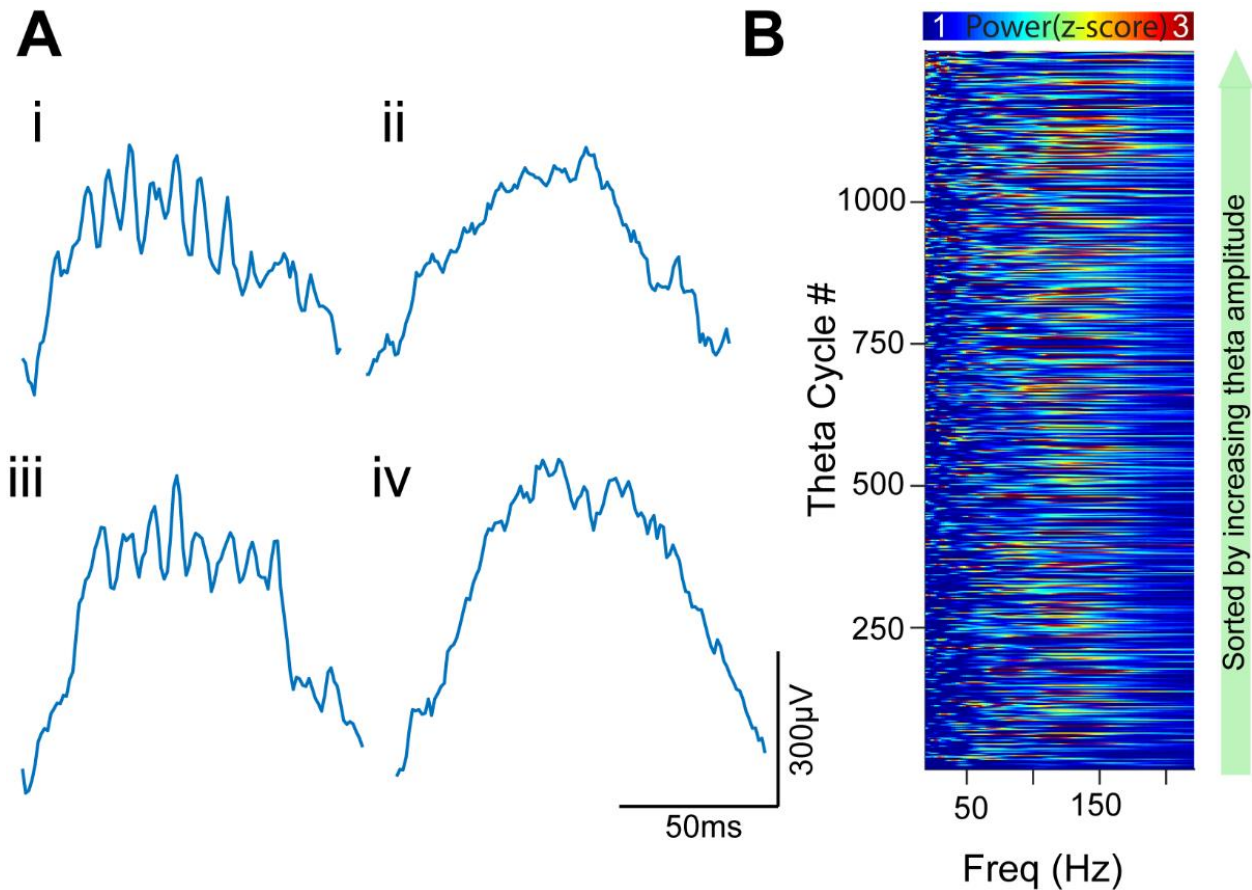
Figure 2-5. During REM sleep, spline power is independent of theta cycle amplitude.

Ai and Aii. Example of two lower amplitude theta cycles, one with (i) and the other without (ii) splines.

Aiii and Aiv: Example of two higher amplitude theta cycles, one with (iii) and the other without (iv) splines.

B. Theta cycles sorted by theta amplitude show that splines can occur during theta cycles of all amplitudes, and theta cycle amplitude is only weakly correlated to the corresponding cycle's spline power (median $\rho = 0.2$, across 9 rats, 54 sessions and 216 channels).
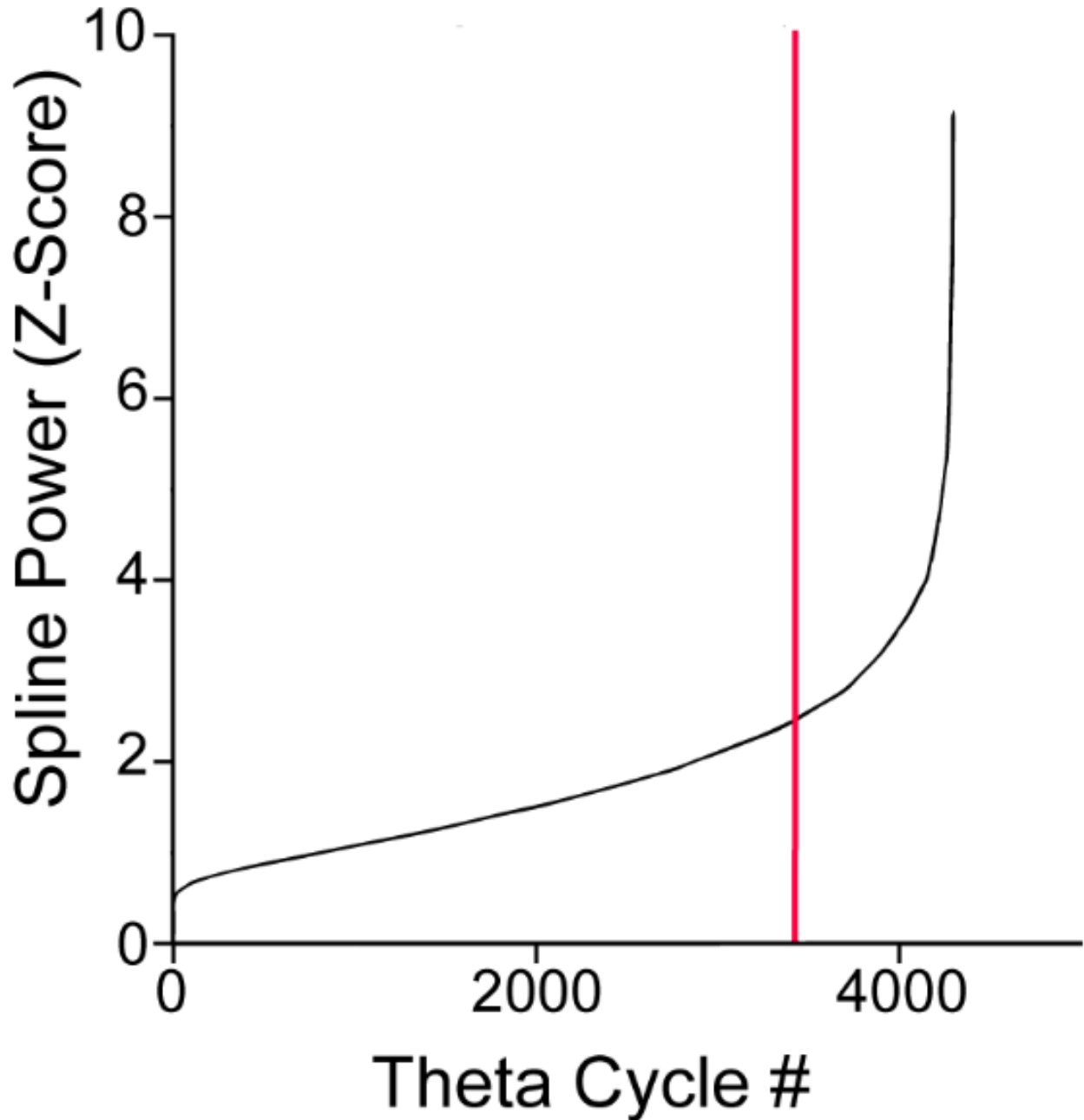
Figure 2-6. Objective algorithm to identify theta cycles with splines.
Theta cycles sorted by spline power in the retrosplenial cortex during REM. Red vertical line indicates the threshold for detecting splines identified using change point analysis (see Methods).

A

RSC FS RSC RS CA1 FS CA1 RS Theta cycles with splines

B

* splines observed in Theta Cycle 0
* no splines in Theta Cycle 0

C

Retrosplenial FS cells   Hippocampal FS cells

D

E

34
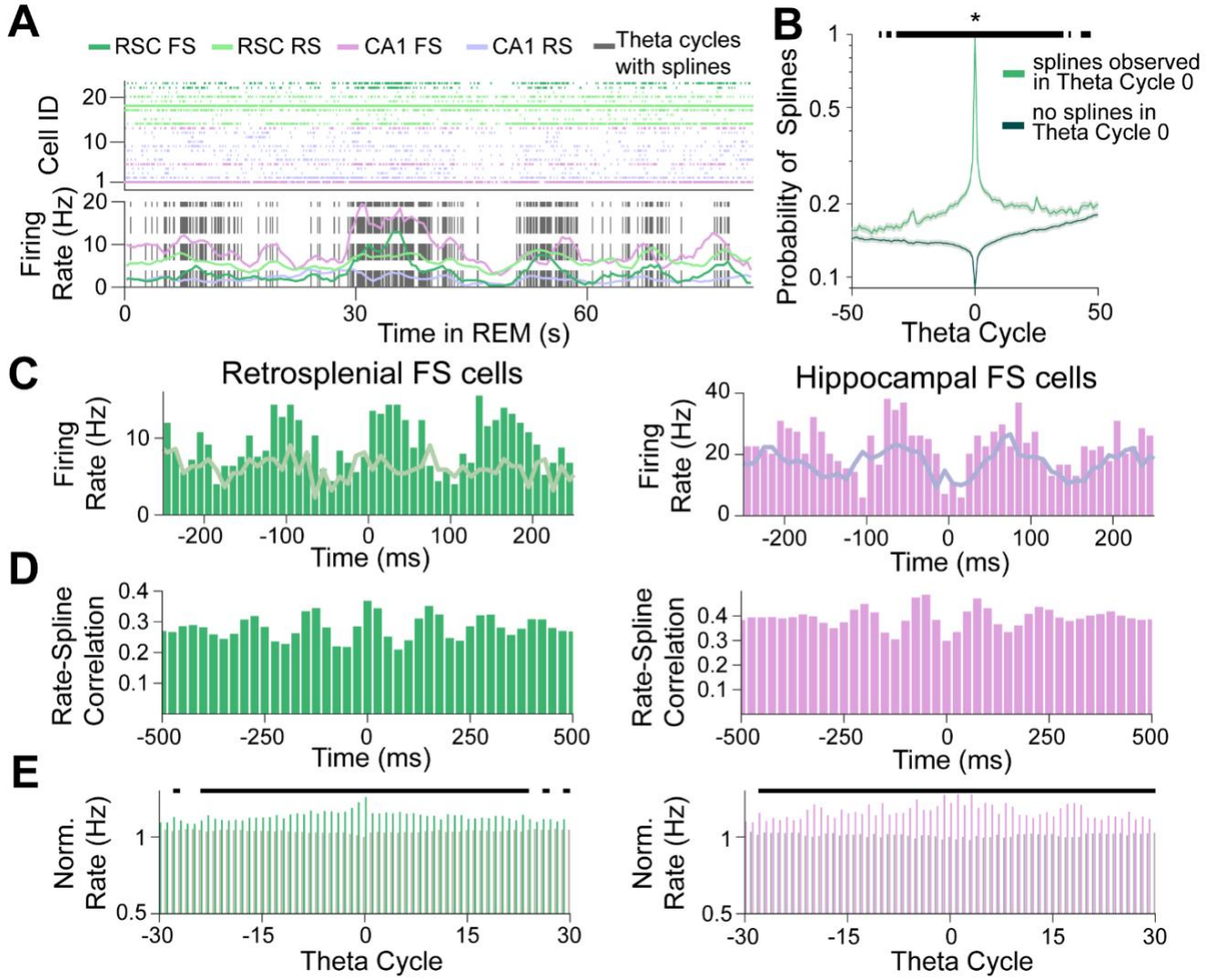
Figure 2-7. Retrosplenial splines demarcate high activity REM sleep frames.
A. Raster plot of FS and RS cells from RSC and CA1 during a single REM epoch (top), with average firing rate of each cell type plotted below. Grey dashed lines represent peaks of RSC theta cycles with splines (see Methods). Firing rates of all cells increase during theta cycles with splines. Theta cycles with splines cluster together into frames, and firing rates of both retrosplenial and hippocampal FS cells increase during the spline-rich frames, suggesting that these frames represent high activity up-states.
B. Probability of observing RSC theta cycles with splines triggered off theta cycles with (green) or without (black) splines across 3 rats from which single units were recorded during REM sleep. When theta cycle 0 contains splines, the probability of observing additional theta cycles with splines remains significantly elevated for -32 to +36 theta cycles before and after theta cycle 0 (two sample t-test, p<0.05).
C. (Left) PSTH of representative RSC FS cell triggered at the peak of RSC theta cycles with (dark green bars) and without (light green line plot) splines. Spline-triggered averages show sustained increases in both the rate and theta modulation of FS firing. (Right) Similar plot, now shown for a CA1 FS cell firing, again triggered at the peak of RSC theta cycles with (purple bars) and without (grey line plot) splines. The CA1 cell also shows sustained increases in firing rate around splines.
D. Correlation between firing rate and RSC spline power for the same FS cells shown in ***C***.
E. Normalized firing rate of FS cells across 3 rats for RSC (left, N = 41) and CA1 (right, N = 57) across ± 30 theta cycles centered on theta cycles with (green bars for RSC; purple for CA1) and without (grey bars) RSC splines. The number of cycles where the difference in firing rate is significant is shown as black bars on top (two sample t-test, p<0.05). FS cells in both RSC and CA1 thus show sustained increases in firing rates during the high-activity REM frames demarcated by retrosplenial splines.
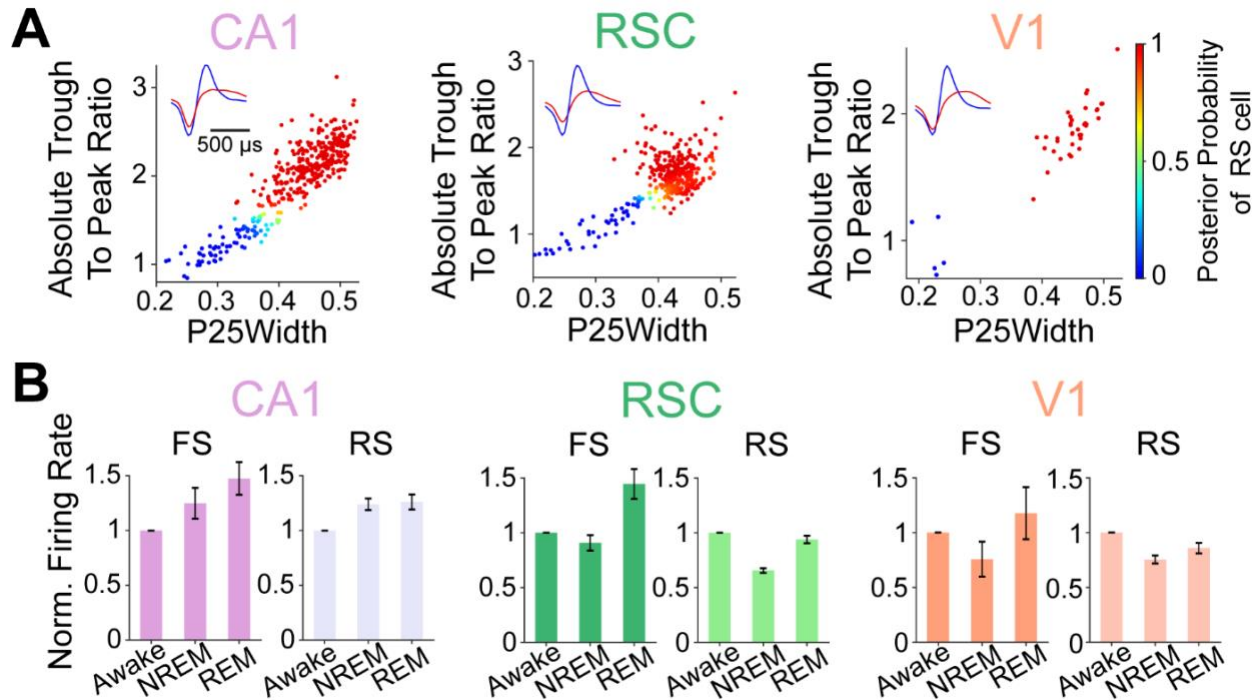
Figure 2-8. Cell classification and brain state specific firing rates across regions.
A. Features used to classify cells into putative fast-spiking (FS) and regular-spiking (RS) clusters using a gaussian mixture model. P25Width is the width of the waveform at 25% of the peak amplitude. The color bar shows the posterior probability of a cell being classified as an RS cell. Thus, red dots represent putative RS cells and blue dots represent putative FS cells. This classification identified 333 RS and 63 FS cells in CA1, 295 RS and 48 FS cells in RSC and 38 RS and 5 FS cells in V1.
B. Firing rates (normalized to awake firing rate) of FS and RS cells across CA1, RSC, and V1 during NREM sleep and REM sleep.
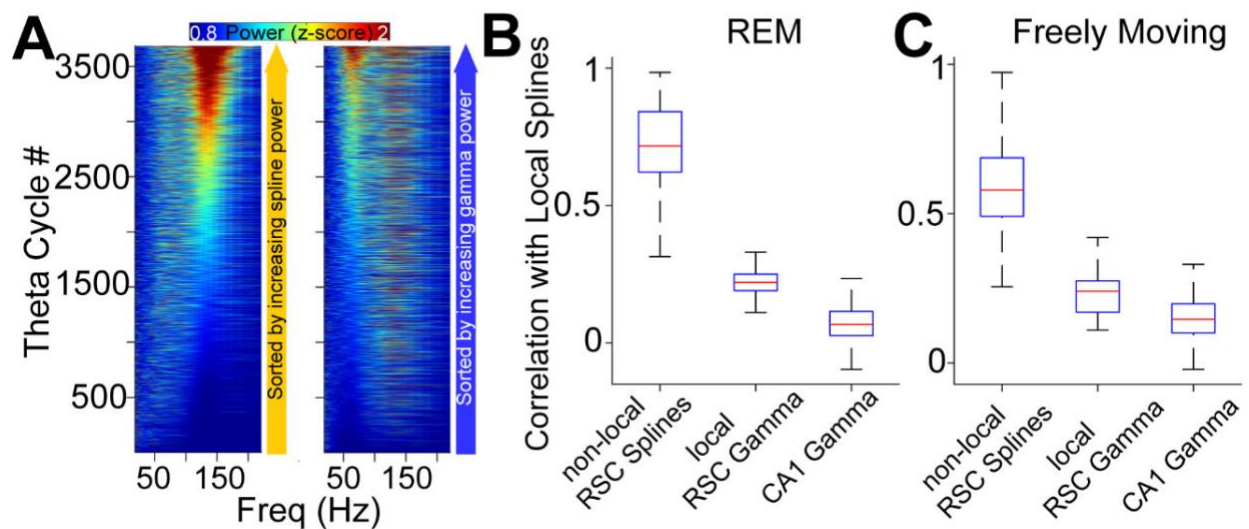
Figure 2-9. Splines are correlated across the long-axis of the retrosplenial cortex but independent of local gamma oscillations.

A. All theta cycles during an example REM epoch sorted by either spline (110-160 Hz; left) or gamma (30-80 Hz; right) power showing the independence of splines and gamma.

B. Population correlation coefficients of RSC splines with: (left) RSC splines at separate simultaneously recorded RSC locations (9 rats, 54 reference electrodes with 162 non-local RSC electrodes); (middle) RSC gamma on the same reference electrode (9 rats and 54 reference electrodes); (right) CA1 gamma (6 rats, 50 reference RSC electrodes with 175 CA1 electrodes) during REM. Spline power across distant RSC electrodes is strongly correlated and is significantly higher than correlations with local RSC gamma (rank sum test, p<0.001) and CA1 gamma (rank sum test, p<0.001). Thus, splines occur independently of RSC gamma and CA1 gamma but are strongly correlated across the long-axis of the RSC.

C. Same as **B.** but for freely moving behavior (speed>5cm/s). Spline power across distant RSC locations was strongly correlated and was significantly higher than correlations with local RSC gamma (rank sum test, p<0.001) and CA1 gamma (rank sum test, p<0.001) during awake active states.

37

2.3.3 Splines occur independently of gamma

Elevated gamma and spline power seen in the retrosplenial spectrogram and

theta phase-amplitude coupling plots raises two possibilities: 1) splines could simply be

harmonics of gamma cycles and hence would only occur when gamma cycles occurred;

or 2) splines could be distinct entities that could occur independently of gamma cycles.

To understand the relationship between splines and gamma rhythms, we sorted each

theta cycle during REM sleep first by spline power (Figure 2-9A, left) and then by

gamma power (Figure 2-9A, right). Theta cycles without splines still had gamma

oscillations, while theta cycles without gamma oscillations very often contained splines.

We confirmed this observation across the population: during REM splines and gamma

were very weakly correlated (ρ=0.22 across 9 rats and 54 local electrodes; Figure 2-9B,

middle). Similarly, RSC splines were uncorrelated with gamma oscillations in CA1

(ρ=0.07 across 6 rats, 50 reference electrodes with 175 CA1 channels; Figure 2-9B;

right). Both of these correlation results during REM sleep are consistent with similar

correlation calculations during wake states (Alexander et al., 2018). We next asked if

splines were correlated across pairs of simultaneously recorded RSC signals and found

that they were robustly correlated (ρ=0.7 across 9 rats, 54 reference electrodes with

162 non-local RSC electrodes; Figure 2-9B, left). Across the population, the correlation

of splines across distant pairs of electrodes within the RSC was significantly higher than

the correlation of splines with local gamma rhythms (rank sum test, $p<0.001$) or with

CA1 gamma rhythms (rank sum test, $p<0.001$) during both REM. Thus, splines are

distinct from gamma and most often occur independently of gamma. Instead, splines co-occur across the long-axis of the RSC.

2.3.4 Splines are also seen in mice and are strongest in the superficial layers of the granular retrosplenial cortex

While splines are highly correlated across the granular RSC (Figure 2-9B), is their strength uniform across layers or do they have a gradient in power? To find the anatomical origin of splines, we implanted three mice with silicon probes spanning both retrosplenial hemispheres, simultaneously recording from all layers of the left and right RSG, as well as the left RSD and medial hippocampal formation (Figure 2-10A). Figure 2-10B shows raw traces from all 32 simultaneously recorded channels (100 μm spacing) during a REM sleep epoch. The tip of the probe in the hippocampus showed the expected strong hippocampal gamma rhythms. Channels in retrosplenial cortex in both left and right hemisphere showed splines. Splines were strongly coupled to the peak of theta as seen in rats (Figure 2-11). To compare the strength of splines, we analyzed the channels in the left hemisphere and found that splines were strongest in the superficial layers during REM (Figure 2-10C) and decreased in amplitude with increasing distance from the midline. Gamma oscillations were also found to be strongest in the superficial layers. To quantify and compare the strength of these oscillations across layers, we grouped channels based on their distance from the midline channel with each group spanning 300 microns. A repeated measures ANOVA was conducted to compare normalized (see Methods) spline and gamma power across

39

these 4 groups. There was a significant effect of distance on spline and gamma power during REM (spline power: $F_{(3,78)} = 78$, $p<0.0001$, gamma power: $F_{(3,78)} = 26$, $p<0.0001$). Post hoc Tukey HSD test indicated that the mean spline power during REM and awake states significantly decreased with distance from midline ($p<0.0001$ all comparisons). Similarly, gamma power for the group closest to midline was also significantly higher ($p<0.0001$ all comparisons).
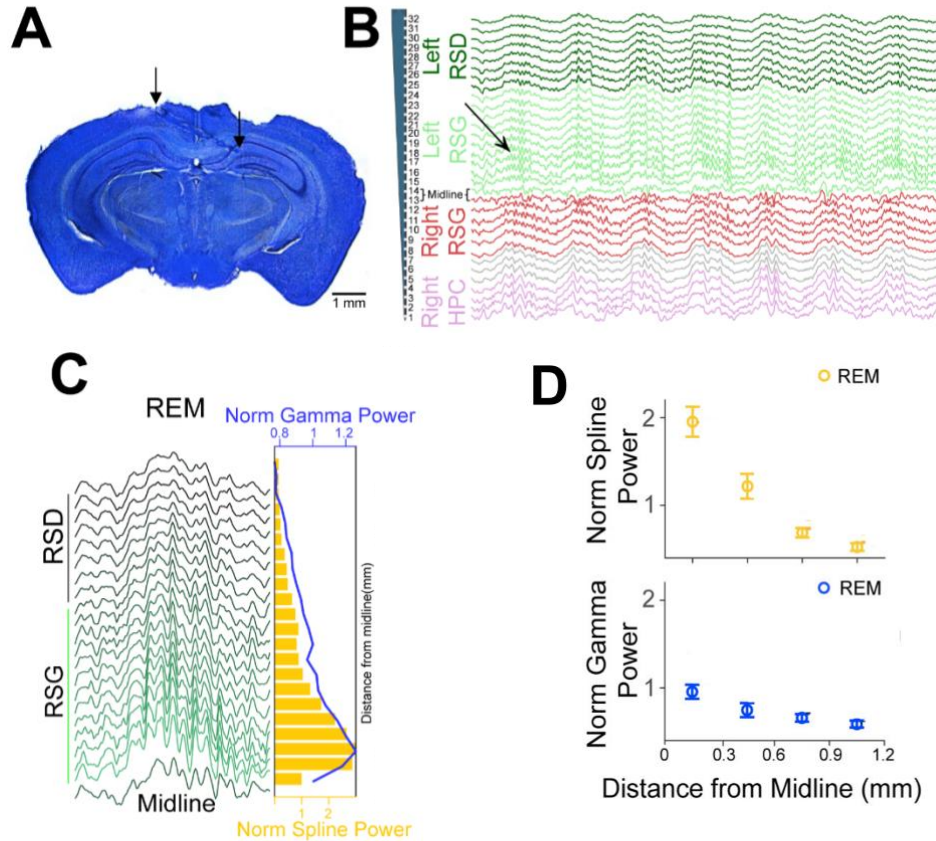
Figure 2-10. Splines are strongest in the superficial layers of the retrosplenial cortex during REM states

A. Histology showing laminar probe implanted bilaterally in the retrosplenial cortex. This allowed us to simultaneously record from multiple layers of the RSC across both hemispheres

B. Raw LFP recorded from a 32-channel probe shows splines are strongest in the superficial layers of the retrosplenial cortex. Purple traces show channels in the hippocampus, red traces in the right RSG, grey traces in Layer1 (midline channels), green traces in left RSG, and black traces in left RSD.

C. Example theta cycle across channels from the left hemisphere during REM sleep (grey trace is the midline channel closest to the first contact in left RSG). (right) Spline power (green bars) and gamma power (line plot) across channels during the entire REM session shows splines and gamma oscillations are strongest in the superficial layers

D. Normalized spline power and gamma power across 3 mice (9 sessions from REM). To quantify and compare the strength of these oscillations across layers, we grouped channels based on their distance from the midline channel with each group spanning 300 μm. A repeated measures ANOVA found a significant effect of distance from midline on spline and gamma power ($p < 0.0001$ for all cases). Similarly, gamma power for the group closest to midline was also significantly higher ($p < 0.0001$ all comparisons).

41
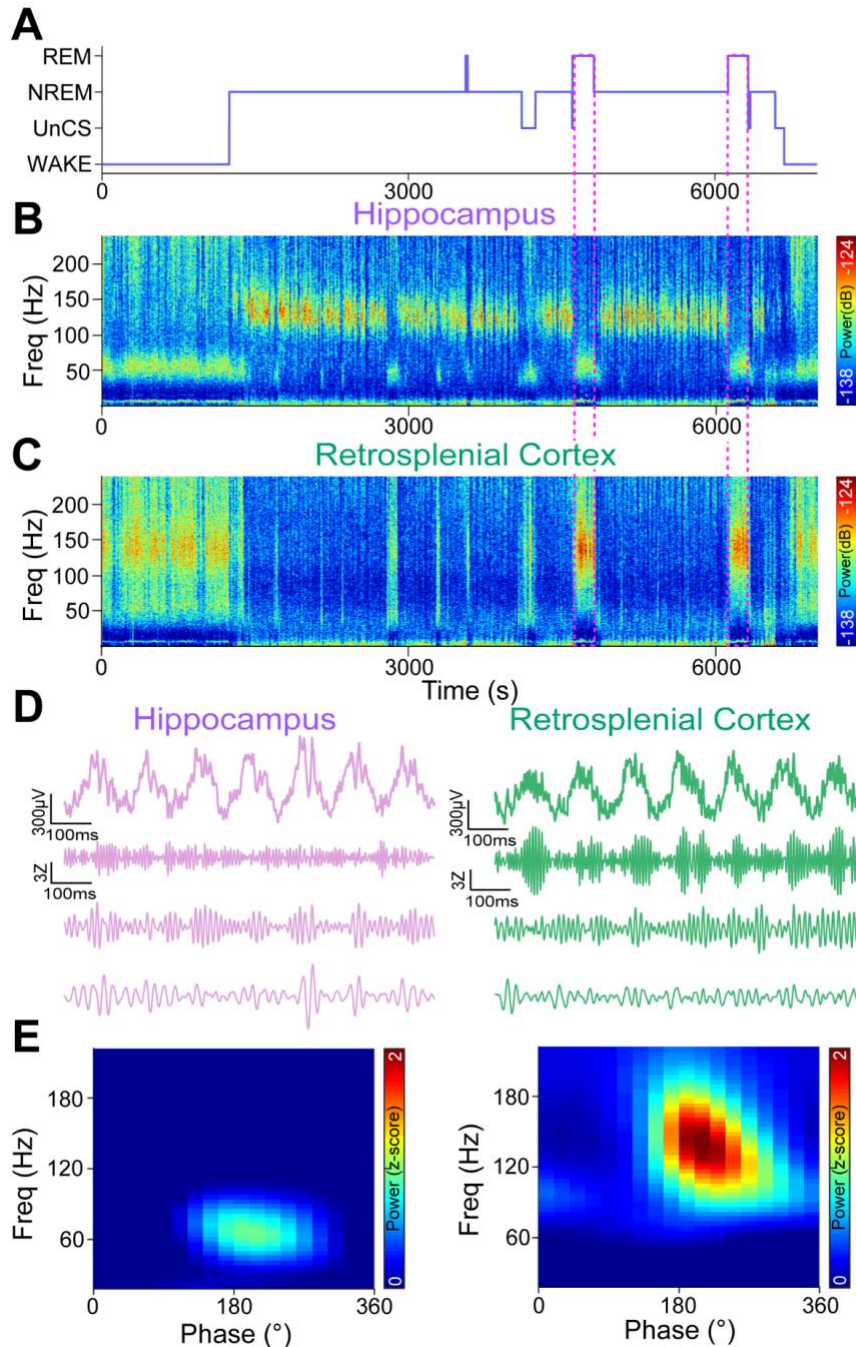
Figure 2-11. Retrosplenial splines in mice show similar properties as in rats, strongest in the RSC and strongly coupled to the peak of theta.
A. Hypnogram from a sleep session with multiple NREM-REM transitions.
B-C. Corresponding spectrograms from hippocampal CA1 and retrosplenial cortex (RSC. CA1 shows typical NREM ripples (*B*). Hippocampal NREM ripples alternate with RSC REM splines as seen in Figure 2-2B-C
D. Raw traces from CA1 and RSC show splines strongest in the RSC
E. Phase-amplitude coupling from an example REM session show splines strongly coupled to the peak of theta in RSC with gamma oscillations in CA1.
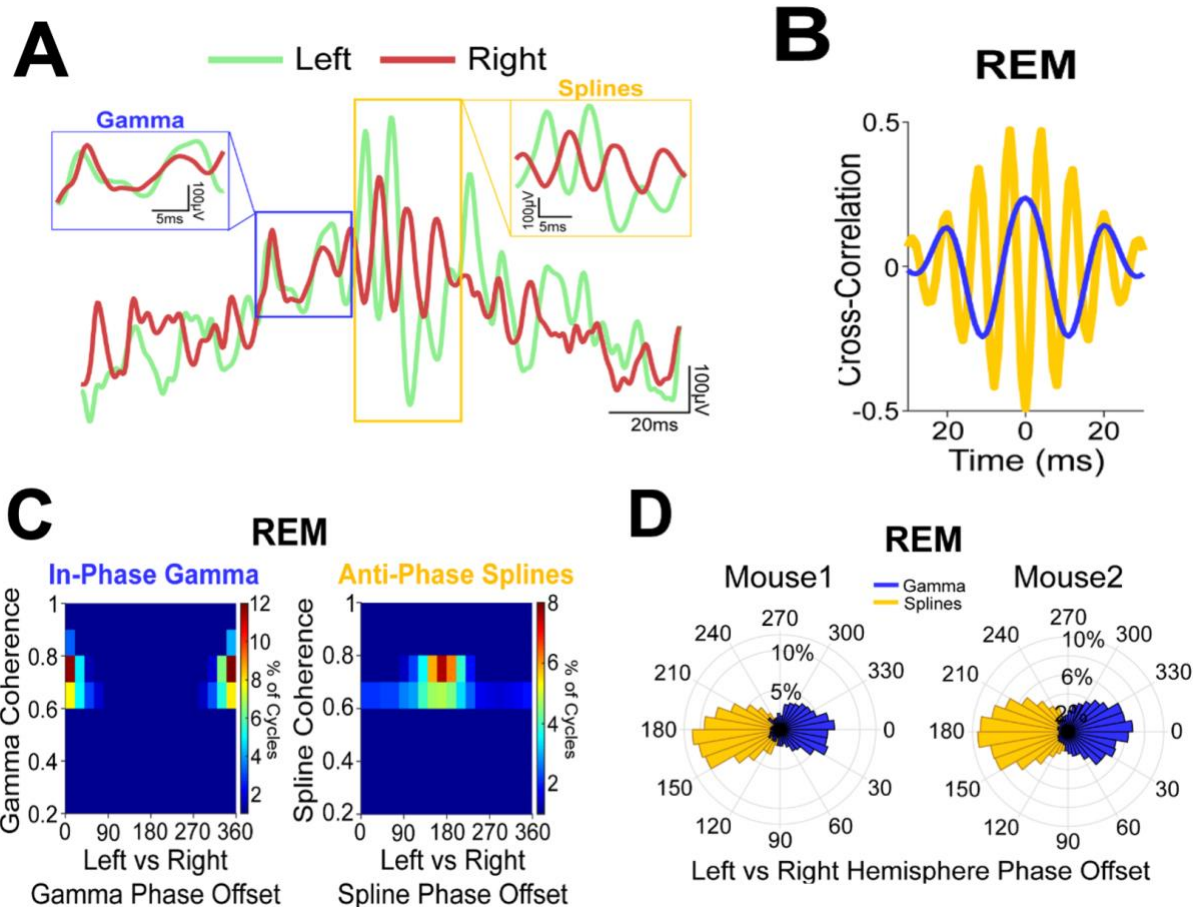
Figure 2-12. Splines are anti-phase across hemispheres while gamma oscillations are in-phase during REM sleep.

A. Example raw LFP trace during REM showing a theta cycle from the left hemisphere (green) overlaid with a simultaneously recorded LFP from the right hemisphere (red). Gamma oscillations (inset shows zoomed view) were in phase, but splines in the contralateral channel were 180 degree out of phase (inset shows zoomed view).

B. Cross-correlation from a REM session shows that splines were antiphase across hemispheres while gamma oscillations were in-phase.

C. Distribution of spline and gamma coherence magnitude and phase across 3 mice (9 sessions) shows that splines were consistently anti-phase (mean phase = 163°, kappa = 0.7) across hemispheres while gamma oscillations were in-phase (mean phase = 2°, kappa = 2.2) during REM. A Watson William test showed that there was a significant difference (p<0.0001) between mean spline phase and gamma phase across hemispheres.

D. Distribution of coherence phase between the left and right hemisphere during REM sessions from 2 mice. A distinct 180 degree offset was seen for splines as compared to gamma
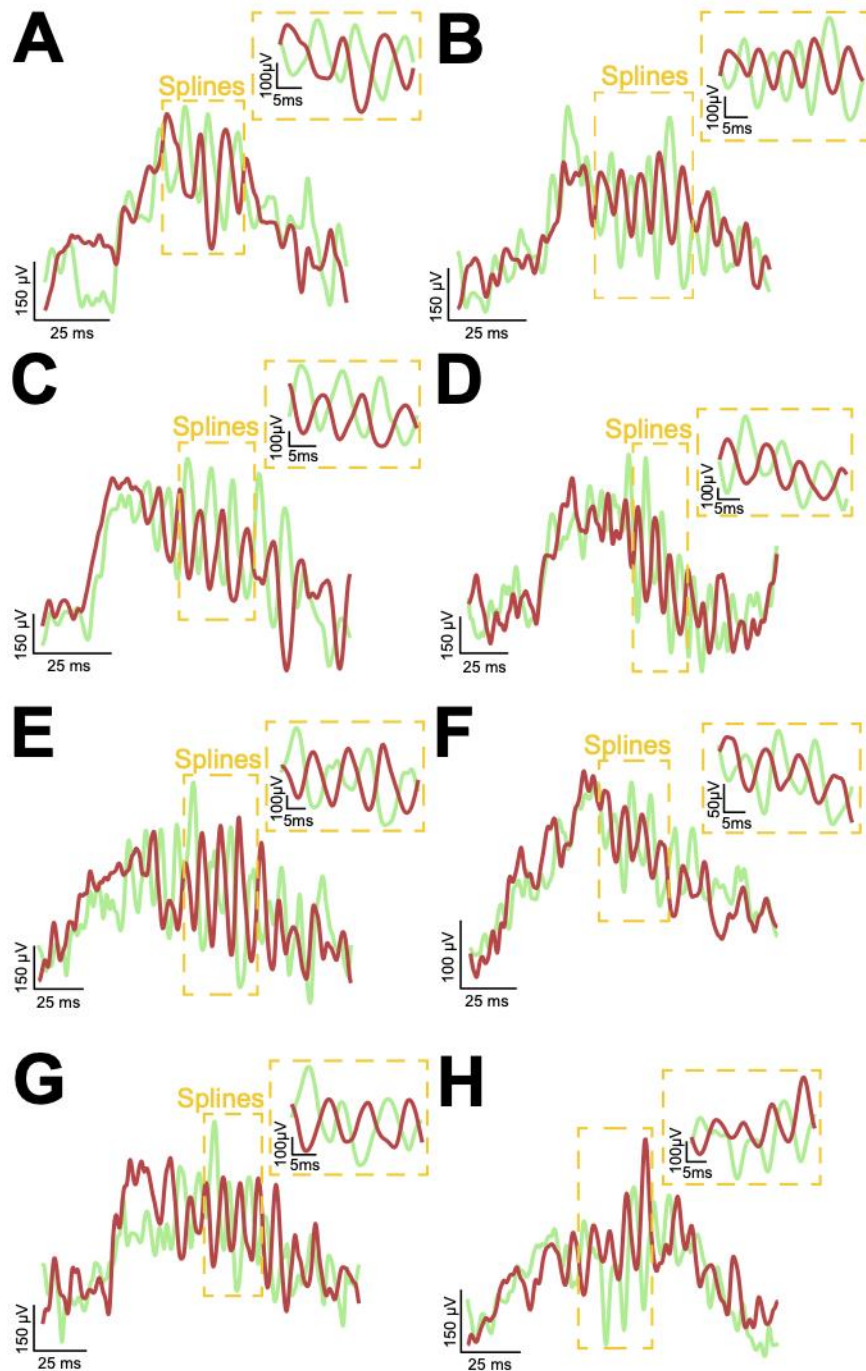
Figure 2-13. Retrosplenial splines are anti-phase across hemispheres.
Example theta cycles from 3 mice showing splines in right hemisphere were 180⁰ offset
from splines in the left hemisphere.
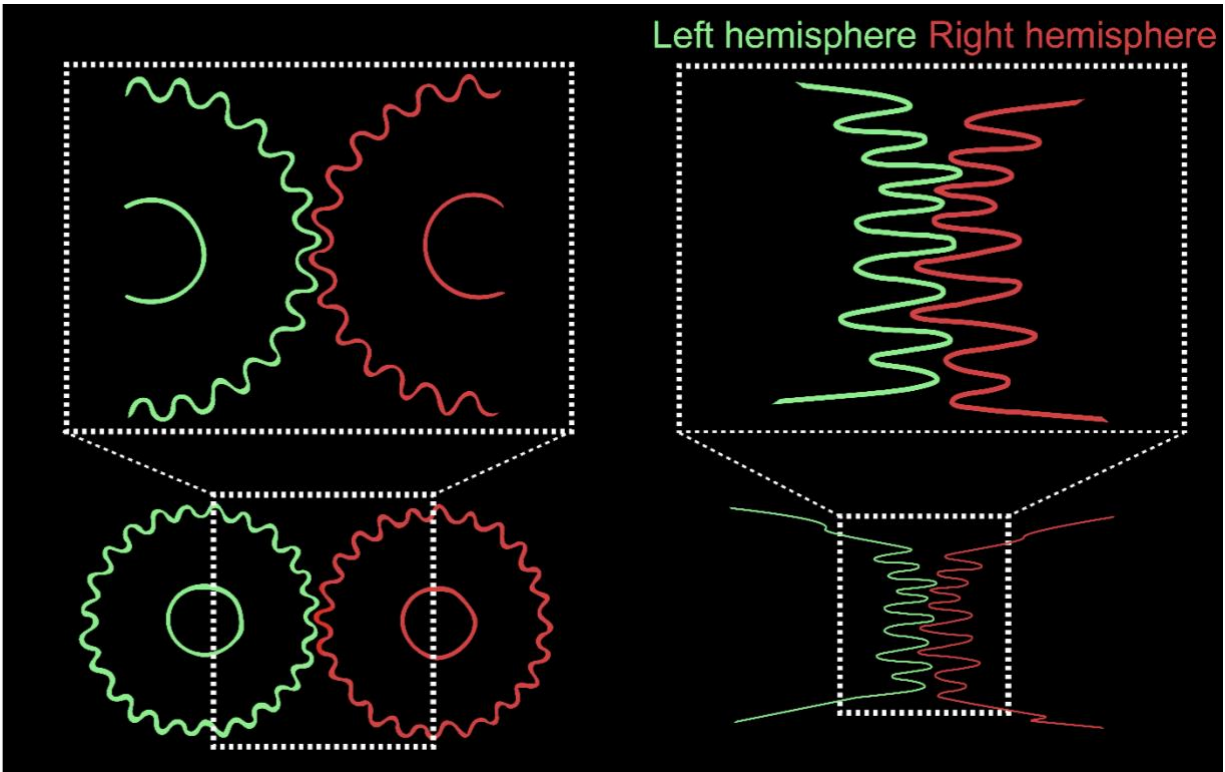
Figure 2-14. Splines: the name for fast 110-160 Hz oscillations sitting at the peak of theta and anti-phase across hemispheres.
Splines are the interlocking teeth or ridges on a mechanical gear (left) and resemble the fast oscillations phase-locked to the peak of individual theta cycles but with opposite phases across hemispheres (right).

2.3.5 Splines are anti-phase across hemispheres while gamma oscillations are in-phase during REM

Our probe recordings reveal that splines and gamma are strongest in the superficial layers of RSG. We next examined the coherence between these oscillations across hemispheres. Simultaneously recorded raw LFP traces from superficial layers of the left and right hemisphere (Figure 2-12A, 2-13) showed that splines were robustly and surprisingly anti-phase (180 degree out of phase) across hemispheres. On the contrary, gamma oscillations in the left and right hemispheres were in-phase. To further understand the phase relationship of splines and gamma across hemispheres, we computed a cross correlations between superficial channels in the left and right hemispheres from 3 mice (Figure 2-12B). Splines were consistently anti-phase across hemispheres during REM sleep. To quantify this phase relationship, we computed wavelet based coherence between superficial channels from the left and right hemisphere during the entire REM session. We analyzed the distribution of coherence phase offset for splines and gamma during REM (Figure 2-12D). Population coherence magnitude and phase distribution (Figure 2-12C) from 3 mice (9 REM sessions) showed that splines were selectively 180 out of phase across hemispheres. Gamma oscillations on the other hand were consistently in-phase. A Watson William test showed that there was a significant difference ($p < 0.0001$) between mean spline phase and gamma phase across hemispheres. It is this characteristic interhemispheric phase relationship of these theta-peak locked oscillations that led us to call them splines, the interlocking teeth on mechanical gears (Figure 2-14).

2.4 Discussion

Here, using large-scale recordings in both rats and mice, we show that theta-coupled 110-160 Hz oscillations are strongest in the superficial layers of the granular retrosplenial cortex (RSG) during REM sleep. Surprisingly, we find that these fast oscillations are the signature of anti-phase communication across hemispheres. These anti-phase 110-160 Hz oscillations are robustly anti-phase coupled across hemispheres, resembling splines, the interlocking teeth on mechanical gears. We therefore refer to them as "splines". Our findings highlight two distinct channels of rapid interhemispheric communication in the RSG during REM sleep, with gamma being in-phase and splines anti-phase.

Our study raises new questions: for REM-containing theta cycles, what mechanism drives the switch between gamma frequencies and spline frequencies? Given that splines specifically occur at the peaks of theta rhythms while gamma rhythms are coupled to the rising phase of theta, it is possible that the increased voltage of the local field during peaks of theta rhythms is one of several conditions influencing the RSC cell assemblies that generate splines. We have observed gamma in CA1, V1, and PPC, but none of these regions have high-frequency oscillations over 100 Hz coupled to the peaks of theta rhythms during REM sleep. While splines are robust in the RSG, they are not as strong in RSD. The RSG's splines may have a small amount of volume conductance to the RSD, or be generated much less strongly in the RSD due to RSD's lack of LR neurons, such that splines appear with relatively low power in RSD. The

47

properties unique to the RSG likely give rise to the mechanism that generates splines: perhaps a combination of RSG's connections with many other brain regions and that RSG contains persistently-firing low-rheobase neurons in layers 2 and 3 (Brennan et al., 2020, 2021). Furthermore, while we would expect most excitatory neuron firing to be phase-locked at or near the trough of theta (Jacobs et al., 2007), splines occur at the peaks of theta, suggesting that excitatory neurons are not the main force at play in the circuit generating splines. Since spline-rich REM frames have increased FS cell activity, FS neurons in layers 2 and 3 may be at play. A mechanism that involves signaling with retrosplenial cortex FS neurons may drive the transition from retrosplenial gamma to splines or vice versa.

We found that splines occurred in clusters spanning multiple contiguous theta cycles, which suggests that the mechanism for generating splines continues beyond the timeframe of one series of splines. It is notable that RSG theta rhythms do occur without splines. Brain rhythms dynamically couple brain regions, and are thought to modulate, filter, and redirect information (Benchenane et al., 2010; Buzsáki, 2004; Fell et al., 2001; Varela et al., 2001, Womelsdorf et al., 2007), but what is the role of RSG's cross-hemispheric coordination in information processing? It is possible that splines augment information transfer in the larger circuit through their rapid signaling. If preventing splines from occurring in REM sleep causes deficits in attention or long-term memory tasks, perhaps treatments that focus on spline restoration could help people with attention or memory disorders. Elucidating the functions of splines in learning and memory, as well as how they may change with age in Alzheimer's disease, may allow splines to serve as a biomarker.

An experiment that transects the brain only at the corpus callosum may elucidate more about spline mechanisms during REM. Low-rheobase neurons from layers 2 and 3 project contralaterally to layer 1c, layer 2, and layer 5 (Brennan et al., 2021). Since layer 2 contains strong splines, these cortico-cortico projections across the hemispheres may be key players in the generation and/or precise temporal coordination of splines. If the transection prevents completely splines from occurring, then the communication between the hemispheres by these projections is important for spline generation. If splines still occur in the RSG after the transection, but their coherence between the hemispheres is disrupted, this would indicate that projections from the contralateral RSG's layers 2 and 3 LR neurons play an important role in carrying information for cross-hemispheric coordination.

2.5 Materials and methods

2.5.1 Subjects

2.5.1a Rats

A total of 9 rats were used (seven male Long-Evans and two male Sprague Dawley rats (Charles Rivers Laboratories, Wilmington, MA)). Rats were socially housed in a temperature- and humidity-regulated colony maintained on a 12:12 h light:dark cycle. Experiments were carried out in the dark phase for the Long-Evans and during the light phase for the Sprague Dawley rats. All procedures followed the NIH guidelines

and were approved by the Institutional Animal Care and Use Committee of the University of Michigan.

2.5.1b Mice

Subjects were three male C57BL/6 mice. Mice were socially housed until implant then singly housed in a temperature- and humidity-regulated colony maintained on a 12:12 h light:dark cycle. Experiments spanned both the light and dark phases. All procedures followed the NIH guidelines and were approved by the Institutional Animal Care and Use Committee of the University of Michigan.

2.5.2 Surgery

Animals were handled and habituated in the recording room for at least 3 days before surgery. Animals were prepared for surgery via isoflurane induction and atropine administration (subcutaneous, 0.05 mg/kg) and then maintained on a surgical anesthetic plane with 1-2.5% isoflurane for the duration of the procedure. Each of the mice was implanted with custom titanium ring headposts (MIC583; H.E. Parmer Company; Nashville TN) and silicon probes (made by NeuroNexus Technologies). Skull screws were implanted for references (cerebellum, posterior parietal cortex, or frontal cortex) and ground (posterior-lateral cerebellum). All implants and injections were performed using a stereotaxic apparatus (Stoelting Co, Wood Dale, IL) and Picospritzer III (Parker Hannifin; Hollis, NH) with a 1.0mm OD glass pipette.

2.5.3 Implant locations

Mice with headposts and chronic probe implantations targeted bilateral retrosplenial cortex, and unilateral subiculum/CA1 hippocampus (AP -2.30; ML range -1.6 to +1.2 on a 55 degree angle; with the driven axis spanning superficial to deep RSC, across the midline, through contralateral RSG, corpus callosum and into subiculum/CA1). They were implanted with NeuroNexus Technologies A1x32-Edge-5mm-100-177-H32 package probe. Post-perfusion histology confirmed the expected recording location for 2 of the 3 probe placements, though one of these confirmed mice had the implant slightly anterior to the target (AP= -2.06). Tissue damage prevented precise histological electrode localization for the third animal; however, recorded data strongly matches results obtained in the other animals. This suggests that probe placement was at the targeted coordinates.

2.5.4 Electrophysiological recordings

2.5.4a Rat recordings

Electrophysiological signals for all Long-Evans rats were acquired continuously and digitized at 32kHz on a 64-channel Digital Lynx SX acquisition system with Cheetah recording and acquisition software (Neuralynx, Inc, MT). Single-unit activity was bandpass filtered between 600Hz-6kHz, and local field potentials were bandpass

filtered between 0.1Hz-8kHz. The final signals were stored with timestamps and position information for subsequent analysis. Electrophysiological signals for the Sprague Dawley rats were amplified, filtered (0.1Hz – 8kHz), and digitized at 30 kHz on the head stage (RHD 2132, Intan Technologies Inc, CA) then passed to an Open Ephys acquisition system (http://open-ephys.org). Electrophysiological recordings started after three to five days of recovery from surgery. Nine rats were recorded during sleep-wake states. In each daily session, rats were placed in a 36 cm diameter octagon turntable and allowed to sleep or move freely for up to 6 hours.

2.5.4b Mouse recordings

Electrophysiological signals were amplified, filtered (0.1Hz – 8kHz), and digitized at 30 kHz on the head stage (RHD 2132, Intan Technologies Inc, CA) then passed to an Open Ephys acquisition system (http://open-ephys.org). Electrophysiological recordings started after three to five days of recovery from surgery. Three mice were recorded during sleep-wake states. They were placed in a 31.75 cm by 31.75 cm open box and allowed to sleep or move freely for up to 10 hours.

2.5.5 Histology

After the last recording session, mice and rats were deeply anesthetized with isoflurane and the final recording site was marked with an electrolytic lesion (~20 µA for 10 seconds). Animals were then perfused with 1x PBS, followed by 4%

paraformaldehyde. The brains were post-fixed for 24 hours in 4% paraformaldehyde and then transferred to a 30% sucrose solution until the time for sectioning. The brains were sectioned at a thickness of 40 μm and stained for Nissl material.

2.5.6 Single unit analysis

Spikes associated with putative individual units were isolated offline based on waveform characteristics and using a variety of partially automated and manual techniques (Offline Sorter, Plexon, Inc.). In case of rats, spike waveforms of isolated units were then used for classifying the sorted units into FS and RS cells. Absolute ratio of the trough to peak amplitude of the spike waveform and the width of the spike waveform at 25% of the amplitude from the peak (P25Width) - were used for an automated clustering using a Gaussian Mixture model (Figure 2-8). The posterior probability of the clusters identified boundary values of the amplitude ratio and P25Width, and we thereafter defined FS cells as those having a P25Width < 0.38 and absolute trough to peak amplitude < 1.5.

2.5.7 Movement analysis

Green and red LEDs on the headstages were used to track rats. Extracted position(x,y) was smoothed with a 1Hz low-pass filter before computing speed as $\sqrt{\frac{dx^2}{dt} + \frac{dy^2}{dt}}$

2.5.8 LFP analysis

All electrophysiological data was analyzed using custom written MATLAB based

programs, unless specifically stated otherwise. The raw LFP was down-sampled to

1000 Hz for all subsequent analysis after verifying that the down-sampling did not affect

the results obtained.

2.5.9 Spectral analysis

LFP power spectral analysis for classifying brain states and assessing brain-state

specific oscillations (Figure 2-2) was performed using multi taper analysis with a window

size of 5 seconds, time-bandwidth product of 1, and a taper of 1 using the chronux

toolbox (https://chronux.org/). Spectral whitening was performed to equalize the

variance across frequencies and adjust for the 1/f decrease in power with frequency that

leads to overemphasis of lower frequencies. A second order autoregressive model (A)

was used to model the raw LFP, and then a filter of [1;-A] was applied to normalize

power across frequencies. To obtain the whitened spectrum, the same multi taper

analysis as mentioned above was performed on this filtered LFP. While plotting spectra

in Figure 2-2, 60Hz noise and its third harmonic was removed by setting power in a 1

Hz range of 59.5 – 60.5 Hz and 179.5 – 180.5Hz as NaN and interpolating power in

these 1 Hz ranges based on the power values in the nearest frequency bins.

2.5.10 Brain state classification

Brain state was classified into awake, NREM, REM, and unclassified (UnCS) using a semi-automated algorithm (Montgomery et al., 2008). EMG was filtered in the 0.5-100 Hz range. Thereafter, a root mean square value of the filtered EMG (rmsEMG) was computed using moving windows of 1 s with an overlap of 0.5 s. Movement speed was averaged using 1 s moving windows with an overlap of 0.5 s. High rmsEMG (> 0.25) and high speed (> 1 cm/s) were used to identify awake epochs. High delta (0.5-4 Hz) power (greater than the median z-scored power), low EMG, and lack of movement were used to identify NREM. Two NREM epochs separated by less than 3s were combined together as one. A NREM epoch of less than 4 seconds was discarded. Theta ratio was computed as the ratio of theta (5-11 Hz) power to a sum of delta and alpha (12-30 Hz) powers (theta / (delta+alpha)). An epoch with high theta ratio, detected by a threshold of 0.5+median z-scored theta ratio, accompanied with low EMG and speed, was classified as REM. NREM and REM epochs lasting less than 4s were not analyzed. Time epochs which did not meet any of the above criteria were labeled as unclassified. A custom-made graphical user interface (programmed in MATLAB) that displayed the computed classification, LFP, EMG, speed, and video recordings of each session was then used to verify every brain state manually. Ambiguous epochs were labeled as unclassified. The resulting final hypnogram had a resolution of 0.5 s.

2.5.11 Normalized spline and ripple power

To obtain a normalized value of power in the 110-160 Hz (spline) and ripple (110-190Hz) frequency ranges during REM and NREM sleep, respectively, we used the ratio

of power in the respective high frequency band to broadband (1-230 Hz) power both prior to and after spectral whitening.

2.5.12 Theta phase-amplitude coupling

Morlet wavelet spectrogram for each channel was computed for the entire session and z-scored to normalize every frequency across the session. Morlet windows were defined as described previously (Tallon-Baudry et al., 1997). A wavelet family of 7 was chosen. To get the Morlet spectrogram, the signal was convolved with the wavelets. To compute the theta phase coupling across frequencies, individual theta cycles were detected by filtering in the 6-12 Hz range. Thereafter, every time bin in the theta cycle was converted to phase by linear transformation such that the start (trough) of a theta cycle was 0 degrees and end (next trough) by 360 degrees. Power across frequencies in a theta cycle was obtained from the wavelet spectrogram values in the corresponding theta cycles over 20-degree bins. Phase-amplitude coupling for a session during REM was computed by averaging across theta cycles in the corresponding brain state.

2.5.13 Modulation index

Strength of the phase-amplitude coupling was quantified using modulation index as defined previously (Tort et al., 2010). Power in the spline band (110-160 Hz) over 20 degree bins across a theta cycle was obtained from the phase-amplitude matrix

computed above. This power was normalized by the sum of spline power across all 360

degrees of the theta cycles, and its distance from a uniform distribution was computed

using the following formula:

$$MI = \frac{\sum_{i=1}^{N} A(i) \times \log\left(\frac{A(i)}{U(i)}\right)}{\log(N)}$$

where A is normalized spine amplitude for the respective bins, U is the uniform

distribution, and N is the total number of bins. The resulting measure, known as the

modulation index (MI), quantifies the extent of phase-amplitude coupling between the

two rhythms.

2.5.14 Kappa

We also computed the concentration parameter kappa of the von Mises

distribution to quantify the strength of theta phase-amplitude coupling using the CircStat

toolbox for MATLAB (Berens, 2009).

2.5.15 Detecting splines within theta cycles

Using the wavelet spectrogram, each theta cycle had an associated spectrum.

Theta cycles were thereafter sorted by power in the 110-160 Hz range. Change point

analysis was used to detect theta cycles with splines (Figure 2-6).

2.5.16 Spline correlations across brain regions

To correlate power in various frequency bands across tetrodes in a given session, theta cycles with peaks closest to those of a reference tetrode in RSC were found. Thereafter, spline (110-160 Hz) power in those matched theta cycles was correlated across other simultaneously recorded RSC tetrodes, which we refer to as non-local RSC spline correlation (Figure 2-9). Spline-gamma correlations for RSC were computed by correlating spline power to gamma (30-80 Hz) power in theta cycles from the same reference tetrode (local gamma, Figure 2-9). Spline-gamma correlation with respect to CA1 was performed by correlating spline power in the RSC reference tetrode to gamma power in matched theta cycles from simultaneously recorded CA1 channels. To compute correlation between theta amplitude and spline power, we defined theta amplitude of a single-cycle as the difference between the z-scored amplitude values of the peak and starting trough.

2.5.17 Spline-single unit firing rate correlation

To assess firing rates in theta cycles, each spike was assigned to a theta cycle extracted as discussed above. Correlations between spline power and firing rate was computed over 25 ms bins.

2.5.18 Coherence analysis

Wavelet spectrogram as described above was used to compute coherence magnitude and phase for the entire REM session. 5 ms smoothing windows were used. Thereafter, mean spline and gamma coherence magnitude and phase were computed over individual theta cycles. For analyzing modulation of coherence by theta phase, mean coherence magnitude and phase offset were computed over 20 degree bins.

2.5.19 Spike phase locking

Spline cycles were extracted by filtering the LFP in 110-160Hz range and finding local troughs and peaks. Spikes were assigned a phase with the starting trough as 0, peak as 180, and end of the cycle as 360 degrees. For spike phase locking to gamma, the LFP was filtered in the 30-80 Hz range to identify local troughs and peaks and phase assignment of spikes was performed as for splines.

2.5.20 Statistical tests

For *in* vivo electrophysiology experiments, a Wilcoxon rank sum test was used to compare power in spline and ripple bands and the strength of phase amplitude coupling of splines across brain regions. A significant deviation from normality was confirmed using the Shapiro-Wilk test before using rank sum tests. To compare the correlation of splines across pairs of simultaneously recorded RSC signals with those recorded from CA1, we used a rank sum test. Two-sample t-tests were used to compare firing rates between theta cycles with and without splines. Thereafter, post hoc comparisons using

the Tukey HSD test were conducted. The CircStat toolbox for MATLAB (Berens, 2009) was used for computing kappa and performing Watson William test for comparing mean spline coherence phase distributions of ipsilateral and contralateral channels. Rayleigh's Z (CircStat toolbox) was used to test the significance of phase locking of units to splines from both local and contralateral channels. An alpha value of 0.05 was used throughout.

2.6 Acknowledgements

CHAPTER 3: Oscillations of the Retrosplenial Cortex in Awake Behavior and Running Speed

A modified version of this chapter was submitted as: Ghosh M*, Yang F*, Rice SP*, Hetrick V, Lorenzo Gonzalez A, Siu D, Brennan EKW, John TT, Ahrens AM, Ahmed OJ. 2021. Running speed controls two distinct modes of rapid interhemispheric communication.

3.1 Abstract

The ability to track the speed of movement is required for successful spatial navigation. To better understand the role of running speed in retrosplenial cortex (RSC) oscillations, we implanted mice with silicon probes across the hemispheres of the RSC bilaterally and had them run either head fixed on a spherical treadmill or in a T-maze where they could move around freely. We found that splines, a unique high-frequency oscillation we have previously identified during REM sleep, are also seen during active running. As during REM, both gamma and splines were strongest in superficial layers of the RSC, with gamma in-phase across the hemispheres and splines anti-phase. We also found that splines increased in power, gained more interhemispheric coherence, and became more strongly coupled to the peaks of theta rhythms at faster running speeds. This suggests that the retrosplenial cortex employs two modes of rapid interhemispheric coordination, splines and gamma, to encode speed information or to consolidate sensory information.

3.2 Introduction

How the brain keeps track of position, speed, and direction in navigation involves the communication between many structures. The retrosplenial cortex receives inputs from the medial entorhinal cortex (van Wijngaarden et al., 2020) and the hippocampus (Yamawaki et al., 2019b), which are interconnected with each other (Ahmed and Mehta 2009; Fyhn et al., 2004) and both encode speed (Moser et al., 2008; Ahmed and Mehta, 2012). Speed signaling has been reported in a subset of all RSC neurons (Alexander et al., 2020a).

The source of the neural speed signal comes from motor systems and sensory systems, both of which have connections to the retrosplenial cortex. The vestibular system also encodes directional and speed signals (Cullen and Taube, 2017; Valerio and Taube, 2016). We would therefore expect that experiments involving head fixation, which holds the head still, would take away the portion of the speed signal that may be modulated by encoding by the vestibular system, and that if the visual scene is also constant, the speed signal would largely be relayed through the self-generated motion of the limbs and the motor efference copy, an anticipatory signal of sensation and motion (Cullen, 2014).

By using large-scale recordings in both rats and mice, we show that theta-coupled 110-160 Hz oscillations are strongest in the superficial layers of the granular retrosplenial cortex (RSG) during head-fixed running. Although these high-frequency oscillations in RSG have previously been described during navigation as "high gamma"

(Alexander et al., 2018), we have determined that they are distinct from gamma. Surprisingly, we find that these fast oscillations are the signature of anti-phase communication across the hemispheres of RSG. These anti-phase 110-160 Hz oscillations across hemispheres resemble splines, the interlocking teeth on mechanical gears. We therefore refer to them as splines. This anti-phase coupling has previously been identified by our lab in mice and rats during REM sleep (Chapter 2). We found that anti-phase coupling of splines is robust during running, including head-fixed running, and becomes even more precise at faster running speeds.

3.3 Results

3.3.1 Splines are anti-phase across hemispheres while gamma oscillations are in-phase during awake active states

Our probe recordings reveal that splines and gamma are strongest in the superficial layers of RSG during active awake states (Figure 3-2), similar to how they are strongest in the superficial layers of RSG during REM sleep (Figure 2-10), decreasing in power at sites more lateral to the midline. As rapid inter-hemispheric communications occurred in REM, we wanted to know how splines and gamma oscillations are modulated by this inter-hemispheric communication during active waking states. Simultaneously recorded raw LFP traces from superficial layers of the left and right hemisphere (Figure 3-3A) showed that splines were robustly and surprisingly anti-phase (180 degrees out of phase) across hemispheres during awake

behaving states. On the contrary, gamma oscillations in the left and right hemispheres were in-phase. Again, like with REM sleep, splines were consistently anti-phase across hemispheres during freely moving states. To quantify this phase relationship, we computed wavelet based coherence between superficial channels from the left and right hemisphere during the freely moving sessions. We analyzed the distribution of coherence phase offset for splines and gamma during freely moving (Figure 3-3B) behavior. Population coherence magnitude and phase distribution (Figure 3-3C) from 3 mice (9 REM and 9 freely moving sessions) showed that splines had a mean phase of 180 degrees, such that they were anti-phase across hemispheres. Gamma oscillations, on the other hand, were consistently in-phase. A Watson William test showed that there was a significant difference ($p < 0.0001$) between mean spline phase and gamma phase across hemispheres.
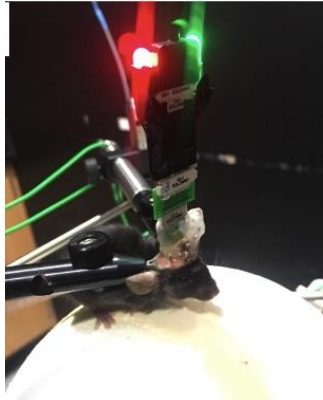
Figure 3-1. Head-fixed spherical treadmill system.
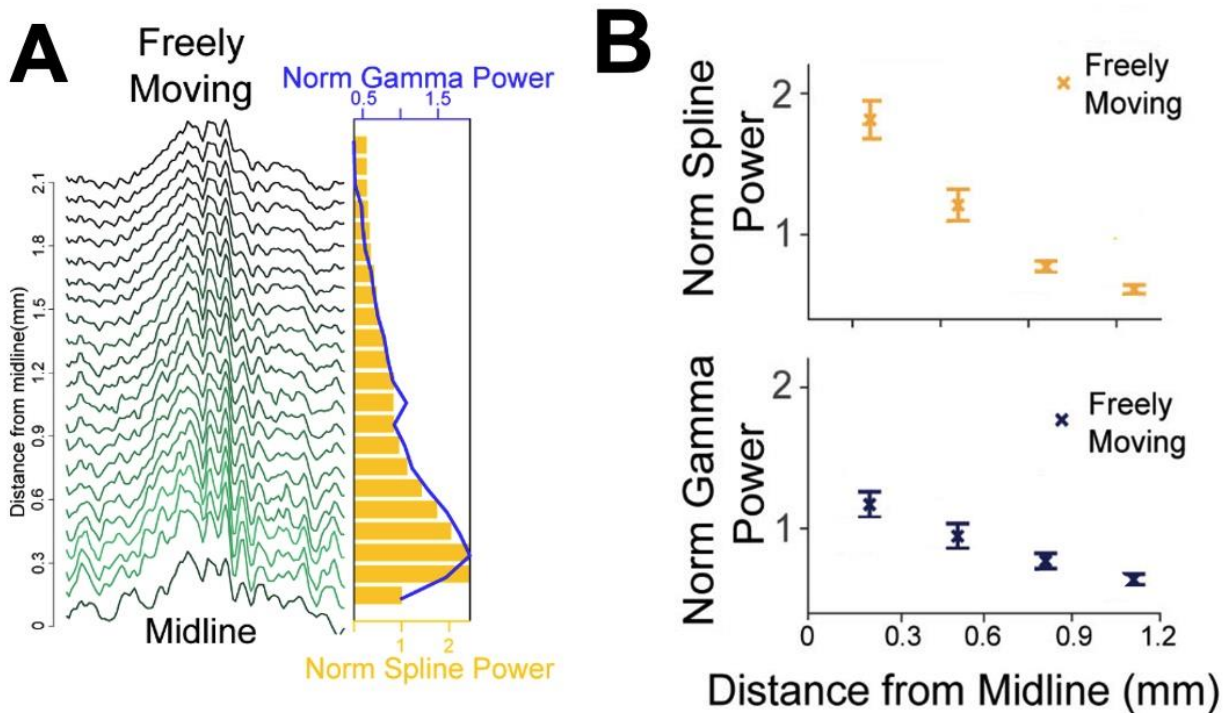
Figure 3-2. Splines are strongest in the superficial layers of retrosplenial cortex during awake active states.

A. Example theta cycle across channels from the left hemisphere during a T-Maze session (speed >5cm/s) shows the decrease in spline power with increasing distance from the midline.

B. Normalized spline power and gamma power across 3 mice (9 sessions). To quantify and compare the strength of these oscillations across layers, we grouped channels based on their distance from the midline channel with each group spanning 300 μm. A repeated measures ANOVA found a significant effect of distance from midline on spline and gamma power (p<0.0001). Post hoc Tukey HSD test indicated that the mean spline power during awake states significantly decrease with distance from midline (p<0.0001 all comparisons). Gamma power for the group closest to midline was also significantly higher (p<0.0001 all comparisons).
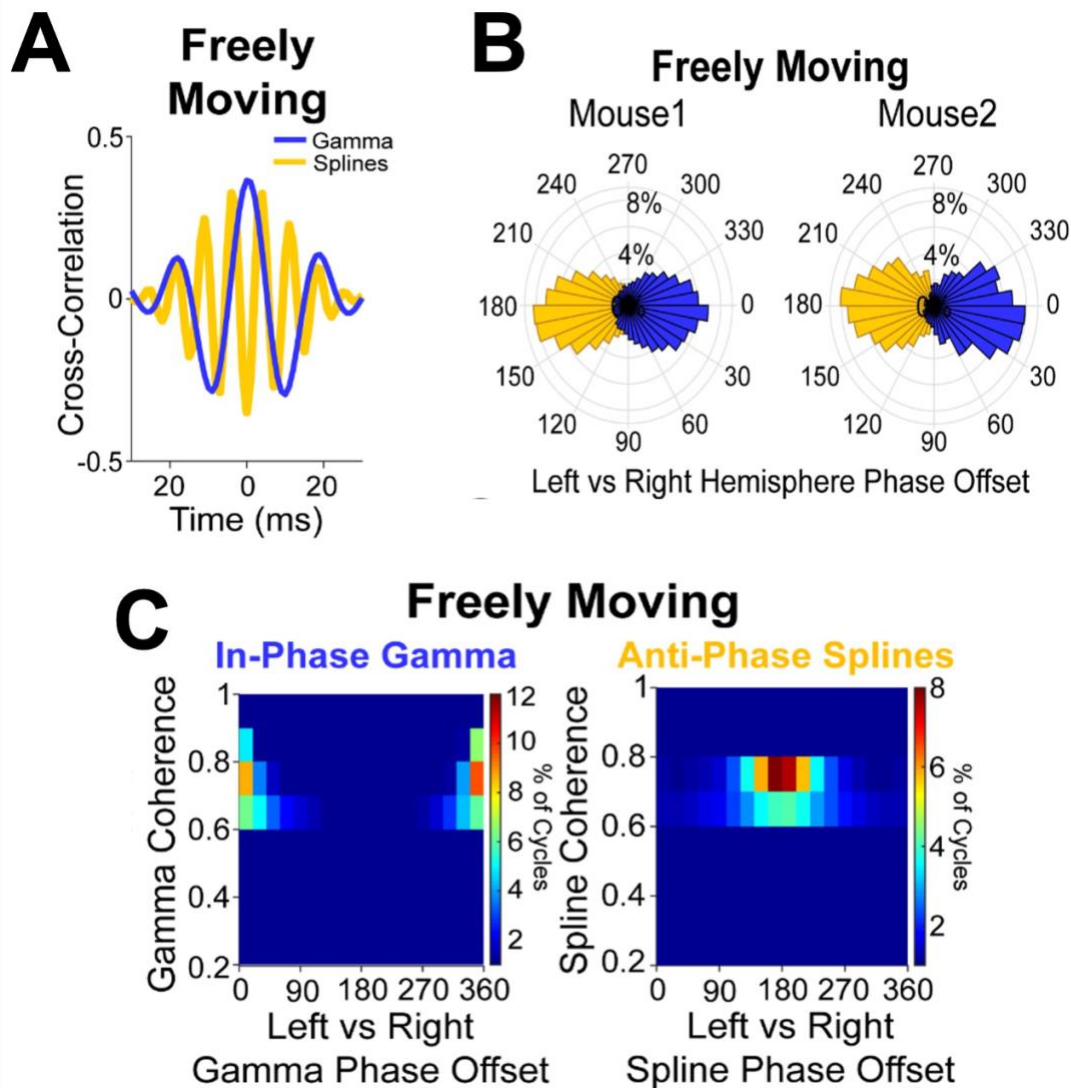
Figure 3-3. Splines are anti-phase across hemispheres while gamma oscillations are in-phase during awake active states.

A. Cross-correlation during a freely moving session shows that splines were antiphase across hemispheres while gamma oscillations were in-phase. All analysis was performed for linear speeds >5 cm/s.

B. Distribution of coherence phase between the left and right hemisphere during freely moving sessions from 2 mice. A distinct 180 degree offset was seen for splines as compared to gamma.

C. Distribution of spline and gamma coherence magnitude and phase across 3 mice (9 sessions) shows that splines were consistently anti-phase (mean phase = 180°, kappa = 0.9) across hemispheres while gamma oscillations were in-phase (mean phase = 2.2°, kappa = 1.6) during freely moving sessions. A Watson William test showed that there was a significant difference (p<0.0001) between mean spline phase and gamma phase across hemispheres.
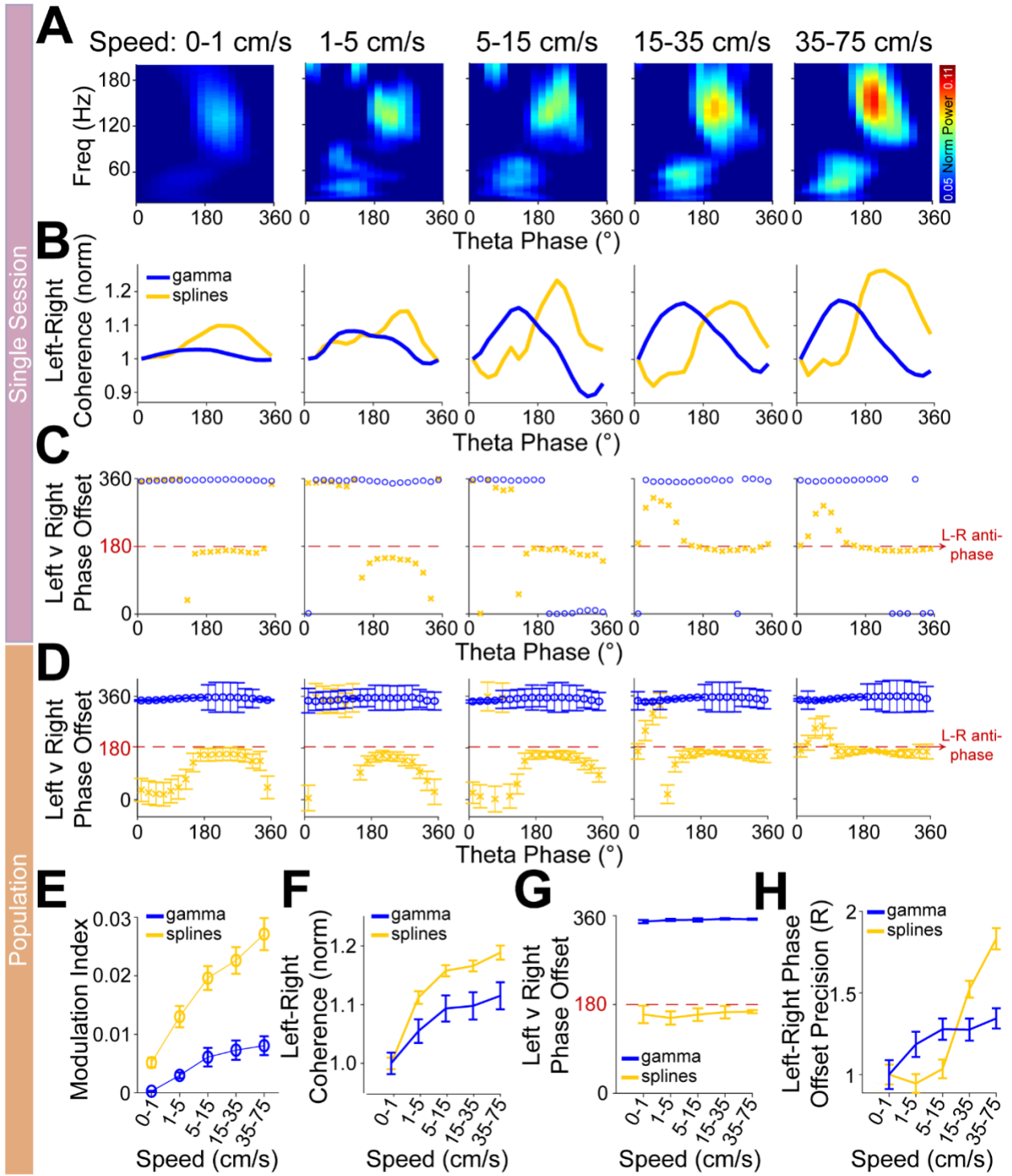
Figure 3-4. Spline and gamma coherence increase with increasing running speed.
A. Example phase-amplitude coupling with increasing running speed. Similar to rats on a linear track, strength of coupling of splines to theta increased with increase in running speed when head-fixed mice run on a spherical treadmill.
B. Spline and gamma coherence magnitude as a function of theta phase at increasing running speed from an example session. Note that spline coherence was maximum at the peak of theta corresponding to the maximum spline power within a theta cycle as seen in *A* above. Similarly, gamma coherence peaked during the rising phase of theta. The coherence magnitude is normalized by the value at theta phase 0 (starting trough of the theta cycle)
C. Spline and gamma coherence phase as a function of theta phase with increasing running speed from the same session as B. Splines were anti-phase specifically at the peak of theta when their power and coherence was the highest.
D. Spline and gamma coherence phase-offset as a function of theta phase across the population (3 Mice, 9 sessions). Splines were consistently anti-phase at the peak of theta.
E. Similar to rats, there was a significant effect of speed on the modulation index of splines ($F_{(4,32)} = 43$, $p<0.001$). Though there was a significant effect of speed on the modulation index of gamma as well ($F_{(4,32)} = 15$), the effect size at 35-75 cm/s compared to 1-5cm/s was higher for splines($d=2.1$) as compared to gamma ($d=1.4$).
F. Spline and gamma coherence magnitude increased with running speed. There was a significant effect of speed on the magnitude of spline ($F_{(4,32)} = 30$, $p<0.001$) and gamma coherence ($F_{(4,32)} = 27$, $p<0.001$). The effect size for the increase in coherence at 35-75 cm/s as compared to 1-5 cm/s was stronger for splines ($d = 1.18$) as compared to gamma ($d = 0.58$). Coherence values were normalized to the slowest speed (0-1 cm/s) bin.
G. Splines were anti-phase and gamma oscillations were in-phase with increasing running speed. Note however that the variance in the phase-offset decreased with increasing running speed.
H. The left-right phase offset precision (mean resultant vector (R)) increased with increasing running speed. The effect size at 35-75 cm/s to that at 1-5 cm/s was stronger for splines ($d = 1.4$) as compared to gamma ($d = 0.4$). All values were normalized to the slowest speed (0-1 cm/s) bin.

3.3.2 Running speed controls two distinct bands of interhemispheric communication

We next investigated how both anti-phase spline coupling and in-phase gamma coupling change with running speed. We used head-fixed mice running on a spherical treadmill to precisely control and track running speed. Phase-amplitude coupling of splines to theta in the superficial layers of RSG in a given hemisphere increased with running speed, with similar relationships seen for theta-gamma coupling (Figure 3-4A, E). A repeated measure ANOVA revealed that there was a significant effect of speed on the modulation index of splines ($F (4,32) = 43$, $p<0.001$) and gamma ($F(4,32) = 15$; $p<0.001$). The effect size of increase in modulation index at the fastest speeds (35-75 cm/s) to that at the slowest running speeds (1-5 cm/s), was higher for splines ($d = 2.1$) as compared to gamma ($d = 1.4$). We next asked if interhemispheric coherence was also similarly modulated by running speed. To do so, we first aimed to understand how spline interhemispheric coherence changed within a theta cycle. Similar to theta phase amplitude coupling (seen in a single hemisphere), we found that the magnitude of spline-spline interhemispheric coherence within a theta cycle was highest at the peak of theta (Figure 3-4B). Gamma-gamma interhemispheric coherence was maximum at the rising phase of theta at all running speeds sampled. At this stage it is important to note that splines only happen near the peak of theta, and correspondingly spline-band interhemispheric coherence is strongest when splines occur. Thus, we predicted that splines should be anti-phase across hemispheres only near the peak of theta. We confirmed this by analyzing the phase of spline-band interhemispheric coherence as a function of theta phase: splines were strongly anti-phase near the peak of theta, but

coherence in this same 110-160 Hz frequency range was highly variable at other

phases, where splines are rarely seen (Figure 3-4C,D). Next, to assess change in

interhemispheric coherence with speed, we analyzed the coherence magnitude and the

interhemispheric spline-spline or gamma-gamma phase offsets at various speeds.

There was a significant effect of speed on the magnitude of spline ($F(4,32) = 30$,

$p<0.001$) and gamma coherence ($F(4,32) = 27$, $p<0.001$). The effect size for the

increase in coherence at the fastest speeds (35-75 cm/s) as compared to the slowest

running speeds (1-5 cm/s) was stronger for splines ($d = 1.18$) as compared to gamma (d

$= 0.58$) (Figure 3-4F). Spline interhemispheric communication remained consistently

anti-phase at all running speeds examined, while gamma remained consistently in-

phase (Figure 3-4G). Importantly, the precision of the interhemispheric communication

increased with increasing running speed. To quantify this, we analyzed the circular

spread in the mean phase across a theta cycle using the mean resultant vector(R).

There was a significant effect of speed on the mean resultant vector (R) for the phase

offset for splines ($F(4,32) = 6$, $p<0.001$) and gamma ($F(4,32) = 18$, $p<0.001$). Similar to

coherence magnitude, the effect size at faster speeds (35-75 cm/s) compared to slower

speeds (1-5 cm/s) was stronger for splines ($d = 1.4$) as compared to gamma ($d = 0.4$).

Thus, running speed increases spline-spline interhemispheric communication by making

this coupling stronger and more precisely anti-phase. Gamma-gamma interhemispheric

communication also becomes stronger and more precisely in-phase at faster running

speeds. However, changes in spline-band interhemispheric communication are more

pronounced than changes in gamma-band interhemispheric communication. These

results show that the two distinct speed-controlled bands of anti-phase (splines) and in-

phase (gamma) interhemispheric communication can co-exist, with the timing of each form of interhemispheric communication controlled by the phase of theta.

We hypothesized that anti-phase communication in the spline frequency band should result in phase-locking of retrosplenial neurons to opposite phases of spline oscillations across hemispheres. Figure 3-5B shows example phase locking distributions of a single unit and a multi-unit recorded from superficial RSC during awake and REM respectively. These units show a clear preference to fire at the trough of local splines and the peak of contralateral splines. Of the 20 single units recorded during REM and active states from the superficial layers, 18 were significantly phase locked to local splines while 14 to contralateral splines (Figure 3-5C). All 19 multi-units recorded were significantly phase locked to both local and contralateral splines (Figure 3-5D). The mean phase distribution of cells with significant phase locking showed that cells were consistently phase locked to the trough of local splines and the peak of contralateral splines (Figure 3-5E and F). Similar analysis for gamma showed significant phase locking of cells to the trough of both local and contralateral gamma (Figure 3-8).
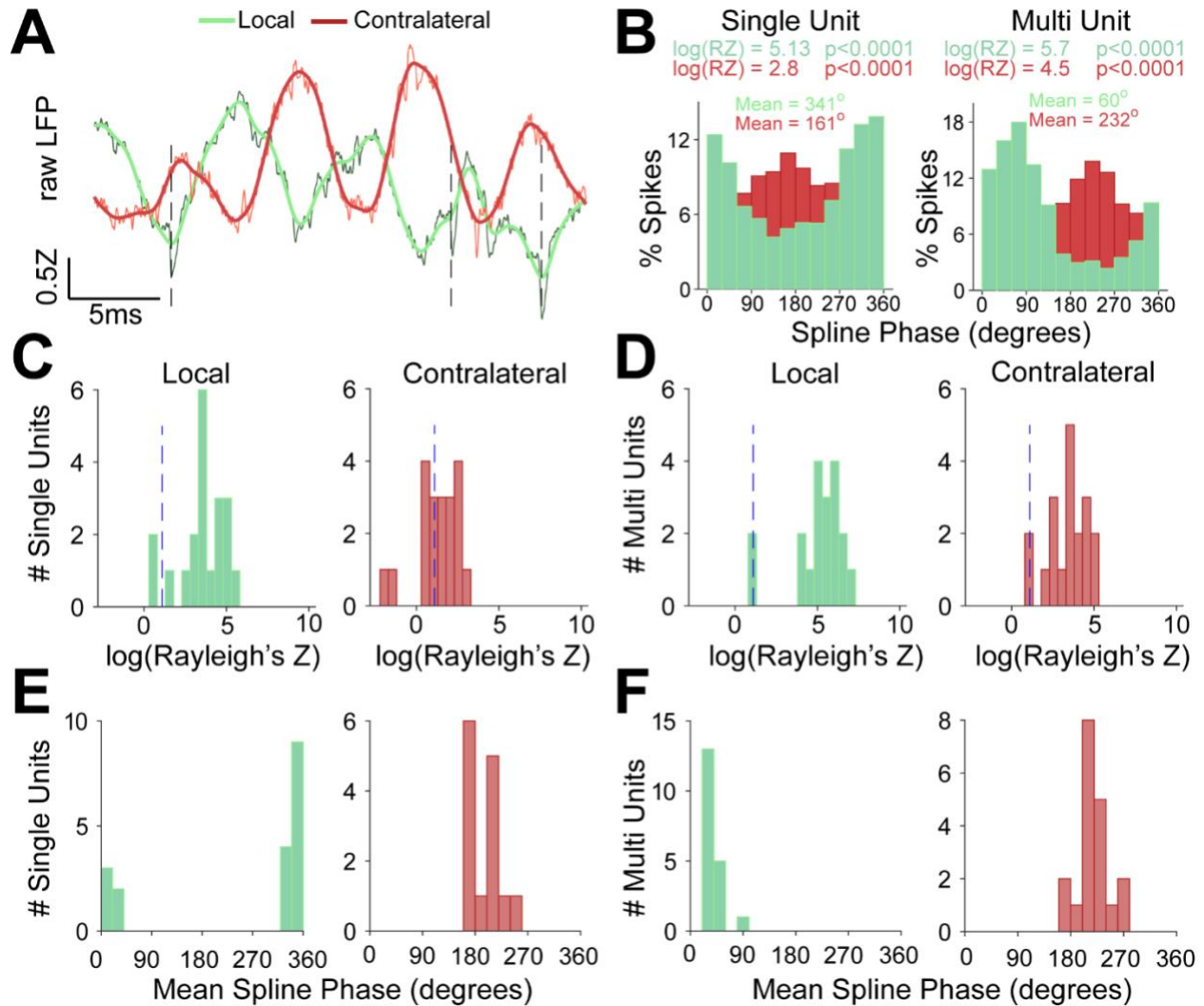
Figure 3-5. Spikes phase-lock to the trough of splines in the ipsilateral LFP and to the peak of splines in the contralateral LFP.

A. Example raw (black) and 3-500 Hz filtered (green) LFP showing spikes (dotted lines) at the trough of splines. A simultaneously recorded raw (orange) and 3-500 Hz filtered (red) LFP from a contralateral channel shows the same spikes locked to the peak of splines.

B. Phase locking from a single-unit and multi-unit to local (green) and contralateral (red) splines showing significant phase locking to the trough of local splines (*single unit*: mean phase = 341°, ln(Rayleigh's Z) = 5.13, p<0.001; *multi-unit*: mean phase = 60°, ln(Rayleigh's Z) = 5.7, p<0.001) and the peak of contralateral splines (*single unit*: mean phase = 161 , ln(Rayleigh's Z) = 2.8, p<0.001; multi-unit: mean phase = 232, ln(Rayleigh's Z) = 4.5, p<0.001)

C. Distribution of Rayleigh's Z for all recorded cells during REM and active states. The blue dotted line at ln(3) = 1.098 indicates the threshold for significance (alpha = 0.05). Of the 20 cells, 18 were significantly phase locked to local splines while 14 were also phase-locked to contralateral splines.

D. Same as **C** for multi-units recorded during REM and active states. All 19 units were significantly phase locked to local and contralateral splines.
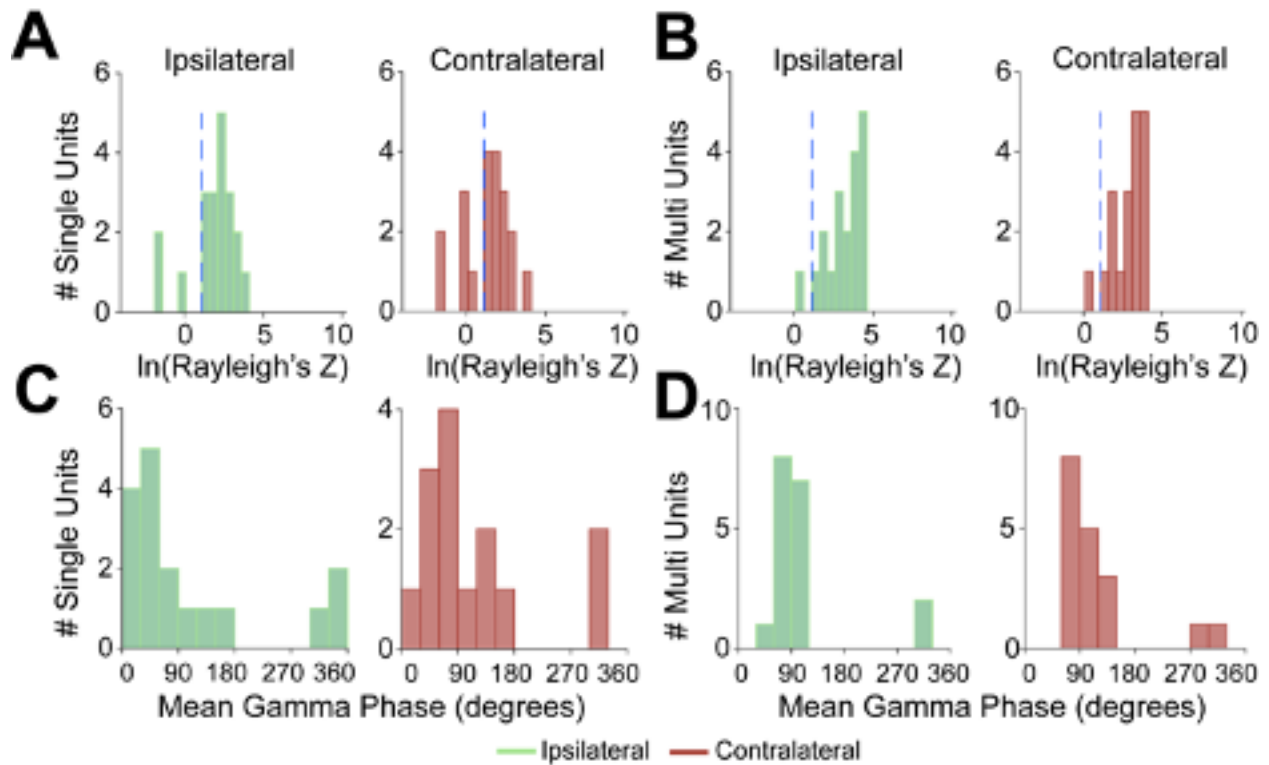
Figure 3-6. Spikes phase-lock near the trough of both ipsilateral and contralateral gamma rhythms.
A. Distribution of Rayleigh's Z for all recorded cells during REM and active states. The blue dotted line at $\ln(3) = 1.098$ indicates the threshold for significance (alpha = 0.05). Of the 20 cells, 17 were significantly phase locked to ipsilateral gamma while 14 were phase locked to contralateral gamma.
B. Same as **A.** for multi-units recorded during REM and active states. Of the 19 units, 18 were significantly phase-locked to local (ipsilateral) gamma and 18 to contralateral gamma.
C. Mean gamma phase distribution of the significantly phase-locked cells. There was no significant difference between the preferred phase distributions for ipsilateral vs contralateral gamma rhythms (Watson Williams test, $p = 0.16$).
D. Same as **C.** for multi-units. Once again, there was no significant difference between the ipsilateral and contralateral gamma preferred phase distributions (Watson Williams test, $p = 0.25$).

74

3.4 Discussion

In this study, we have analyzed retrosplenial cortex oscillatory dynamics during head-fixed running. The properties of hippocampal gamma rhythms are known to be controlled by running speed (Sheeran and Ahmed, 2020; Ahmed and Mehta, 2012; Chen et al., 2011; Kemere et al., 2013). Our results show that interhemispheric RSG coherence in both the gamma and spline bands increases with running speed in head-fixed mice, with a much stronger effect on splines (Fig. 3-4). Gamma rhythms become more precisely in-phase across RSG hemispheres at faster speeds while splines become more precisely anti-phase, with the effect size again being larger for splines (Fig. 3-5). Our results on gamma rhythms agree with recent studies, which demonstrated that interhemispheric gamma coherence is more strongly in-phase during more demanding and more successfully-executed tasks (Bland et al., 2020; Cho et al., 2020). In contrast, our finding of increased interhemispheric spline coherence at faster speeds shows that more strongly activated brain states, such as running faster (Ahmed and Mehta, 2012), can also improve and sharpen anti-phase communication between the two RSG hemispheres. Both in-phase gamma and anti-phase spline coherence can be altered by changes in running speed.

This sharper interhemispheric coherence for splines and gamma rhythms at faster running speeds likely contributes to the retrosplenial cortex's ability to process sensorimotor information during higher speeds of navigation. The faster externally-referenced and self-generated motion cues that come with increased running speed may drive higher spline power. The prevalence of local connectivity from fast-spiking

inhibitory neurons (Brennan et al., 2020) along with the drive from navigationally-relevant projections such as the subiculum (Yamawaki et al., 2019a, Brennan et al., 2021), the anterior thalamic nuclei (Brennan et al., 2021), and the medial septum (Robertson et al., 2009) would allow RSG neurons to generate greater feedforward inhibition as the mouse runs faster.

3.5 Materials and methods

Methods were identical to those in Chapter 2 with the following additions.

3.5.1 Mouse recordings

For controlled running speed, three of the mice were head-fixed on a 7 inch diameter spherical treadmill and were free to choose whether to run or not (Figure 3-1). These sessions lasted 30-60 minutes. For self-generated navigational behavior, two of the three C57BL/6 mice (both of whom were also recorded during sleep) were trained to run in a T-maze, which allowed mice to move freely for 30 minutes. The T-maze had a long arm of 76.2 cm divided by a central arm of 30.5 cm. Walls were 10 cm high. All arms and walls were uniform in color and pattern.

3.5.2 Head-fixed speed analysis

To assess modulation of coherence by running speed, five speed categories were chosen: 0-1, 1-5, 5-15, 15-35, 35-75 cm/s. These speed bins were chosen to represent the full range of running speeds keeping the number of theta cycles in each bin nearly the same. Each theta cycle was assigned a speed value by computing speed at the peak of a theta cycle. Thereafter, theta cycles corresponding to each speed category were chosen and phase-amplitude coupling, as mentioned above, was obtained for those theta cycles. Each theta cycle was assigned the peak coherence in that cycle. Coherence phase corresponding to the peak coherence magnitude was then assigned to each theta cycle. Thereafter, averaging over theta cycles for each speed bin was performed. The mean resultant vector (CircStat toolbox) of the distribution of mean coherence phase was computed for every speed bin.

3.5.3 Statistical tests

Two-sample t-tests were used to compare firing rates between theta cycles with and without splines. To understand the relationship of theta amplitude and phase-amplitude coupling on splines and gamma with running speed, theta cycles were divided into 3 speed groups (slow [10-20 cm/s], medium [20-35 cm/s], and fast [35-55 cm/s]). Since the same channels were used for each of the three groups, a repeated measures ANOVA was performed on theta amplitude and modulation index across these speed groups. Thereafter, post hoc comparisons using the Tukey HSD test were conducted. The CircStat toolbox for MATLAB (Berens, 2009) was used for computing kappa and performing Watson William test for comparing mean spline coherence phase

distributions of ipsilateral and contralateral channels. Rayleigh's Z (CircStat toolbox) was used to test the significance of phase locking of units to splines from both local and contralateral channels. A repeated measures ANOVA was used to test the effect of speed on coherence magnitude and modulation index for head-fixed set-up. Cohen's d was used to quantify effect size between the 35-75 cm/s speed and 1-5 cm/s speed bin. 1-5 cm/s was chosen as the reference for comparing effect of running speed instead of 0-1 cm/s since 0-1 cm/s included epochs of non-movement as well. An alpha value of 0.05 was used throughout.

3.6 Acknowledgements

CHAPTER 4: Conclusions and Future Directions

4.1 Results and implications

Our results demonstrate that there are two distinct modes of rapid cross-hemispheric coordination that occur in the retrosplenial cortex both during REM sleep and during awake movement. One of these modes is gamma rhythms, which are in-phase across the hemispheres. The other mode is splines, which are antiphase across the hemispheres. The retrosplenial cortex can rapidly switch between these two mechanisms of interhemispheric communication. While gamma rhythms are coupled to the rising phase of theta, splines are precisely coupled to the peaks of theta rhythms. Spline power is independent of theta amplitude. Splines also become more precisely anti-phase with higher running speed. As splines are at their highest power during REM sleep, this also suggests splines could play a role in memory consolidation processes.

Splines are distinct from sharp wave ripples. Sharp wave ripples occur during NREM sleep and awake inactivity. Splines occur during REM sleep and awake activity, suggesting that splines are distinct from sharp wave ripples and not volume conducted from the hippocampus. Since splines are strongest during REM sleep, this implies that their role in information transfer could be more critical during REM sleep than during active behavior. Splines may serve as a biomarker and a target for treatment of

79

cognitive dysfunction, as several conditions, including Alzheimer's disease (Lakmache et al., 1998), post-traumatic stress disorder (Saar-Ashkenazy et al., 2016), and depression (Guo et al., 2013), involve interhemispheric communication impairments.

4.2 Potential mechanisms of spline generation

4.2.1 The role of cell type properties

Fast-spiking inhibitory neurons can be driven to fire at a wide range of frequencies (8-200 Hz), while excitatory pyramidal neurons only amplify lower frequency oscillations (Cardin et al., 2009). As light pulses increase in frequency, FS neurons (Connors and Gutnick, 1990) and LR neurons retain a high probability of firing while the regular-spiking excitatory neurons attenuate in their response (Brennan et al., 2020). These properties of cortical circuitry allows inhibitory neurons to generate gamma rhythms. Fast-spiking inhibitory neurons are also by far the most active cell type during sharp wave ripples, allowing these super fast oscillations to occur in hippocampus (Bähner et al., 2011; Klausberger et al., 2003; Schlingloff et al., 2014).

4.2.2 The role of oscillation properties

Through sorting theta cycles by spline power and sorting theta cycles by gamma power, we have found that theta cycles that contain strong spline power do not necessarily contain strong gamma power. This lack of correlation between power of

gamma and power of splines within theta cycles provides strong evidence that splines are distinct from gamma rhythms.

What is happening with gamma rhythms, which are also a mode of cross-hemispheric coordination? Other groups have explored mechanisms of gamma-theta coupling outside of the RSC. Segneri et al. performed analyses of theta-nested gamma rhythms, noting that theta-gamma locked states happen more often in ING than in PING (Segneri et al., 2020). In the hippocampus's theta-gamma code, different theta phases represent different spatial locations, while the gamma rhythm defines items in messages with multiple parts (Lisman and Jensen, 2013). Higher theta-gamma phase-amplitude coupling has been associated with stronger memory performance in the hippocampus (Vivekananda et al., 2021) and in the frontal region of the brain (Goodman et al., 2018). It is possible that theta-gamma coupling strength in the RSG also serve as a biomarker for better memory. In the RSG, firing rates of all cells increase during theta cycles that contain splines, but more work is needed to determine which cell types are firing and when during gamma versus splines.

It is questionable what sends the circuit dynamics past the tipping point of gamma rhythms to generate splines at the peaks of theta cycles that do contain splines. The FINO mechanism that generates sharp wave ripples would allow for an oscillation over 100 Hz. We think that splines are generated by a mechanism similar to the FINO mechanism.

Not all theta cycles contain splines, and it is currently unknown precisely what determines whether theta cycles do versus do not contain splines. Notably, splines occur in temporal clusters have a high probability of happening in clusters for -32 to +36

adjacent cycles of theta, this means that the mechanism for splines may involve a behavioral timescale of about 5-10 seconds during REM.

4.2.3 The role of connectivity

Locally, the fast-spiking inhibitory neurons of the RSG display 100% fast-spiking to fast-spiking connectivity (Brennan et al., 2020). While the inhibitory to excitatory connectivity is 53%, the excitatory to inhibitory connectivity is 16% in the RSG. The only local excitatory to inhibitory synapses have LR neurons as the presynaptic neurons. This means LR neurons likely have some influence on FS neuron firing rates.

By its connectivity, RSG neurons are strongly controlled by inhibition (Brennan et al., 2020). Strong and fast connectivity between inhibitory neurons allow the FS-FS synapses to generate high-frequency oscillations via an interneuron gamma mechanism (Viriyopase et al., 2016), as both the strength and of inhibitory postsynaptic potentials generated by FS neurons would lead to strong fast synchrony. The RSG's cell type connectivity gives rise to the prevalent inhibition that would make fast oscillations possible

4.2.4 The role of the cholinergic system

As theta rhythms are mediated by cholinergic inputs (Colgin, 2013) and splines occur specifically at the peaks of theta rhythms, this suggests that acetylcholine may shape some aspects of spline generation. The MSDB's cholinergic neurons project to

both the retrosplenial cortex (Robertson et al., 2009) and the hippocampus (Colgin, 2013). Acetylcholine allows for the generation of theta rhythms during movement and REM sleep (Colgin, 2013). Basal forebrain acetylcholine release is especially strong during REM sleep (Vazquez and Baghdoyan, 2001), which is also where we have observed the highest spline power. Since splines are strongest in brain states correlated with theta rhythms and higher levels of acetylcholine release, this indicates acetylcholine is not only involved in the mechanism of gamma-theta coupling, but also in shaping splines.

Howe et al., 2017 measured LFPs in the prefrontal cortex, blocking either mAChRs or nAChRs (Howe et al., 2017). They found that missed cues were not associated with theta-gamma coupling and that mecamylamine (nicotinic AChR antagonist) and telenzepine (muscarinic AChR antagonist) disrupted theta-gamma coupling. Newman et al., 2013 measured LFPs from medial entorhinal cortex and found that scopolamine (muscarinic AChR antagonist) administration selectively decreases peak-locked high gamma power (Newman et al., 2013). Furthermore, administration of PNU-282987, an alpha-7 nAChR agonist, to the hippocampus did not significantly increase gamma power, but did significantly increase coupling between gamma and theta (Stoilijkovic et al., 2015). Given the effects of acetylcholine on the phase amplitude coupling between gamma and theta rhythms, we also think that acetylcholine plays a role in phase-amplitude coupling for splines by modulating some of the same neurons to fire specifically at the peaks of theta.

4.6 Future directions and speculations

4.6.1 Low-rheobase neuron contributions

To further understand LR neurons' potential role in spline propagation or generation, it would be good to know the firing rates of LR neurons *in vivo* during different brain states. LR neurons are found across the RSC's long axis, are anatomically positioned to send information from one RSG hemisphere to the other, and neurons only synapse to FS neurons locally (Brennan et al., 2020). It is not yet known which cell types LR neurons synapse to contralaterally, but determining this will also provide clues to LR neurons' shaping of the RSG's oscillations. While rostral anterior-posterior planes of the RSC have the corpus callosum and the two RSC hemispheres anatomically close to each other while the more caudal anterior-posterior planes of RSC are farther apart without the corpus callosum in the same cross-section. This raises the question of how connectivity within the anterior-posterior plane of RSC may cause splines to differ. In our experiments, we kept consistent probe sites for in-vivo electrophysiology. Future experiments may explore what happens with splines in more caudal planes of RSG: whether the cross-hemispheric coherence is as strong when the two RSG hemispheres are physically farther apart, whether splines have the most power in the AP planes where the corpus callosum is thickest, and whether they may be a topographic organization to splines along the long axis of the brain.

4.6.2 Retrosplenial oscillations in the broader circuit

Studying retrosplenial cortex oscillations and their correlates would ideally be in the context of the broader circuit. Since the RSC is an association cortex and one of the most heavily interconnected brain regions, there are many avenues for investigating its circuitry. CA1 neurons have long-range axonal projections to the retrosplenial cortex and have been found to be a distinct class of GABAergic neurons (Yamawaki et al., 2019a). The border of the stratum radiatum and stratum lacunosum-moleculare are anatomically positioned to mediate direct inhibitory communication from dorsal hippocampus to RSG, and they have been shown to do so in channelrhodopsin-assisted circuit mapping (CRACM) experiments in slices. Experiments chemogenetically inhibiting connections from CA1 to RSG increase freezing behavior during the retrieval test of contextual fear conditioning. In contrast, inhibiting connections from anterior thalamic nuclei (ATN) to RSG reduced freezing behavior in the same retrieval test.

The Yamawaki et al. study did not investigate oscillatory dynamics during behavior. It is notable that the GABAergic neurons' long-range axons synapse onto and potently inhibit apical dendrites of excitatory L5 pyramidal neurons in RSG. Performing similar experiments while measuring and manipulating the circuit will shed light on how splines may be altered when inhibiting CA1 versus ATN. Since the effect is strong enough to cause differences in freezing behavior and the CA1-RSG projections are inhibitory while the ATN-RSG projections are excitatory, I would expect the CA1 and the ATN inputs to affect retrosplenial oscillatory dynamics differently at the population level in vivo, as well.

Given that the ATN and CA1 synapse to layer 1 of the RSG and that both of these regions would be involved in navigation to escape to shelter, disrupting the coordination of ATN and CA1 inputs to layer 1 of RSG during escape behavior may impair navigation towards shelter. It is known that the RSC-superior colliculus circuit supports an egocentric representation of shelter direction and that chemogenetically disrupting the superior colliculus's inputs to the RSC decreases the efficiency of shelter direction encoding (Vale et al., 2020), but given the ATN's essential role in head direction encoding and synapses to layer 1a of the RSG where the apical dendrites of LR neurons are (Brennan et al., 2021), that the LR neurons are the most prevalent cell type in L2 and L3 of the RSG, and the relative strength of the splines in the superficial layers of the RSG which are the only known locations of LR neuron cell bodies (Brennan et al., 2020), I hypothesize that inhibiting ATN would change retrosplenial oscillations in the superficial layers. The ATN provides a strong external drive to the retrosplenial cortex (Brennan et al., 2021). As lesions in the rodent ATN cause severe spatial deficits (Aggleton and Nelson, 2015), I also hypothesize that there will be a corresponding behavioral correlate: if the anterodorsal nucleus's neurons are inhibited, the animal would take a longer path in orienting and navigating towards a shelter for escape.

4.6.3 In-vivo experiments with Alzheimer's mouse model

Another future direction is to perform more in-vivo behavioral experiments with 5xFAD mice, which have five different mutations associated with Alzheimer's disease:

APP KM670/671NL (Swedish), APP I716V (Florida), APP V717I (London), PSEN1 M146L (A>C), and PSEN1 L286V (Oakley et al., 2006). 5xFAD mice are impaired in spontaneous alternation in the Y-maze at 4-5 months (Oakley et al., 2006; Devi and Ohno, 2010). These mice are also impaired in navigating the Morris water maze at 6 months (Xiao et al., 2015), in social recognition learning at 9 months (Flanigan et al., 2014), and in motor function at 12 months (O'Leary et al., 2018). 5xFAD mice have a 10% decrease in hippocampal volume by 13 months of age (MacDonald et al., 2014). 5xFAD mice also have impairments in place cell reactivation, with shorter and fewer sharp wave ripples (Prince et al., 2021). It may be insightful to investigate the dynamics of splines and ripples in the retrosplenial cortices of these mice, to compare which of these oscillations is most disrupted with the progression of Alzheimer's disease. Given that both the retrosplenial cortex and the hippocampus are affected early in Alzheimer's disease, I would expect that like how ripples are fewer and shorter in hippocampus, both ripples and splines are fewer and shorter in the RSC of these transgenic mice. Identifying oscillatory biomarkers for Alzheimer's disease progression may help to develop interventions and assess their effectiveness.

4.6.4 Eye movement

Splines occur most strongly during REM sleep but also during awake movement, two states which involve eye movement. It is possible that splines may be modulated by eye movement. In awake behavior, the optic flow component could be isolated from eye movement with a virtual reality environment or using a projector. The eye movement

component may be assessed in the future if we add an eye tracking device to our setup. If splines could occur in RSG during awake head fixation in the absence of running while the visual scene is changing, if they increased in amplitude with faster and more dynamic changes to the visual scene, and if they were not significantly different from splines during passive motion at the same speeds, this would serve as a line of evidence that visual inputs contribute to the generation of splines. As high-frequency oscillations of 110-160 Hz have been found in various other cortical regions (González et al., 2020; Sirota et al., 2008; Scheffzük et al., 2011; Tort et al., 2013), characterizing the microcircuitry that underpins these regions' ability to generate high-frequency oscillations may give greater insight into the functions of these high-frequency oscillations and how they may differ in regions with different cell types.

4.6.5 Passive motion experiments

There are several considerations to keep in mind while designing experiments to study passive motion in very controlled ways. Noise artifacts may occur during passive motion of the mouse on the spherical treadmill, and these noises change according to the speed that the mouse is passively pushed. This would likely lead to processing of sounds by the auditory cortex, something that may go unnoticed if video information is captured without measuring audio data during the recording. The visual environments for freely moving behavioral paradigms and for the head-fixed paradigms could be made more similarly: as uniform and featureless as possible via use of a black curtain, true darkness, an infrared camera, and better sensors to monitor head position and

movement. The technical challenge in using an infrared sensor is that it is challenging to monitor head tilts and movements. Future experiments will be designed to extract and triangulate motion via gyroscope and accelerometer with high precision, allowing us to perform well-controlled experiments manipulating vestibular inputs. Learning about spline dynamics in the switch from active modes of motion to passive, virtual modes of motion will be another direction for probing the oscillations that underpin navigation abilities.

4.6.6 Exploration of microcircuitry in spline dynamics using genetic tools

If splines have anti-phase cross-hemispheric coordination across the hemispheres, can splines can exist in a single hemisphere without existing in the contralateral hemisphere? If so, yet another question arises: exactly what about the contralateral hemisphere facilitates splines, and to what extent? This question can be answered in part by using genetic tools to manipulate different cells in the circuit. I would expect that exciting or silencing fast-spiking inhibitory neurons would change gamma rhythms and strongly affect splines, but it is also possible that low-rheobase neurons, which synapse to neurons in the contralateral hemisphere, are key to the cross-hemispheric coordination mechanism of this high-frequency oscillation. As both splines and gamma are modes of cross-hemispheric communications, I think both of these brain rhythms have some coordination via the low-rheobase neurons that may be communicating signals across the hemispheres.

Using optogenetics in a closed-loop system to activate or inhibit different types of neurons in the retrosplenial cortex upon detecting splines the first few spline-containing theta cycles may allow us to determine what happens with splines during REM sleep versus during awake active running would be helpful to see if they drive a behavioral correlate.

Higher excitatory external input, as through the thalamus and the medial septum/diagonal band of Broca during high-activity REM states or when the animal runs faster, may synchronize inhibitory neurons, leading to higher spline frequency and power. LR neurons comprise 61% of the neurons in L2 and L3 of the RSG (Brennan et al., 2020), which are also the layers where splines (Ghosh et al., 2021), gamma, and ripples are the strongest (Nitzan et al., 2020). Further experiments are needed to create a more complete model of how splines are generated and elucidate what role, if any, LR neurons may play in spline generation. Currently, there is no known genetic or molecular signature that is specific only to LR neurons, and finding such signatures is another future direction for retrosplenial cortex research. We cannot yet precisely target LR neurons for optogenetics or chemogenetics in-vivo, but since we know they are excitatory (Brennan et al., 2020), we can target them along with RS neurons or along with all neurons. Selectively silencing different cell types or groups of cell types would shed light on their specific contributions to spline initiation, propagation, and function during both active behaviors and during sleep.

What we have described here about splines is just the tip of the iceberg. There are still numerous questions on the tips of our tongues, and many future directions to navigate in further characterizing this high-frequency oscillation

BIBLIOGRAPHY

1.   Aggleton JP, Nelson AJ. 2015. Why do lesions in the rodent anterior thalamic nuclei cause such severe spatial deficits? *Neurosci Biobehav Rev.* 54:131-44. doi:10.1016/j.neubiorev.2014.08.013

2.   Ahmed OJ, Mehta MR. 2009. The hippocampal rate code: anatomy, physiology and theory. *Trends Neurosci.* 32(6):329–338. doi:10.1016/j.tins.2009.01.009

3.   Ahmed OJ, Mehta MR. 2012. Running speed alters the frequency of hippocampal gamma oscillations. *J. Neurosci.* 32(21):7373–7383. doi:10.1523/JNEUROSCI.5110-11.2012

4.   Alexander AS, Carstensen LC, Hinman JR, Raudies F, Chapman GW, Hasselmo ME. 2020a. Egocentric boundary vector tuning of the retrosplenial cortex. *Sci. Adv.* 6(8):eaaz2322. doi:10.1126/sciadv.aaz2322

5.   Alexander AS, Robinson JC, Dannenberg H, Kinsky NR, Levy SJ, Mau W, Chapman GW, Sullivan DW, Hasselmo ME. 2020b. *Brain Neuroscience Adv.* 4:2398212820972871. doi:10.1177/2398212820972871

6.   Alexander AS, Rangel LM, Tingley D, Nitz DA. 2018. Neurophysiological signatures of temporal coordination between retrosplenial cortex and the hippocampal formation. *Behav. Neurosci.* 132:453–468. doi:10.1037/bne0000254

7.   Amaral DG, Witter MP. 1989. The three-dimensional organization of the hippocampal formation: a review of anatomical data. *Neuroscience* 31(3):571-91. doi:10.1016/0306-4522(89)90424-7

8.   Amemiya S, Redish AD. 2018. Hippocampal Theta-Gamma Coupling Reflects State-Dependent Information Processing in Decision Making. *Cell Rep.* 2(12):3328-3338. doi:10.1016/j.celrep.2018.02.091

9.   Angelaki DE, Gu Y, DeAngelis GC. 2009. Multisensory integration: psychophysics, neurophysiology, and computation. *Curr Opin Neurobiol.* 19(4):452-8. doi:10.1016/j.conb.2009.06.008

10. Aronov D, Tank DW. 2014. Engagement of the neural circuits underlying 2D spatial navigation in a rodent virtual reality system. *Neuron* 84(2): 442-56. doi:10.1016/j.neuron.2014.08.042

11. Aserinsky E, Kleitman N. 1953. Regularly occuring periods of eye motility, and concomitant phenomena, during sleep. *Science* 118:273-274. doi:10.1126/science.118.3062.273

12. Athanasiadou D, Jiang W, Reznikov N, Rodríguez-Navarro AB, Kröger R, Bilton M, González-Segura A, Hu Y, Nelea V, McKee MD. 2020. Nanostructure of mouse otoconia. *J Struct Biol.* 210(2):107489. doi:10.1016/j.jsb.2020.107489

13. Bähner F, Weiss EK, Birke G, Maier N, Schmitz D, Rudolph U, Frotscher M, Traub RD, Both M, Draguhn A. 2011. Cellular correlate of assembly formation in oscillating hippocampal networks in vitro. *Proc Natl Acad Sci U S A* 108(35):E607-16. doi:10.1073/pnas.1103546108

14. Barlow JS. 1964. Inertial navigation as a basis for animal navigation. *J Theor Biol.* 6(1):76–117. doi:10.1016/0022-5193(64)90067-0

15. Barry C, Lever C, Hayman R, Hartley T, Burton S, O'Keefe J, Jeffery K, Burgess N. 2006. The boundary vector cell model of place cell firing and spatial memory. *Rev Neurosci.* 17(1-2):71-97. doi:10.1515/revneuro.2006.17.1-2.71

16. Benchenane K, Peyrache A, Khamassi M, Tierney PL, Gioanni Y, Battaglia FP, Wiener SI. 2010. Coherent theta oscillations and reorganization of spike timing in the hippocampal- prefrontal network upon learning. *Neuron* 66(6):921-36. doi:10.1016/j.neuron.2010.05.013

17. Berens P. 2009. CircStat : A MATLAB Toolbox for Circular Statistics. *J. Stat. Softw. 31*, 1–21

18. Bigl V, Woolf NJ, Butcher LL. 1982. Cholinergic projections from the basal forebrain to frontal, parietal, temporal, occipital, and cingulate cortices: a combined fluorescent tracer and acetylcholinesterase analysis. *Brain Res Bull.* 8(6):727-49. doi:10.1016/0361-9230(82)90101-0

19. Bittner KC, Grienberger C, Vaidya SP, Milstein AD, Macklin JJ, Suh J, Tonegaw S, Magee JC. 2015. Conjunctive input processing drives feature selectivity in hippocampal CA1 neurons. *Nat Neurosci.* 18(8):1133-42. doi:10.1038/nn.4062

20. Bland NS, Mattingley JB, Sale MV. (2020). Gamma coherence mediates interhemispheric integration during multiple object tracking. *J. Neurophysiol.* 123: 1630–1644. doi:10.1152/jn.00755.2019

21. Blytt KM, Bjorvatn B, Husebo B, Flo E. 2017. Clinically significant discrepancies between sleep problems assessed by standard clinical tools and actigraphy. *BMC Geriatr.* 17(1):253. doi:10.1186/s12877-017-0653-7

22. Börgers C, Kopell N. 2003. Synchronization in networks of excitatory and inhibitory neurons with sparse, random connectivity. *Neural Comput.* 15(3):509-38. doi:10.1162/089976603321192059

23. Börgers C, Kopell N. 2005. Effects of noisy drive on rhythms in networks of excitatory and inhibitory neurons. *Neural Comput.* 17(3):557-608. doi:10.1162/0899766053019908

24. Börgers C. 2017. The PING Model of Gamma Rhythms. In: An Introduction to Modeling Neuronal Dynamics. Texts in Applied Mathematics. *Springer, Cham.* 66:255-267. doi:10.1007/978-3-319-51171-9_30

25. Bragin A, Jandó G, Nádasdy Z, Hetke J, Wise K, Buzsáki G. 1995. Gamma (40-100 Hz) oscillation in the hippocampus of the behaving rat. *J. Neurosci.* 15:47–60. doi:10.1523/JNEUROSCI.15-01-00047.1995

26. Brandon MP, Bogaard AR, Libby CP, Connerney MA, Gupta K, Hasselmo ME. 2011. Reduction of theta rhythm dissociates grid cell spatial periodicity from directional tuning. *Science* 332(6029):595-9. doi:10.1126/science.1201652

27. Brandt T, Schautzer F, Hamilton DA, Brüning R, Markowitsch HJ, Kalla R, Darlington C, Smith P, Strupp M. 2005. Vestibular loss causes hippocampal atrophy and impaired spatial memory in humans. *Brain: a journal of neurology* 128(Pt 11):2732-41. doi:10.1093/brain/awh617

28. Brennan EKW, Jedrasiak-Cape I, Kailasa S, Rice SP, Sudhakar SK, Ahmed OJ. 2021. Thalamus and claustrum control parallel layer 1 circuits in retrosplenial cortex. *Elife* 10:e62207. doi:10.7554/eLife.62207

29. Brennan EKW, Sudhakar SK, Jedrasiak-Cape I, John TT, Ahmed OJ. 2020. Hyperexcitable Neurons Enable Precise and Persistent Information Encoding in the Superficial Retrosplenial Cortex. *Cell Reports* 30:1598-1612.e8. doi:10.1016/j.celrep.2019.12.09

30. Burgess N, Becker S, King JA, O'Keefe J. 2001. Memory for events and their spatial context: models and experiments. *Philos Trans R Soc Lond B Biol Sci.* 356, 1493–1503. doi:10.1098/rstb.2001.0948

31. Butler JS, Smith ST, Campos JL, Heinrich H. Bülthoff HH. 2010. Bayesian integration of visual and vestibular signals for heading. *Journal of Vision* 10(11):23. doi:https://doi.org/10.1167/10.11.23

32. Buzsáki G. 1989. Two-stage model of memory trace formation: a role for "noisy" brain states. *Neuroscience* 31:3, 551-570. doi:10.1016/0306-4522(89)90423-5

33. Buzsáki G. 2004. Large-scale recording of neuronal ensembles. *Nat. Neurosci.* 7:446-451. doi:10.1038/nn1233

34. Buzsáki G. 2011. Hippocampus. *Scholarpedia* 6(1):1468. doi:10.4249/scholarpedia.1468

35. Buzsáki G. 2015. Hippocampal Sharp Wave-Ripple: A Cognitive Biomarker for Episodic Memory and Planning. *Hippocampus* 25:1073-1188. doi:10.1002/hipo.22488

36. Buzsáki G, Moser EI. 2013. Memory, navigation and theta rhythm in the hippocampal- entorhinal system. *Nat. Neurosci.* 16(2):130. doi:10.1038/nn.3304

37. Buzsáki G, Watson BO. 2012. Brain rhythms and neural syntax: implications for efficient coding of cognitive content and neuropsychiatric disease. *Dialogues in Clinical Neuroscience* 14(4):345-367. doi:10.31887/DCNS.2012.14.4/gbuzsaki

38. Byrne P, Becker S, Burgess N. 2007. Remembering the past and imagining the future: a neural model of spatial memory and imagery. *Psychol Rev.* 114(2):340-75. doi:10.1037/0033-295X.114.2.340

39. Cardin JA, Carlén M, Meletis K, Knoblich U, Zhang F, Deisseroth K, Tsai LH, Moore CI. 2009. Driving fast-spiking cells induces gamma rhythm and controls sensory responses. *Nature* 459(7247):663-7. doi:10.1038/nature08002

40. Chen Z, Resnik E, McFarland JM, Sakmann B, Mehta MR. 2011. Speed controls the amplitude and timing of the hippocampal gamma rhythm. *PLoS One* 6(6):e21408. doi:10.1371/journal.pone.0021408

41. Cho KKA, Davidson TJ, Bouvier G, Marshall JD, Schnitzer MJ, Sohal VS. 2020. Cross-hemispheric gamma synchrony between prefrontal parvalbumin interneurons supports behavioral adaptation during rule shift learning. *Nat Neurosci.* 23(7):892-902. doi:10.1038/s41593-020-0647-1

42. Cho KK, Hoch R, Lee AT, Patel T, Rubenstein JL, Sohal VS. 2015. Gamma Rhythms Link Prefrontal Interneuron Dysfunction with Cognitive Inflexibility in *Dlx5/6*[+/-] Mice. *Neuron* 85(6):1332-1343. doi:10.1016/j.neuron.2015.02.019

43. Cho J, Sharp, PE. 2001. Head direction, place, and movement correlates for cells in the rat retrosplenial cortex. *Behav Neurosci.* 115(1):3-25. doi:10.1037/0735-7044.115.1.3

44. Clark BJ, Bassett JP, Wang SS, Taube JS. 2010. Impaired Head Direction Cell Representation in the Anterodorsal Thalamus after Lesions of the Retrosplenial Cortex. *J. Neurosci.* 30(15):528-5302. doi:10.1523/JNEUROSCI.3380-09.2010

45. Colgin LL. 2013. Mechanisms and functions of theta rhythms. *Annu Rev Neurosci.* 36:295-312. doi:10.1146/annurev-neuro-062012-170330

46. Colgin LL, Denninger T, Fyhn M, Hafting T, Bonnevie T, Jensen O, Moser MB, Moser EI. 2009. Frequency of gamma oscillations routes flow of information in the hippocampus. *Nature* 462(7271):353-7. doi:10.1038/nature08573

47. Connors BW, Gutnick MJ. 1990. Intrinsic firing patterns of diverse neocortical neurons. *Trends Neurosci.* 13(3):99-104. doi:10.1016/0166-2236(90)90185-d

48. Corradi F, Zambrano D, Raglianti M, Passetti G, Laschi C, Indiveri G. 2014. Towards a neuromorphic vestibular system. *IEEE Trans Biomed Circuits Syst.* 8(5):669-80. doi:10.1109/TBCAS.2014.2358493

49. Csicsvari J, Jamieson B, Wise KD, Buzsáki G. 2003. Mechanisms of gamma oscillations in the hippocampus of the behaving rat. *Neuron* 37(2):311-22. doi:10.1016/s0896-6273(02)01169-8

50. Cullen KE. 2014. The neural encoding of self-generated and externally applied movement: implications for the perception of self-motion and spatial memory. *Front Integr Neurosci.* 7:108. doi:10.3389/fnint.2013.00108

51. Cullen KE, Taube JS. 2017. Our Sense of Direction: Progress, Controversies, and Challenges. *Nature Neuroscience* 20(11):1465-1473. doi:10.1038/nn.465

52. Dannenberg H, Pabst M, Braganza O, Schoch S, Niediek J, Bayraktar M, Mormann F, Beck H. 2015. Synergy of direct and indirect cholinergic septo-hippocampal pathways coordinates firing in hippocampal networks. *J Neurosci.* 35(22):8394-410. doi:10.1523/JNEUROSCI.4460-14.2015

53. Darwin C. 1873. Origin of Certain Instincts. *Nature* 417-418. doi:10.1038/007417a0

54. Devi L, Ohno M. 2010. Phospho-eIF2α level is important for determining abilities of BACE1 reduction to rescue cholinergic neurodegeneration and memory defects in 5XFAD mice. *PLoS One* 5(9):e12974. doi:10.1371/journal.pone.0012974

55. de Winkel KN, Katliar M, Bülthoff HH. 2017. Causal Inference in Multisensory Heading Estimation. *PLoS One* 12(1):e0169676. doi:10.1371/journal.pone.0169676

56. Dolorfo CL, Amaral DG. 1998. Entorhinal cortex of the rat: topographic organization of the cells of origin of the perforant path projection to the dentate gyrus. *J Comp Neurol.* 398(1):25-48

57. Domesick VB. 1969. Projections from the cingulate cortex in the rat. *Brain Res.* 12(2):296–320. doi:10.1016/0006-8993(69)90002-x

58. Dragoi G, Buzsáki G. 2006. Temporal encoding of place sequences by hippocampal cell assemblies. *Neuron* 50(1):145–157. doi:10.1016/j.neuron.2006.02.023

59. Engel AK, Singer W. 2001. Temporal binding and the neural correlates of sensory awareness. *Trends Cogn. Sci. (Regul. Ed.)* 5(1):16–25. doi:10.1016/s1364-6613(00)01568-0

60. Epstein RA. 2008. Parahippocampal and retrosplenial contributions to human spatial navigation. *Trends Cogn. Sci. 12*, 388–396. doi:10.1016/j.tics.2008.07.004

61. Everson CA. 1995. Functional consequences of sustained sleep deprivation in the rat. *Behav Brain Res.* 69(1-2):43-54. doi:10.1016/0166-4328(95)00009-i

62. Fell J, Klaver P, Lehnertz K, Grunwald T, Schaller C, Elger CE, Fernández G. 2001. Human memory formation is accompanied by rhinal-hippocampal coupling and decoupling. *Nat Neurosci.* 4(12):1259-64. doi:10.1038/nn759

63. Ferguson MA, Lim C, Cooke D, Darby RR, Wu O, Rost NS, Corbetta M, Grafman J, Fox MD. 2019. A human memory circuit derived from brain lesions causing amnesia. *Nature Commun.* 10(1):3497. doi:10.1038/s41467-019-11353-z

64. Fernández-Ruiz A, Oliva A, Fermino de Oliveira E, Rocha-Almeida F, Tingley D, Buzsáki G. 2019. Long-duration hippocampal sharp wave ripples improve memory. *Science* 364(6445):1082-1086. doi:10.1126/science.aax0758

65. Finkelstein A, Ulanovsky N, Tsodyks M, Aljadeff J. 2018. Optimal dynamic coding by mixed-dimensionality neurons in the head-direction system of bats. *Nat Commun.* 9(1):3590. doi:10.1038/s41467-018-05562-1

66. Fitzgerald PJ, Watson BO. 2018. Gamma oscillations as a biomarker for major depression: an emerging topic. Transl Psychiatry. 8(1):177. doi:10.1038/s41398-018-0239-y

67. Flanigan TJ, Xue Y, Kishan Rao S, Dhanushkodi A, McDonald MP. 2014. Abnormal vibrissa-related behavior and loss of barrel field inhibitory neurons in 5xFAD transgenics. *Genes Brain Behav.* doi:10.1111/gbb.12133

68. Fuhs MC, Touretzky DS. 2006. A spin glass model of path integration in rat medial enorhinal cortex. *J Neurosci.* 26(16):4266-4276. doi:10.1523/JNEUROSCI.4353-05.200

69. Fyhn M, Molden S, Witter MP, Moser EI, Moser MB. 2004. Spatial representation in the entorhinal cortex. *Science* 305(5688):1258-64. doi:10.1126/science.1099901

70. Gerlei K, Passlack J, Hawes I, Vandrey B, Stevens H, Papastathopoulos I, Nolan MF. 2020. Grid cells are modulated by local head direction. *Nat Commun* 11(1):4228. doi:10.1038/s41467-020-17500-1

71. Ghosh M*, Yang F*, Rice SP*, Hetrick V, Lorenzo Gonzalez A, Siu D, Brennan EKW, John TT, Ahrens AM, Ahmed OJ. 2021. Running speed controls two distinct modes of rapid interhemispheric communication. Submitted.

72. Giocomo LM, Moser MB, Moser EI. 2011. Computational models of grid cells. *Neuron* 71(4):589-603. doi:10.1016/j.neuron.2011.07.023

73. González J, Cavelli M, Mondino A, Rubido N, Bl Tort A, Torterolo P. 2020. Communication Through Coherence by Means of Cross-frequency Coupling. *Neuroscience* 449:157–164. doi:10.1016/j.neuroscience.2020.09.019

74. Goodman MS, Kumar S, Zomorrodi R, Ghazala Z, Cheam ASM, Barr MS, Daskalakis ZJ, Blumberger DM, Fischer C, Flint A, Mah L, Herrmann N, Bowie CR, Mulsant BH, Rajji TK. 2018. Theta-Gamma Coupling and Working Memory in Alzheimer's Dementia and Mild Cognitive Impairment. *Front Aging Neurosci.* 10:101. doi:10.3389/fnagi.2018.00101

75. Gray CM, König P, Engel AK, Singer W. 1989. Oscillatory responses in cat visual cortex exhibit inter-columnar synchronization which reflects global stimulus properties. *Nature 338*, 334–337. doi:10.1038/338334a0

76. Guo W, Liu F, Dai Y, Jiang M, Zhang J, Yu L, Long L, Chen H, Gao Q, Xiao C. 2013. Decreased interhemispheric resting-state functional connectivity in first-episode, drug-naive major depressive disorder. *Prog Neuropsychopharmacol Biol Psychiatry* 41:24-9. doi:10.1016/j.pnpbp.2012.11.003

77. Hafting T, Fyhn M, Molden S, Moser MB, Moser EI. 2005. Microstructure of a spatial map in the entorhinal cortex. *Nature* 436:801–806. doi:10.1038/nature0372

78. Hargreaves EL, Rao G, Lee I, Knierim JJ. 2005. Major dissociation between medial and lateral entorhinal input to dorsal hippocampus. *Science* 308(5729):1792-4. doi:10.1126/science.1110449

79. Harvey RE, Rutan SA, Willey GR, Siegel JJ, Clark BJ, Yoder RM. 2018. Linear Self-Motion Cues Support the Spatial Distribution and Stability of Hippocampal Place Cells. *Curr Biol.* 28(11):1803-1810.e5. doi:10.1016/j.cub.2018.04.034

80. Hasenstaub A, Shu Y, Haider B, Kraushaar U, Duque A, McCormick DA. 2005. Inhibitory postsynaptic potentials carry synchronized frequency information in active cortical networks. *Neuron* 47(3):423-35. doi:10.1016/j.neuron.2005.06.016

81. Headley DB, Weinberger NM. 2011. Gamma-Band Activation Predicts Both Associative Memory and Cortical Plasticity. *J Neurosci.* 31(36):12748-12758. doi:10.1523/JNEUROSCI.2528-11.2011

82. Headley DB, Weinberger NM. 2013. Fear Conditioning Enhances Gamma Oscillations and Their Entrainment of Neurons Representing the Conditioned Stimulus. *J Neurosci.* 33(13):5705-5717. doi:10.1523/JNEUROSCI.4915-12.2013

83. Hennawy M, Sabovich S, Liu CS, Herrmann N, Lanctôt KL. 2019. Sleep and Attention in Alzheimer's Disease. *Yale J Biol Med* 92(1):53-61.

84. Highstein SM, Holstein GR. 2006. The anatomy of the vestibular nuclei. *Prog Brain Res.* 151:157-203. doi:10.1016/S0079-6123(05)51006-9

85. Horii A, Russell NA, Smith PF, Darlington CL, Bilkey DK. 2004. Vestibular influences on CA1 neurons in the rat hippocampus: an electrophysiological study in vivo. *Exp Brain Res.* 155(2):245-50. doi:10.1007/s00221-003-1725-9

86. Horii A, Takeda N, Mochizuki T, Okakura-Mochizuki K, Yamamoto Y, Yamatodani A. 1994. Effects of vestibular stimulation on acetylcholine release from rat hippocampus: an in vivo microdialysis study. *J Neurophysiol.* 72(2):605-11. doi:10.1152/jn.1994.72.2.605

87. Howe WM, Gritton HJ, Lusk NA, Roberts EA, Hetrick VL, Berke JD, Sarter M. 2017. Acetylcholine Release in Prefrontal Cortex Promotes Gamma Oscillations and Theta-Gamma Coupling during Cue Detection. *J Neurosci.* 37(12):3215-3230. doi:10.1523/JNEUROSCI.2737-16.2017

88. Hwaun E, Colgin LL. 2019. CA3 place cells that represent a novel waking experience are preferentially reactivated during sharp wave-ripples in subsequent sleep. *Hippocampus* 29(10):921-938. doi:10.1002/hipo.23090

89. Jacobs J, Kahana MJ, Ekstrom AD, Fried I. 2007. Brain oscillations control timing of single-neuron activity in humans. *J Neurosci.* 27(14):3839-44. doi:10.1523/JNEUROSCI.4636-06.2007

90. Jarosiewicz B, McNaughton BL, Skaggs WE. 2002. Hippocampal population activity during the small-amplitude irregular activity state in the rat. *J Neurosci.* 22(4):1373-84. doi:10.1523/JNEUROSCI.22-04-01373.2002

91. Jensen O, Kaiser J, Lachaux JP. 2007. Human gamma-frequency oscillations associated with attention and memory. *Trends Neurosci.* (7):317-24. doi:10.1016/j.tins.2007.05.001

92. Johnson LG, Rouse RC, Wright CG, Henry PJ, Hawkins JE Jr. 1982. Pathology of neuroepithelial suprastructures of the human inner ear. *Am J Otolaryngol.* 3(2):77-90. doi:10.1016/s0196-0709(82)80037-9

93. Jutras MJ, Fries P, Buffalo EA. 2009. Gamma-band synchronization in the macaque hippocampus and memory formation. *J Neurosci.* 29(40):12521-31. doi:10.1523/JNEUROSCI.0640-09.2009

94. Kemere C, Carr MF, Karlsson MP, Frank LM. 2013. Rapid and continuous modulation of hippocampal network state during exploration of new places. *PLoS One* 8(9):e73114. doi:10.1371/journal.pone.0073114

95. Kim DH, Kim HA, Han YS, Jeon WK, Han JS. 2020. Recognition memory impairments and amyloid-beta deposition of the retrosplenial cortex at the early stage of 5XFAD mice. *Physiol Behav.* 222:112891. doi:10.1016/j.physbeh.2020.112891

96. Kinnavane L, Vann SD, Nelson AJD, O'Mara SM, Aggleton JP. 2018. Collateral Projections Innervate the Mammillary Bodies and Retrosplenial Cortex: A New Category of Hippocampal Cells. *eNeuro* 5(1):ENEURO.0383-17.2018. doi:10.1523/ENEURO.0383-17.2018

97. Klausberger T, Magill PJ, Márton LF, Roberts JD, Cobden PM, Buzsáki G, Somogyi P. 2003. Brain-state- and cell-type-specific firing of hippocampal interneurons in vivo. *Nature* 421(6925):844-8. doi:10.1038/nature01374

98. Koenig J, Linder AN, Leutgeb JK, Leutgeb S. 2011. The spatial periodicity of grid cells is not sustained during reduced theta oscillations. *Science* 332:592–95

99. Koike BDV, Farias KS, Billwiller F, Almeida-Filho D, Libourel PA, Tiran-Cappello A, Parmentier R, Blanco W, Ribeiro S, Luppi PH, Queiroz CM. 2017. Electrophysiological Evidence That the Retrosplenial Cortex Displays a Strong and Specific Activation Phased with Hippocampal Theta during Paradoxical (REM) Sleep. *J Neurosci.* 37(33):8003-8013. doi:10.1523/JNEUROSCI.0026-17.2017

100. Kremmyda O, Hüfner K, Flanagin VL, Hamilton DA, Linn J, Strupp M, Jahn K, Brandt T. 2016. Beyond Dizziness: Virtual Navigation, Spatial Anxiety and Hippocampal Volume in Bilateral Vestibulopathy. *Front Hum Neurosci.* 10:139. doi:10.3389/fnhum.2016.00139

101. Kropff E, Carmichael JE, Moser MB, Moser EI. 2015. Speed cells in the medial entorhinal cortex. *Nature* 523(7561):419-24. doi:10.1038/nature1462

102. Kubie JL, Fenton AA. 2012. Linear look-ahead in conjunctive cells: An entorhinal mechanism for vector-based navigation. *Frontiers in Neural Circuits* 20:1-15. doi:10.3389/fncir.2012.0002

103. Lakmache Y, Lassonde M, Gauthier S, Frigon JY, Lepore F. 1998. Interhemispheric disconnection syndrome in Alzheimer's disease. *Proc Natl Acad Sci U S A* 95(15):9042-6. doi:10.1073/pnas.95.15.9042

104. Le Bon O. 2020. Relationships between REM and NREM in the NREM-REM sleep cycle: a review on competing concepts. *Sleep Med.* 70:6-16. doi:10.1016/j.sleep.2020.02.004

105. Lee S, Jones SR. 2013. Distinguishing mechanisms of gamma frequency oscillations in human current source signals using a computational model of a laminar neocortical network. *Front Hum Neurosci.* 7:869. doi:10.3389/fnhum.2013.00869

106. Leutgeb JK, Leutgeb S, Moser MB, Moser EI. 2007. Pattern separation in the dentate gyrus and CA3 of the hippocampus. *Science* 315(5814):961-6. doi:10.1126/science.1135801

107. Lisman JE, Jensen O. 2013. The θ-γ neural code. *Neuron* 77(6):1002-16. doi: 10.1016/j.neuron.2013.03.007

108. Louie K, Wilson, MA. 2001. Temporally structured replay of awake hippocampal ensemble activity during rapid eye movement sleep. *Neuron* 29(1):145-56. doi:10.1016/s0896-6273(01)00186-6

109. MacDonald IR, DeBay DR, Reid GA, O'Leary TP, Jollymore CT, Mawko G, Burrell S, Martin E, Bowen CV, Brown RE, Darvesh S. 2014. Early detection of cerebral glucose uptake changes in the 5XFAD mouse. *Curr Alzheimer Res.* 11(5):450-60. doi:10.2174/1567205011666140505111354

110. Maguire E. 2001. The retrosplenial contribution to human navigation: A review of lesion and neuroimaging findings. Scand. *J. Psychol.* 42:225–238. doi:10.1111/1467-9450.00233

111. Martorell AJ, Paulson AL, Suk HJ, Abdurrob F, Drummond GT, Guan W, Young JZ, Kim DN, Kritskiy O, Barker SJ, Mangena V, Prince SM, Brown EN, Chung K, Boyden ES, Singer AC, Tsai LH. 2019. Multi-sensory Gamma Stimulation Ameliorates Alzheimer's-Associated Pathology and Improves Cognition. *Cell* 177(2):256-271.e22. doi:10.1016/j.cell.2019.02.014

112. Mathalon DH, Sohal VS. 2015. Neural Oscillations and Synchrony in Brain Dysfunction and Neuropsychiatric Disorders: It's About Time. *JAMA Psychiatry* 72(8):840-4. doi:10.1001/jamapsychiatry.2015.0483

113. Maurer AP, Burke SN, Lipa P, Skaggs WE, Barnes CA. 2012. Greater running speeds result in altered hippocampal phase sequence dynamics. *Hippocampus* 22(4):737-47. doi:10.1002/hipo.20936

114. McNaughton BL, Battaglia FP, Jensen O, Moser EI, Moser MB. 2006. Path integration and the neural basis of the 'cognitive map'. *Nat Rev Neurosci.* 7(8):663-78. doi:10.1038/nrn1932

115. Meddis R. 1975. On the function of sleep. *Anim Behav.* 23(3):676-91. doi:10.1016/0003-3472(75)90144-x

116. Minoshima S, Giordani B, Berent S, Frey KA, Foster NL, Kuhl DE. 1997. Metabolic reduction in the posterior cingulate cortex in very early Alzheimer's disease. *Ann Neurol.* 42(1):85-94. doi:10.1002/ana.410420114

117. Mitchell SJ, Rawlins JN, Steward O, Olton DS. 1982. Medial septal area lesions disrupt theta rhythm and cholinergic staining in medial entorhinal cortex and produce impaired radial arm maze behavior in rats. *J Neurosci.* 2(3):292-302. doi:10.1523/JNEUROSCI.02-03-00292.1982

118. Mizumori SJ, Perez GM, Alvarado MC, Barnes CA, McNaughton BL. 1990. Reversible inactivation of the medial septum differentially affects two forms of learning in rats. *Brain Res.* 528(1):12-20. doi:10.1016/0006-8993(90)90188-h

119. Monacelli AM, Cushman LA, Kavcic V, Duffy CJ. 2003. Spatial disorientation in Alzheimer's disease: the remembrance of things passed. *Neurology* 61(11):1491-7. doi:10.1212/wnl.61.11.149

120. Montgomery SM, Buzsáki G. 2007. Gamma oscillations dynamically couple hippocampal CA3 and CA1 regions during memory task performance. *Proc Natl Acad Sci U S A* 104(36):14495-500. doi:10.1073/pnas.0701826104

121. Montgomery SM, Sirota A, Buzsáki G. 2008. Theta and gamma coordination of hippocampal networks during waking and rapid eye movement sleep. *J Neurosci.* 28(26):6731-41. doi:10.1523/JNEUROSCI.1227-08.2008

122. Moran M, Lynch CA, Walsh C, Coen R, Coakley D, Lawlor B. 2005. Sleep disturbance in mild to moderate Alzheimer's disease. *Sleep Med.* 6(4):347-52. doi:10.1016/j.sleep.2004

123. Moser EI, Kropff E, Moser MB. 2008. Place cells, grid cells, and the brain's spatial representation system. *Annu Rev Neurosci* 31:69-89. doi:10.1146/annurev.neuro.31.061307.090723

124. Most EI, Aboudan S, Scheltens P, Van Someren EJ. 2012. Discrepancy between subjective and objective sleep disturbances in early- and moderate-stage

Alzheimer disease. *Am J Geriatr Psychiatry* 20(6):460-7. doi:10.1097/JGP.0b013e318252e3ff

125. Murthy VN, Fetz EE. 1992. Coherent 25- to 35-Hz oscillations in the sensorimotor cortex of awake behaving monkeys. *Proc Natl Acad Sci U S A* 89(12):5670-4. doi:10.1073/pnas.89.12.5670

126. Murthy VN, Fetz EE. 1996. Oscillatory activity in sensorimotor cortex of awake monkeys: synchronization of local field potentials and relation to behavior. *J Neurophysiol.* 76(6):3949-67. doi:10.1152/jn.1996.76.6.3949

127. Murakami K, Ishikawa Y, Sato F. 2013. Localization of α7 nicotinic acetylcholine receptor immunoreactivity on GABAergic interneurons in layers I-III of the rat retrosplenial granular cortex. *Neuroscience* 252:443-59. doi:10.1016/j.neuroscience.2013.08.024

128. Nestor PJ, Fryer TD, Ikeda M, Hodges JR. 2003. Retrosplenial cortex (BA 29/30) hypometabolism in mild cognitive impairment (prodromal Alzheimer's disease). *Eur J Neurosci.* 18(9):2663-7. doi:10.1046/j.1460-9568.2003.0299

129. Neustadter E, Mathiak K, Turetsky BI. 2016. Chapter 13- EEG and MEG Probes of Schizophrenia Pathophysiology. *Academic Press* 213-236

130. Newman EL, Gillet SN, Climer JR, Hasselmo ME. 2013. Cholinergic blockade reduces theta-gamma phase amplitude coupling and speed modulation of theta frequency consistent with behavioral effects on encoding. *J Neurosci.* 33(50):19635-46. doi:10.1523/JNEUROSCI.2586-13.2013

131. Nitzan N, McKenzie S, Beed P, English DF, Oldani S, Tukker JJ, Buzsáki G, Schmitz D. 2020. Propagation of hippocampal ripples to the neocortex by way of a subiculum-retrosplenial pathway. *Nat Commun.* 11(1):1947. doi:10.1038/s41467-020-15787-8

132. Oakley H, Cole SL, Logan S, Maus E, Shao P, Craft J, Guillozet-Bongaarts A, Ohno M, Disterhoft J, Van Eldik L, Berry R, Vassar R. 2006. Intraneuronal beta-amyloid aggregates, neurodegeneration, and neuron loss in transgenic mice with five familial Alzheimer's disease mutations: potential factors in amyloid plaque formation. *J Neurosci.* 26(40):10129-40. doi:10.1523/JNEUROSCI.1202-06.2006

133. Odagiri S, Meguro R, Asano Y, Tani T, Ichinohe N. 2011. Single axon branching analysis in rat thalamocortical projection from the anteroventral thalamus to the granular retrosplenial cortex. *Front Neuroanat.* 5:63. doi:10.3389/fnana.2011.00063

134. O'Keefe J. 1976. Place units in the hippocampus of the freely moving rat. *Exp Neurol.* 51(1):78-109. doi:10.1016/0014-4886(76)90055-8

135. O'Keefe J. 1979. A review of the hippocampal place cells. *Prog Neurobiol.* 13(4):419-39. doi:10.1016/0301-0082(79)90005-4

136. O'Keefe J, Burgess N. 2005. Dual phase and rate coding in hippocampal place cells: theoretical significance and relationship to entorhinal grid cells. *Hippocampus* 15(7):853-66. doi:10.1002/hipo.20115

137. O'Keefe J, Conway DH. 1978. Hippocampal place units in the freely moving rat: why they fire where they fire. *Exp Brain Res.* 31(4):573-90. doi:10.1007/BF00239813

119. O'Keefe J, Dostrovsky J. 1971. The hippocampus as a spatial map. Preliminary evidence from unit activity in the freely-moving rat. *Brain Res.* 34(1):171-175. doi:10.1016/0006-8993(71)90358-1

138. O'Leary TP, Robertson A, Chipman PH, Rafuse VF, Brown RE. 2018. Motor function deficits in the 12 month-old female 5xFAD mouse model of Alzheimer's disease. *Behav Brain Res.* 337:256-263. doi:10.1016/j.bbr.2017.09.009

139. Olson JM, Tongprasearth K, Nitz DA. 2017. Subiculum neurons map the current axis of travel. *Nat Neurosci.* 20(2):170-172. doi:10.1038/nn.4464

140. Opalka AN, Huang WQ, Liu J, Liang H, Wang DV. 2020. Hippocampal Ripple Coordinates Retrosplenial Inhibitory Neurons during Slow-Wave Sleep. *Cell Rep.* 30(2):432-441.e3. doi:10.1016/j.celrep.2019.12.038

141. Osawa A, Maeshima S, Kunishio K. 2008. Topographic disorientation and amnesia due to cerebral hemorrhage in the left retrosplenial region. *Eur Neurol.* 59(1-2):79-82. doi:10.1159/000109572

142. Osipova D, Takashima A, Oostenveld R, Fernández G, Maris E, Jensen O. 2006. Theta and gamma oscillations predict encoding and retrieval of declarative memory. *J Neurosci.* 26(28):7523-31. doi:10.1523/JNEUROSCI.1948-06.2006

143. Pastalkova E, Itskov V, Amarasingham A, Buzsáki G. 2008. Internally generated cell assembly sequences in the rat hippocampus. *Science.* 321(5894):1322-7. doi:10.1126/science.1159775

144. Paxinos G, Franklin KBJ, Franklin KBJ. 2001. The Mouse Brain in Stereotaxic Coordinates 2nd Ed. San Diego: *Academic Press*

145. Paxinos G, Watson C. 2007. The rat brain in stereotaxic coordinates. 6th ed. London: *Academic Press*

146. Peters A. 1979. Thalamic input to the cerebral cortex. *Trends in Neurosciences*

2:183–185. doi:https://doi.org/ 10.1016/0166-2236(79)90074-2

147. Plihal W, Born J. 1997. Effects of early and late nocturnal sleep on declarative and procedural memory. *J Cogn Neurosci.* 9(4):534-47. doi:10.1162/jocn.1997.9.4.534

148. Poirier GL, Amin E, Good MA, Aggleton JP. 2011. Early-onset dysfunction of retrosplenial cortex precedes overt amyloid plaque formation in Tg2576 mice. *Neuroscience* 174:71-83. doi:10.1016/j.neuroscience.2010.11.025

149. Prince SM, Paulson AL, Jeong N, Zhang L, Amigues S, Singer AC. 2021. Alzheimer's pathology causes impaired inhibitory connections and reactivation of spatial codes during spatial navigation. *Cell Rep.* 35(3):109008. doi:10.1016/j.celrep.2021.109008

150. Rasch B, Born J. 2013. About sleep's role in memory. *Physiol Rev.* 93(2):681-766. doi:10.1152/physrev.00032.2012

151. Rauchs G, Bertran F, Guillery-Girard B, Desgranges B, Kerrouche N, Denise P, Foret J, Eustache F. 2004. Consolidation of strictly episodic memories mainly requires rapid eye movement sleep. *Sleep* 27(3):395-401. doi:10.1093/sleep/27.3.395

152. Robertson RT, Baratta J, Yu J, LaFerla FM. 2009. Amyloid-beta expression in retrosplenial cortex of triple transgenic mice: relationship to cholinergic axonal afferents from medial septum. *Neuroscience* 164(3):1334-46. doi:10.1016/j.neuroscience.2009.09.024

153. Saar-Ashkenazy R, Veksler R, Guez J, Jacob Y, Shelef I, Shalev H, Friedman A, Cohen JE. 2016. Breakdown of Inter-Hemispheric Connectivity Is Associated with Posttraumatic Symptomatology and Memory Impairment. *PLoS One* 11(2):e0144766. doi:10.1371/journal.pone.0144766

154. Scheffzük C, Kukushka VI, Vyssotski AL, Draguhn A, Tort AB, Brankačk J. 2011. Selective coupling between theta phase and neocortical fast gamma oscillations during REM-sleep in mice. *PLoS One* 6(12):e28489. doi:10.1371/journal.pone.002848

155. Schlingloff D, Káli S, Freund TF, Hájos N, Gulyás AI. 2014. Mechanisms of sharp wave initiation and ripple generation. *J Neurosci.* 34(34):11385-98. doi:10.1523/JNEUROSCI.0867-14.2014

156. Schuerger RJ, Balaban CD. 1993. Immunohistochemical demonstration of regionally selective projections from locus coeruleus to the vestibular nuclei in rats. *Exp Brain Res.* 92(3):351-9. doi:10.1007/BF0022902

157. Segneri M, Bi H, Olmi S, Torcini A. 2020. Theta-Nested Gamma Oscillations in Next Generation Neural Mass Models. *Front Comput Neurosci.* 14:47. doi:10.3389/fncom.2020.00047

158. Sheeran WM, Ahmed OJ. 2020. The neural circuitry supporting successful spatial navigation despite variable movement speeds. *Neurosci Biobehav Rev.* 108:821-833. doi:10.1016/j.neubiorev.2019.11.013

159. Shine JP, Valdes-Herrera JP, Hegarty M, Wolbers T. 2016. The Human Retrosplenial Cortex and Thalamus Code Head Direction in a Global Reference Frame. *J. Neurosci.* 36(24):6371–6381. doi:10.1523/JNEUROSCI.1268-15.2016

160. Siclari F, Baird B, Perogamvros L, Bernardi G, LaRocque JJ, Riedner B, Boly M, Postle BR, Tononi G. 2017. The neural correlates of dreaming. *Nat Neurosci.* 20(6):872-878. doi:10.1038/nn.4545

161. Siclari F, Bernardi G, Cataldi J, Tononi G. 2018. Dreaming in NREM Sleep: A High-Density EEG Study of Slow Waves and Spindles. *J Neurosci.* 38(43):9175-9185. doi:10.1523/JNEUROSCI.0855-18.2018

162. Sirota A, Montgomery S, Fujisawa S, Isomura Y, Zugaro M, Buzsáki G. 2008. Entrainment of neocortical neurons and gamma oscillations by the hippocampal theta rhythm. *Neuron* 60(4):683-97. doi:10.1016/j.neuron.2008.09.014

163. Skaggs WE, McNaughton BL. 1996. Replay of neuronal firing sequences in rat hippocampus during sleep following spatial experience. *Science* 271(5257):1870-3. doi:10.1126/science.271.5257.1870

164. Sohal VS. 2012. Insights into cortical oscillations arising from optogenetic studies. *Biol Psychiatry* 71(12):1039-45. doi:10.1016/j.biopsych.2012.01.024

165. Solstad T, Boccara CN, Kropff E, Moser MB, Moser EI. 2008. Representation of geometric borders in the entorhinal cortex. *Science* 322(5909):1865-8. doi:10.1126/science.1166466

166. Spiers HJ, Burgess N, Hartley T, Vargha-Khadem F, O'Keefe J. 2001. Bilateral hippocampal pathology impairs topographical and episodic memory but not visual pattern matching. *Hippocampus* 11(6):715-25. doi:10.1002/hipo.1087

167. Sripanidkulchai K, Wyss JM. 1987. The laminar organization of efferent neuronal cell bodies in the retrosplenial granular cortex. *Brain Research* 406 (1-2):255-269. doi:10.1016/0006-8993(87)90790-6

168. Steriade, M. 2010. Sleep Oscillations and PGO Waves. *Encyclopedia of Neuroscience* 1035-1042. doi:10.1016/B978-008045046-9.00055-3

169. Stewart S, Jeewajee A, Wills TJ, Burgess N, Lever C. 2013. Boundary coding in the rat subiculum. *Philos Trans R Soc Lond B Biol Sci.* 369(1635):20120514. doi:10.1098/rstb.2012.0514

170. Stoiljkovic M, Kelley C, Nagy D, Hajós M. 2015. Modulation of hippocampal neuronal network oscillations by α7 nACh receptors. *Biochem Pharmacol.* 97(4):445-453. doi:10.1016/j.bcp.2015.06.031

171. Tallon-Baudry C, Bertrand O, Delpuech C, Permier J. 1997. Oscillatory gamma-band (30-70 Hz) activity induced by a visual search task in humans. *J Neurosci.* 17(2):722-34. doi:10.1523/JNEUROSCI.17-02-00722.1997

172. Taube JS. 1995. Place cells recorded in the parasubiculum of freely moving rats. *Hippocampus* 5:569–83. doi:10.1002/hipo.450050608

173. Taube JS. 1998. Head direction cells and the neurophysiological basis for a sense of direction. *Progress in Neurobiology* 55(3):225-56. doi:10.1016/s0301-0082(98)00004-5

174. Taube JS, Burton HL. 1995. Head direction cell activity monitored in a novel environment and during a cue conflict situation. *J Neurophysiol.* 74(5):1953-71. doi:10.1152/jn.1995.74.5.195

175. Taube JS, Muller RU, Ranck JB Jr. 1990a. Head-direction cells recorded from the postsubiculum in freely moving rats. I. Description and quantitative analysis. *J Neurosci.* 10(2):420-35. doi:10.1523/JNEUROSCI.10-02-00420.1990

176. Taube JS, Muller RU, Ranck JB Jr. 1990b. Head-direction cells recorded from the postsubiculum in freely moving rats. II. Effects of environmental manipulations. *J Neurosci.* 10(2):436-47. doi:10.1523/JNEUROSCI.10-02-00436.1990

177. Tiesinga P, Sejnowski TJ. 2009. Cortical enlightenment: are attentional gamma oscillations driven by ING or PING. *Neuron* 63, 727–732. doi:10.1016/j.neuron.2009.09.009

178. Todorova R, Zugaro M. 2020. Hippocampal ripples as a mode of communication with cortical and subcortical areas. *Hippocampus* 30(1):39-49. doi:10.1002/hipo.22997

179. Tort AB, Komorowski R, Eichenbaum H, Kopell N. 2010. Measuring phase-amplitude coupling between neuronal oscillations of different frequencies. *J Neurophysiol.* 104(2):1195-210. doi:10.1152/jn.00106.2010

180. Tort AB, Scheffer-Teixeira R, Souza BC, Draguhn A, Brankačk J. 2013. Theta-associated high-frequency oscillations (110-160Hz) in the hippocampus and neocortex. *Prog Neurobiol.* 100:1-14. doi:10.1016/j.pneurobio.2012.09.002

181. Townsend B, Legere JK, O'Malley S, Mohrenschildt MV, Shedden JM. 2019. Attention modulates event-related spectral power in multisensory self-motion perception. *Neuroimage* 191:68-80. doi:10.1016/j.neuroimage.2019.02.015

182. Tsao A, Sugar J, Lu L, Wang C, Knierim JJ, Moser MB, Moser EI. 2018. Integrating time from experience in the lateral entorhinal cortex. *Nature* 561(7721):57-62. doi:10.1038/s41586-018-0459-6

183. Vale R, Campagner D, Iordanidou P, Arocas OP, Tan YL, Stempel AV, Keshavarzi S, Petersen R, Margrie T, Branco T. 2020. A cortico-collicular circuit for accurate orientation to shelter during escape. *BioRxiv* 2020.05.26.117598

184. Valenstein E, Bowers D, Verfaellie M, Heilman KM, Day A, Watson RT. 1987. Retrosplenial amnesia. *Brain 110*, 1631–1646. doi:10.1093/brain/110.6.1631

185. Valerio S, Taube JS. 2016. Head Direction Cell Activity Is Absent in Mice without the Horizontal Semicircular Canals. *J Neurosci.* 36(3):741-54. doi:10.1523/JNEUROSCI.3790-14.2016

186. van Groen T, Wyss JM. 1990. Connections of the retrosplenial granular a cortex in the rat. *J Comp Neurol* 300:593–606. doi:10.1002/cne.903000412

187. van Groen T, Wyss JM. 1992. Connections of the retrosplenial dysgranular cortex in the rat. *J Comp Neurol.* 315(2):200-16. doi:10.1002/cne.903150207

188. van Groen T, Wyss JM. 1995. Projections from the anterodorsal and anteroveniral nucleus of the thalamus to the limbic cortex in the rat. *J Comp Neurol* 358:584–604. doi:10.1002/cne.903580411

189. Van Groen T, Wyss JM. 2003. Connections of the retrosplenial granular b cortex in the rat. J Comp Neurol. 463(3):249-63. doi: 10.1002/cne.10757

190. van Wijngaarden JB, Babl SS, Ito HT. 2020. Entorhinal-retrosplenial circuits for allocentric-egocentric transformation of boundary coding. *Elife* 9:e59816. doi:10.7554/eLife.59816

191. Vann SD, Aggleton JP, Maguire EA. 2009. What does the retrosplenial cortex do? *Nat Rev Neurosci.* 10:792–802. doi:10.1038/nrn2733

192. Varela F, Lachaux JP, Rodriguez E, Martinerie J. 2001. The brainweb: phase synchronization and large-scale integration. *Nat Rev Neurosci.* 2(4):229-39. doi:10.1038/35067550

193. Vazquez J, Baghdoyan HA. 2001. Basal forebrain acetylcholine release during REM sleep is significantly greater than during waking. *Am J Physiol Regul Integr*

Comp Physiol. 280(2):R598-601. doi:10.1152/ajpregu.2001.280.2.R598

194. Viriyopase A, Memmesheimer RM, Gielen S. 2016. Cooperation and competition of gamma oscillation mechanisms. *J Neurophysio*l. 116(2):232–251. doi:10.1152/jn.00493.2015

195. Vitte E, Derosier C, Caritu Y, Berthoz A, Hasboun D, Soulié D. 1996. Activation of the hippocampal formation by vestibular stimulation: a functional magnetic resonance imaging study. *Exp Brain Res.* 112(3):523-6. doi:10.1007/BF00227958

196. Vivekananda U, Bush D, Bisby JA, Baxendale S, Rodionov R, Diehl B, Chowdhury FA, McEvoy AW, Miserocchi A, Walker MC, Burgess N. 2021. Theta power and theta-gamma coupling support long-term spatial memory retrieval. *Hippocampus* 31(2):213-220. doi:10.1002/hipo.23284

197. Vogt BA, Miller MW. 1983. Cortical connections between rat cingulate cortex and visual, motor, and postsubicular cortices. *J Comp Neurol.* 216(2):192-210. doi:10.1002/cne.902160207

198. Wang C, Holtzman DM. 2020. Bidirectional relationship between sleep and Alzheimer's disease: role of amyloid, tau, and other factors. *Neuropsychopharmacology* 45(1):104-120. doi:10.1038/s41386-019-0478-5

199. Wang Y, Romani S, Lustig B, Leonardo A, Pastalkova E. 2015. Theta sequences are essential for internally generated hippocampal firing fields. *Nat Neurosci.* 18(2):282-8. doi:10.1038/nn.390

200. Whittington MA, Traub RD, Kopell N, Ermentrout B, Buhl EH. 2000. Inhibition-based rhythms: experimental and mathematical observations on network dynamics. *Int J Psychophysiol.* 38(3):315-36. doi:10.1016/s0167-8760(00)00173-2

201. Winer JR, Mander BA, Helfrich RF, Maass A, Harrison TM, Baker SL, Knight RT, Jagust WJ, Walker MP. 2019. Sleep as a Potential Biomarker of Tau and β-Amyloid Burden in the Human Brain. *J Neurosci.* 39(32):6315-6324. doi:10.1523/JNEUROSCI.0503-19.2019

202. Womelsdorf T, Schoffelen JM, Oostenveld R, Singer W, Desimone R, Engel AK, Fries P. 2007. Modulation of neuronal interactions through neuronal synchronization. *Science* 316(5831):1609-12. doi:10.1126/science.1139597

203. Wyss JM, Van Groen T, Sripanidkulchai K. 1990. Dendritic bundling in layer I of granular retrosplenial cortex: intracellular labeling and selectivity of innervation. J *Comp Neurol.* 295(1):33-42. doi:10.1002/cne.902950104

204. Xiao NA, Zhang J, Zhou M, Wei Z, Wu XL, Dai XM, Zhu YG, Chen XC. 2015. Reduction of Glucose Metabolism in Olfactory Bulb is an Earlier Alzheimer's Disease-related Biomarker in 5XFAD Mice. *Chin Med J (Engl).* 128(16):2220-7. doi:10.4103/0366-6999.162507

205. Yamawaki N, Corcoran KA, Guedea AL, Shepherd GMG, Radulovic J. 2019a. Differential Contributions of Glutamatergic Hippocampal→Retrosplenial Cortical Projections to the Formation and Persistence of Context Memories. *Cereb Cortex.* 29(6):2728–2736. doi:10.1093/cercor/bhy142

206. Yamawaki N, Li X, Lambot L, Ren LY, Radulovic J, Shepherd GMG. 2019b. Long-range inhibitory intersection of a retrosplenial thalamocortical circuit by apical tuft-targeting CA1 neurons. *Nat Neurosci.* 22(4):618-626. doi:10.1038/s41593-019-0355-x

207. Yamawaki N, Radulovic J, Shepherd GM. 2016. A corticocortical circuit directly links retrosplenial cortex to M2 in the mouse. *J Neurosci.* 36:9365–74. doi:10.1523/JNEUROSCI.1099-16.2016

208. Yoshida K, Oka H. 1995. Topographical projections from the medial septum-diagonal band complex to the hippocampus: a retrograde tracing study with multiple fluorescent dyes in rats. *Neurosci Res.* 21(3):199-209. doi:10.1016/0168-0102(94)00852-7

209. Yousuf H, Nye AN, Moyer JR Jr. 2020. Heterogeneity of Neuronal Firing Type and Morphology in Retrosplenial Cortex of Male F344 Rats. *J Neurophysiol.* 123(5):1849-1863. doi:10.1152/jn.00577.2019

210. Zhigalov A, Duecker K, Jensen O. 2021. The visual cortex produces gamma band echo in response to broadband visual flicker. *PLoS Comput Biol.* 17(6):e1009046. doi:10.1371/journal.pcbi.1009046